Design and Development of An Ultra-capacitor based Peak Power Management System for Electrified Metro Transit Powertrains

Nina Naghizadeh

A Thesis

in

The Department

of

Electrical and Computer Engineering

Presented in Partial Fulfillment of the Requirements

for the Degree of

Master of Applied Science (Electrical and Computer Engineering) at

Concordia University

Montreal, Quebec, Canada

January 2015

CONCORDIA UNIVERSITY
SCHOOL OF GRADUATE STUDIES

This is to certify that the thesis prepared

By: Nina Naghizadeh

Entitled: "Design and Development of An Ultra-capacitor based Peak Power Management System for Electrified Metro Transit Powertrains"

and submitted in partial fulfillment of the requirements for the degree of

Master of Applied Science

Complies with the regulations of this University and meets the accepted standards with respect to originality and quality.

Signed by the final examining committee:

_____ Chair
Dr. M. Z. Kabir

_____ Examiner, External
Dr. A. Bagchi (BCEE) To the Program

_____ Examiner
Dr. S. Hashtrudi Zad

_____ Supervisor
Dr. S. Williamson

Approved by: _____
Dr. W. E. Lynch, Chair
Department of Electrical and Computer Engineering

January 30, 2015

_____
Dr. Amir Asif, Dean
Faculty of Engineering and Computer Science

Abstract

Design and Development of An Ultra-capacitor based Peak Power Management System for Electrified Metro Transit Powertrains

Nina Naghizadeh

Hybridization of the metro traction systems has been the research focus during the last few years. Research has been done on various technologies that combine, in addition to its main energy source (DC rail), reversible energy storage devices like fly-wheels, ultra-capacitors, and batteries. Among these technologies, ultra-capacitors are promising because of their high power density and the fact that their lifespan is about ten years longer than that of batteries. The idea is to store the regenerative braking energy in an ultra-capacitor module. This energy will be used during the acceleration. As such, the grid will be protected from the over-currents related to start-up of the metro car. Moreover, the traction system efficiency will increase since the braking energy which is dissipated in resistors in the current system, will be recovered.

In this thesis the Montreal Metro Traction system is studied. The main energy source (MES) is the DC rail in Metro. The metro system is first analysed and

model. Ultra-capacitor sizing is done for the system. For the purpose of simulation, the initial system is scaled down. A 2 Hp machine is used as the traction motor. A bidirectional buck-boost DC/DC converter is designed to drive the motor. The ultra-capacitor interfaced bidirectional DC/DC converter and the ultra-capacitor bank are modeled and simulated. A unidirectional boost DC/DC converter is designed and simulated along with PI controllers, to control the flow of power from the DC rail (MES). Moreover, two efficient supervisory control strategies are developed for two possible ultra-capacitor bank sizes of the Montreal metro system. The novel control strategy enables superior regulation capability and ease of control.

Acknowledgments

I would like to express my sincere gratitude to Prof. Sheldon Williamson for his availability, commitment and financial support throughout the course of this research. I am deeply thankful to Transport Canada for funding this project. I wish also to express my gratefulness to Dr. Najath Abdul Azeez for his generosity in sharing knowledge and experience.

I am extremely grateful to my friends Narges, Lesedi, Maninder, Wanjiko, Jemimah, and Tasneem for their timely help regarding my work. The pleasurable time spent with the colleagues at the Power Electronics and Energy Research (PEER) Group will always be remembered.

Last but not at all the least; I would like to sincerely thank family and all my friends. This thesis would have just remained a dream without your encouragement, trust and support, Pooya.

To my parents and brother.

Table of Contents

List of Figures

List of Tables

List of Acronyms and Abbreviations

AC	Alternating Current
AES	Auxiliary Energy Storage
ESR	Equivalent Series Resistance
C	Capacitor
DC	Direct Current
e_{ss}	Steady State Error
f_s	Switching Frequency
f_c	Cross-over Frequency
Hp	Horse Power
L	Inductor
MES	Main Energy Source
OV	Overshoot
PI	Proportional-Integral
PM	Phase Margin
PMDC	Permanent Magnet Direct Current

PWM	Pulse Width Modulation
R	Resistor
T_r	Rise Time
T_S	Settling Time
SoC_{UC}	Ultra-Capacitor State of Charge

List of Symbols

ρ	Density of Air
J	Rotational Inertia
α	Rotational Acceleration
m	Mass
J_1	Tire Inertia
J_t	Total Tire Inertia
N_x	Number of Axles
J_m	Motor Inertia
N	Number of Motors
GR	Gear Ratio
g	Gravitational Acceleration Constant
β	Grade Angle
C_0	Coefficient of Rolling Resistance
C_D	Aerodynamic Drag Coefficient
A_F	Equivalent Frontal Area of the Vehicle
r	Radius
a	Linear Acceleration
η	Product of Motor Efficiency and the Transmission (Gear) Efficiency
R_{Leak}	Self-discharge Resistance
D	Duty Ratio

K_P	Proportional Gain
K_I	Integral Gain
K_D	Derivative Gain
N	Filter Coefficient
R_a	Armature Resistance
L_a	Armature Inductance
K_E	Back-EMF Constant
K_T	Motor Torque Constant
T_m	Moving Time Window
B_m	Viscous Friction Coefficient
T_f	Coulomb Friction Torque
T	Torque

Chapter 1: Introduction and Thesis Overview

1.1 Background

1.1.1 Background

Electrochemical double-layer capacitors, which are famous as ultra-capacitors have been the center of attention in power conversion applications. They have been used in controlled industrial traction and automotive drives. Ultra-capacitors are used to store the drive's regenerative braking energy during braking. The stored energy is then recovered when the drive runs in motoring mode. In regular drives, the braking energy which represents about 20%–30% of the expended energy is dissipated in a brake resistor [1]. Ultra-capacitors can be used in place of these resistors as the Auxiliary Energy Source (AES). The AES limits the power constraints on the Main Energy Source (MES) by providing the peak acceleration power. This allows the MES to work at constant or near-constant power levels, lower than the peak load power. Additionally, it makes possible the MES's power-rating reduction to levels near average power demand which results in drive cost drop [2].

Today, centralized power generation from large-scale plants own a vital spot in industrialized countries across the world. This source is used as the MES in electrified rail traction system. Therefore, hybridization of the MES with energy storage technologies grants the possibility of storing excess energy when the demand is low, and increase its production when the demand is high [3].

Ultra-capacitors are appropriate substitute for batteries in energy storage systems where repetitive high power density is required. In comparison with batteries, ultra-capacitors have a lower energy density and a higher power density. They can thus be used in a lot of applications for energy storage management especially where bursts of power are required over a short period of time [4].

The use of ultra-capacitors call for power electronic converters in order to ensure their efficient management. The power converter interfaces the ultra-capacitor bank to the drive DC bus. It is controlled to meet the system requirements which include regulation of the DC bus voltage, ultra-capacitor bank state of charge control, or active energy sharing between the drive and ultra-capacitor bank [5].

In this thesis the Montreal metro traction system where the DC rail is the MES is studied. The DC rail is fed from a diode rectifier stage connected to the AC-utility grid. Since the current is unidirectional in a diode rectifier, the

regenerative energy cannot be fed back to the grid hence it is dissipated in the braking resistors. Hybridization of this system with ultra-capacitors adds the capability to store and recover the braking energy. Besides, the DC/DC converter controls and smoothens the rectifier input power. Therefore, an ultra-capacitor bank can be used as the AES in this system which improves sustainability by conserving energy, via the recovery of braking energy.

1.1.2 System Overview

Ultra-capacitors are broadly used as AES in electric vehicles (EV) as well as in hybrid electric traction systems. The regenerative braking system absorbs some of the vehicle's kinetic energy by operating the traction motor as a generator. The braking torque on the wheels recharges the AES. Ultra-capacitors are then discharged to provide the motor drive's peak acceleration power. A block diagram of the system during AES charge and discharge is shown in Figure 1-2 and Figure 1-1.

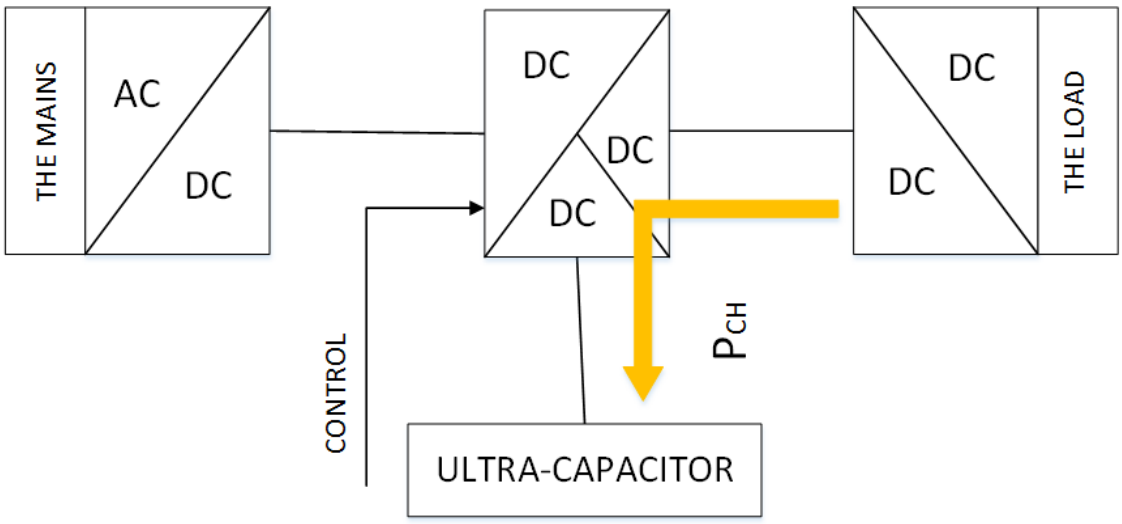

Figure 1-1: Ultra-Capacitors are charged by Braking Energy

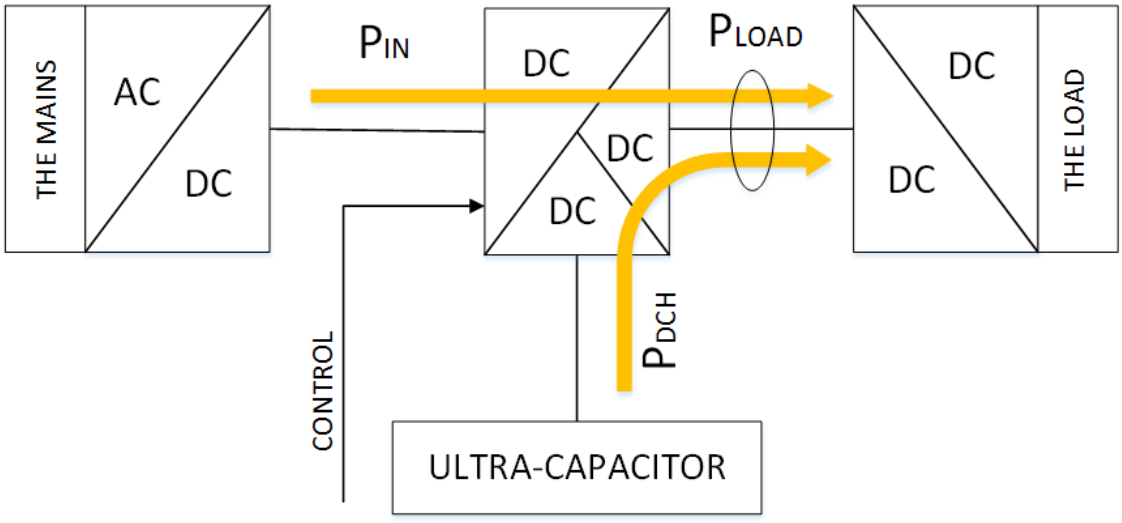

Figure 1-2: Ultra-Capacitors discharging to the Load adopted from [1]

The rapid acceleration and deceleration results in steep peaks and dips in the load power profile. These transients can be smoothed out by the ultra-capacitor based AES. This is because ultra-capacitors are capable of handling high resultant currents surging in and out. This unique function of the ultra-capacitors

remarkably reduces the power constraints on the MES. For example, hybridization of the battery with ultra-capacitor, minimizes the cycling of the battery at high charge and discharge currents. Instead, the battery works with an approximately constant average current. Therefore, the issues associated with peak currents that tend to generate extensive heat inside the battery, reducing the efficiency of the battery and in the long run decreasing its lifetime, will be solved [3]. The MES can also be any other source like fuel cells or the utility grid with respect to the application of the specific system.

To achieve system flexibility and high efficiency, a switching mode power converter is used to connect the ultra-capacitor bank to the load DC bus. Most DC/DC converter topologies are based on non-isolated half-bridge buck-boost topology. The buck-boost topology is a bidirectional current converter with high efficiency as well as low number of components. Multi-level and interleaved buck-boost topologies are used to achieve high voltage levels and switching frequencies by spreading the voltage stress on several [4]. The switches are stressed on a fraction of the total DC bus voltage. This allows the utilization of lower-voltage-rated switches achieving better switching and conduction performance compared to the switches rated on the full blocking voltage. Switching loss are also then decreased [5].

The converter is controlled in a way to meet the system requirements. Three major system requirements are control of the DC bus voltage, ultra-capacitor bank state of charge, and active energy sharing between the drive and the ultra-capacitor bank [5].

1.2 Literature Review

Proportional-Integral (PI) controllers are designed to perform the task of controlling the DC bus voltage and ultra-capacitor bank current. The generation of the references for PI controllers is a key issue in the overall system operation. Various methods have been proposed and implemented to generate the controller references.

In systems with batteries and ultra-capacitors as the AES, the DC bus voltage is imposed by the battery module [1]. As such, only ultra-capacitor current control is needed. On the other hand, systems operating with the ultra-capacitors as the AES, require a DC/DC converter to regulate the DC bus voltage. In that case, the DC/DC converter is usually a buck or a boost [1].

Selection of the DC bus voltage reference is straight forward; it is the constant designed DC bus voltage. The ultra-capacitor current reference varies with the fluctuation of the load power profile.

One way to obtain the ultra-capacitor reference current is from a power balance diagram between the ultra-capacitor module and the DC bus. The ultra-capacitor reference current will be calculated from subtraction of the actual load current from the average load current. In other words, the reference will be the peak load current which is met by the AES. The average load current is the battery current in topologies using the battery as the MES [6], [7], [8], [3]. Another method is to limit the current extracted from (or injected to) the battery pack. Therefore, currents outside these limits will come from the ultra-capacitors. The current reference automatically changes when the battery is fully charged, which prevents over charging during braking. Optimization tools can also be used to generate the reference values. Neural network (NN) techniques, for example, can procure the learned value of the most efficient current for the AES. The information is trained using various sets of data based on known load current and drive cycle, preserving boundary conditions such as ultra-capacitor state of charge. The result is the optimal battery current. Thus, the most efficient set of currents must be found for the ultra-capacitor [9].

In systems with the rectified DC rail source from the AC-utility grid as the MES, like electrified metro, more control requirements come into the picture. The reason is that the MES is unidirectional in current i.e. it can never take the

braking energy coming from the drive load. Hence, it must be ensured that the ultra-capacitors are always discharged before beginning of the braking. Otherwise, they will be overcharged. This important fact imposes some limitations on the choice of the current reference generation algorithm as well as the capacity of the AES. The control algorithms presented previously for a bidirectional MES, cannot be used for the electrified metro system.

In [4], an ultra-capacitor based storage system is designed for traction application. The ultra-capacitor current reference is generated from the power balance rule as described in [10], [11]. To solve the problem of unidirectional MES, braking resistors are connected across the DC bus with a switch. When the ultra-capacitors are fully charged, the switch is pulsed to dissipate the excess power.

In [5], an inner current controller and three outer controllers are used. The inner PI controls the ultra-capacitor current. Two of the outer voltage loops regulate the DC bus voltage between a minimum and a maximum voltage level. The other voltage loop controls the ultra-capacitor voltage in a way to produce the required current reference for the inner loop. The rated ultra-capacitor voltage is the same as the rated DC bus voltage which makes possible to employ the proposed control algorithm. However, having the same AES and DC bus voltage level,

constrains the size of the AES. For heavy transit application, 48 Volts or 125 Volts ultra-capacitor modules are normally used. The DC bus voltage in metro application is about 600-800 Volts. For the ultra-capacitor bank to reach the DC bus voltage level several modules should be connected in series. Therefore, an ultra-capacitor bank with a relatively large capacity should be used for the above algorithm.

The size of the ultra-capacitor bank is important in terms of the initial cost, the implementation and the maintenance. The weight and volume that the ultra-capacitor bank takes in the vehicle should also be taken into account. Sizing of the AES is also done in several ways. It can be designed to store sufficient energy to repeatedly sustain power during both acceleration and braking tasks. In the case of city driving conditions, extreme demanding tasks like climbing a hill should also be taken into account. In other cases, sizing is done to provide the peak acceleration power. Since the braking power is about 20 to 30 percent of the acceleration power, the MES has to help charging the ultra-capacitors during constant speed periods [1], [12].

An ultra-capacitor based AES can also be sized to meet the total acceleration power i.e. not only the peak acceleration power. However, the feasibly of implementing such a system in terms of weight and cost should be carefully

investigated [13]. To minimize the cost, the AES can be sized to capture the regenerative braking energy. As such, it can provide a percentage of the peak acceleration power which will still smoothen the MES power demand. Inevitably, the percentage of MES peak power shaving is less compared to when the AES is sized to provide the full acceleration peak power.

1.3 **Purpose and Method**

The core purpose of this thesis is to examine the effects of integrating an ultra-capacitor bank into the existing Montreal metro system. The scope is therefore narrowed to three objectives.

I. The first objective is to develop an effective control algorithm which stores the regenerative braking energy and provides the peak acceleration energy;
II. The second objective is to optimize the sizing and utilization of the ultra-capacitor bank;
III. Protection of the ultra-capacitor bank is also a key factor;

For the system under study, the size of the ultra-capacitor bank is important since the cost of hybridization increases with enlarging the AES capacity. Moreover, for a system that is constantly connected to the grid, forcing a large

AES system is not necessary. A large AES may reduce the control complexity of the system, but adds the maintenance and system efficiency problems.

The simulated system consists of a boost converter interfaced with a DC source that represents the DC rail in the metro system. The boost converter will operate in voltage control or current control mode based on the employed control algorithm. A bidirectional current converter is required to do the task of charging and discharging of the ultra-capacitor bank. To this end, a half-bridge buck-boost converter is used. This converter also works in voltage control or current control mode as required. The above two converters are connected in parallel to the DC bus. The DC bus is directly connected to the load. The load is a bidirectional current motor drive which represents the metro traction motor.

A model for the Montreal metro MR73 train-set is formulated in Matlab/ Simulink after conducting analysis and calculations based on the mechanical parameters and a sample drive cycle. The developed Model provides the load power profile for the electrical traction motor in the metro system. Ultra-capacitor sizing is done for the given load power profile.

For the purpose of simulation, the above power profile is scaled down and so is the ultra-capacitor bank.

The Baldor CDPW3585 2 horse power (Hp) Permanent Magnet Direct Current (PMDC) machine is selected to emulate the traction motor. The size of the Montreal metro traction motor is 168 Hp. Tests for the machine parameters are done in the PEER laboratory at Concordia. The machine is simulated in Matlab/Simulink and its bidirectional current drive is also a buck-boost converter. The bidirectional buck-boost converter and the boost converter are also designed for the scaled down load power profile. All the three converter topologies will first be modeled, simulated and analyzed using Matlab/Simulink numerical computation software.

In this thesis a novel control strategy is proposed and simulated in two phases based on two possible ultra-capacitor bank sizes for the Montreal metro system. In the first phase, the method used in [3] is adopted then modified for this application. The developed control strategy enables simpler dynamics, compared to methodologies used in the literature, superior regulation capability and ease of control. On the other hand, this control scheme does not work for a small ultra-capacitor bank size which provides the peak acceleration energy. To this end, a second control strategy is established in the next phase. In the second strategy, the control functionality of the converters is changed in a way to produce the desired results.

1.4 Thesis Outline and Contributions

The structure of the thesis is as follows. In chapter 2 a brief overview of the Montreal metro system is presented. The procedure to derive the torque and power profile as the load of the electrical motors from the metro train-set mass and mechanical parameters is discussed.

In chapter 3, the physical and electrical characteristics of the ultra-capacitors are briefly discussed. Then ultra-capacitor sizing is done for the calculated power rating of the Montreal metro as derived in chapter 2. The initial metro power profile is scaled down which reduces the rating of the ultra-capacitor bank.

The bidirectional DC/DC converter is designed first in chapter 4. The operation principals of the converter are explained. Then, the converter components and filter capacitor are designed according to the predefined operating conditions and finally the converter is modeled. The objective is to design a feedback controller for the converter which enables us to control the current flowing to and from the ultra-capacitor bank. An adequate control design is then formulated based on linear control theory using proportional-integral-controllers. The same procedure is then followed for the DC rail Boost converter design.

In chapter 5 the Baldor CDPW3585 PMDC is studied. The extraction of the parameters tests is described along with the design of the motor drive. The motor is loaded with a load that emulates the motion of the metro derived in chapter 3, in Matlab/Simulink. Cascaded speed and current control is also employed for the drive.

In chapter 6, the formulated supervisory control unit is first explained. Secondly, it is implemented in the buck-boost topology. The control and over/under voltage protection strategy are applied to the system. Using Matlab/Simulink the control strategy is simulated with the PMDC motor drive together with the DC rail boost converter. The simulations are done for two control algorithms. The demand and function of each strategy is discussed in detail as well as their pros and cons.

Chapter 8 summarizes the work done in this thesis. Suggestions for future work to expand the current work are presented.

The contributions of this thesis are as follows:

- A comprehensive study of the characteristics of the Montreal metro traction system. Assessing the power requirement. Analyzing the issue of peak power drawn from the grid as well as wasted regenerative braking energy

- Development of a model for the MR73 metro train-set in Matlab/Simulink
- Review of ultra-capacitor assisted hybrid traction systems. Study of various topologies and control strategies. Study of the effects of integrating an ultra-capacitor bank to the existing metro system
- Design and analysis of PI controllers based on time domain requirements of this application
- Design of a bidirectional drive as well as speed and current controller for a Permanent Magnet DC motor; model Baldor CDPWD3585
- Development and validation of two effective supervisory control algorithms for the designed system in Matlab/Simulink
- Proposing an optimal operation point strategy for maximum utilization of the ultra-capacitor bank
- Introduction and validation of an ultra-capacitor bank protection system Matlab/Simulink

Chapter 2: MR73 Metro Train-set Drivetrain

2.1 Introduction

To study the power requirement of the Montreal metro the train-set model MR73 is selected. The objective is to derive the power and torque profile of this train-set. The results will be used to analyse the hybridization of the MES via ultra-capacitors.

First the general dynamics of the motion of a vehicle will be studied where the tractive torque and power will be derived. Then, power and torque of the MR73 train-set will be derived.

2.2 Dynamics of Vehicle Motion

Tractive force is the force between the vehicle's tires and the road (and parallel to the road) supplied by the electric motor in an EV. The dynamic equation of motive force in the tangential direction is given by:

$$F_{TR} = F_a + F_{AD} + F_{Roll} + F_{gxT} \tag{2-1}$$

The traction force, F_{TR}, consists of the acceleration force, F_a, the gravitational force in the tangential direction, F_{gxT}, rolling resistance of the tires, F_{Roll} and the

aerodynamic drag force, F_{AD} [14], [15]. The components of the traction force will be explained in detail in the following section and is shown in Figure 2-1.

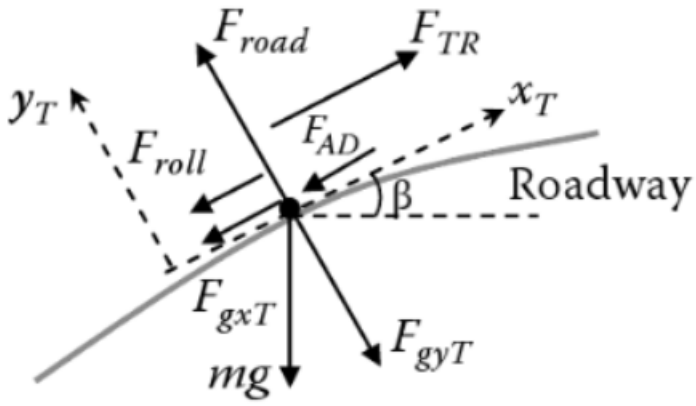

Figure 2-1: Forces acting on a vehicle adopted from [16]

2.2.1 Acceleration Force

The acceleration force is composed of the linear acceleration force and the rotational acceleration force.

$$F_a = F_{a1} + F_{a2} \tag{2-2}$$

Linear Acceleration force is:

$$F_{a1} = m\frac{dv(t)}{dt} \tag{2-3}$$

Where m is the total mass of the vehicle and $\frac{dv(t)}{dt}$ is the acceleration of the vehicle.

Rotational Acceleration Force is:

$$F_{a2} = J\alpha_{tire} \tag{2-4}$$

Where J is the rotational inertia and α_{tire} is the rotational acceleration of the tire.

The rotational inertia is the summation of the motor inertia referred to the tire side and the tire inertia.

$$J = J_1 + J_2 \tag{2-5}$$

$$J_1 = 2N_x J_t \tag{2-6}$$

$$J_2 = \frac{NJ_m}{GR^2} \tag{2-7}$$

J_1 is the total tire inertia. J_t is the tire inertia and N_x number of axles. Each axle is connected to two tires. J_2 is the total motor inertia referred to the tire side. N is the number of motors, GR is the gear ratio and J_m is the motor inertia [16], [15]. There is also a rule of thumb to calculate F_{a2}. It is about ten percent of F_{a1} [17].

2.2.2 Gravitational Force

The gravitational force of the vehicle that should be overcome for moving forward is:

$$F_{gxT} = mg\sin\beta \tag{2-8}$$

Where m is the total mass of the vehicle, g is the gravitational acceleration constant, and β is the grade angle with respect to the horizon. Knowing the

grade percentage, β can be calculated from the following equation.

$$\%\,\text{grade} = 100\tan\beta \tag{2-9}$$

2.2.3 Rolling Resistance Force of the Tires

The rolling resistance is created by the friction of the tire at the contact surface with the roadway. The tractive force F_{TR} must overcome this force, F_{Roll}.

$$F_{Roll} = mg\left(C_0 + C_1 V^2(t)\right) \tag{2-10}$$

Where C_0 is the coefficient of rolling resistance. Typically, 0.004< C_0 <0.02 (unitless), and $C_1 << C_0$ (s^2/m^2) [16].

2.2.4 Aerodynamic Drag Force

The result of viscous resistance and pressure distribution of the air working against the vehicle motion is the aerodynamic drag force. The force is given by:

$$F_{AD} = 0.5 C_D \rho A_F V(t)^2 \tag{2-11}$$

Where ρ is the air density in kg/m^3, C_D is the aerodynamic drag coefficient (dimensionless, and typically is 0.2<C_D<0.4), and A_F is the equivalent frontal area of the vehicle [16].

2.3 Gear Ratio

The gear is a mechanical power transmission mechanism used to gain a

mechanical advantage through an increase in torque or decrease in speed. This mechanical device uses the law of energy conservation; torque times speed is power that remains constant in an ideal transmission process. The gearbox can be used as a torque multiplier or speed reducer. A typical gear mechanism is shown in Figure 2-2.

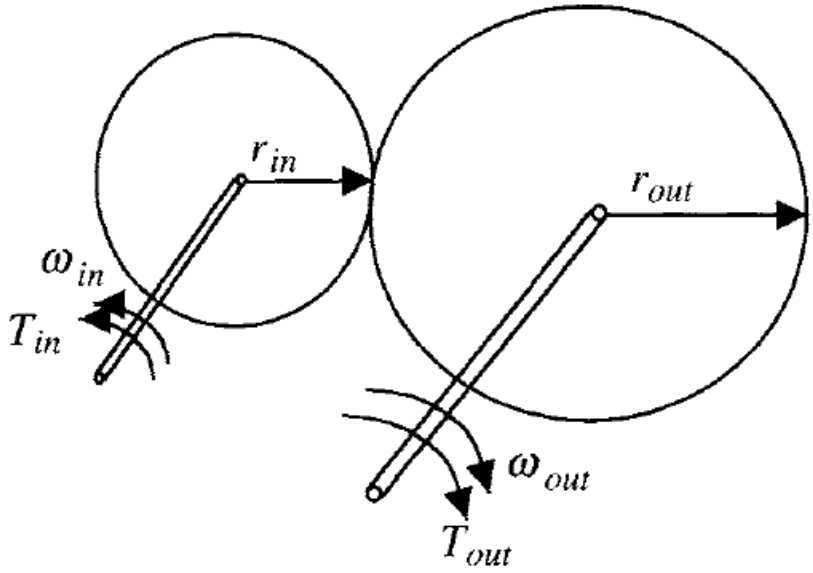

Figure 2-2: Gear Mechanism [16]

Physically, a gear is a round disk with teeth cut at equal breaks around the rim designed to engage with similar teeth of another disk. The round disks, placed in groups, convey power from one gear to another. The teeth at both the disks lock the driving and the driven shafts together to transfer the energy through contact.

For a disk with radius *r,* the linear and the angular velocity are related by:

$$\omega r = \upsilon \tag{2-12}$$

The linear velocity at the gear teeth contact point is the same for the two gears disks shown in Figure 2-2 with different radius:

$$\omega_{in} r_{in} = \upsilon = \omega_{out} r_{out} \tag{2-13}$$

The input shaft of the gear box is the motor and the output is the vehicle axle with tires.

$$\omega_{in} = \omega_{motor} \tag{2-14}$$
$$\omega_{out} = \omega_{tire} \tag{2-15}$$

The gear ratio is defined in terms of the ratio of speed transformation between the input shaft and the output shaft [16].

$$GR = \frac{\omega_{motor}}{\omega_{tire}} = \frac{r_{tire}}{r_{motor}} \tag{2-16}$$

Assuming 100% efficiency of the gear box:

$$\begin{aligned} P_{out} &= P_{in} \\ T_{motor}\omega_{motor} &= T_{tire}\omega_{tire} \end{aligned} \tag{2-17}$$

The gear ratio in terms of the torque at the two shafts is:

$$GR = \frac{T_{tire}}{T_{motor}} = \frac{r_{tire}}{r_{motor}} \tag{2-18}$$

2.3.1 Tire and Motor Rotational Acceleration

Tire rotational acceleration is the rate of change of its angular velocity given by:

$$\alpha_{tire} = \frac{\Delta\omega(t)}{\Delta t} \tag{2-19}$$

The tire linear acceleration is:

$$a_{tire} = \frac{dV(t)}{dt} \tag{2-20}$$

The relationship between linear and rotational acceleration is therefore:

$$\alpha_{tire} = \frac{d\omega(t)}{dt} = \frac{d(v(t)/r_{tire})}{dt} = \frac{a}{r_{tire}} \tag{2-21}$$

The motor rotational acceleration is the product of the tire rotational acceleration and the gear ratio [16].

$$\alpha_{motor} = \alpha_{tire} GR \tag{2-22}$$

2.3.2 Torque, Energy, and Power Calculation

Total traction torque at the shaft is equal to the product of the total traction force and the rotating radius, which is tire radius.

$$T_{TR} = F_{TR} r_{tire} \tag{2-23}$$

Total torque referred to the motor side is:

$$T_{TM} = \frac{T_{TR}}{\eta\, GR} \tag{2-24}$$

Where η is the product of the motor efficiency and the transmission (gear) efficiency.

$$\eta = \eta_{motor} \eta_{transmission} \tag{2-25}$$

Energy output at driving axle is the product of force and distance travelled [14].

$$E_T = F_{TR} D \tag{2-26}$$

Total energy is the summation of energy consumed for each tractive force. The consumed energy in each mode can be calculated as the following.

Energy to accelerate the vehicle is given by:

$$E_{acc} = F_a D_1 \tag{2-27}$$

D_1 is the distance travelled during acceleration.

Some energy is consumed to overcome the aerodynamic drag, rolling resistance, and grade forces during acceleration.

$$E_g = F_{gxT} D_1 \tag{2-28}$$
$$E_{Roll} = F_{Roll} D_1 \tag{2-29}$$
$$E_{AD} = F_{AD} D_1 \tag{2-30}$$

Total energy output at the axle is:

$$E_T = E_{acc} + E_g + E_{Roll} + E_{AD} \tag{2-31}$$

Now tractive power can be calculated by dividing the total energy by time.

$$\mathrm{P}_{\mathrm{TR,average}} = \frac{\Delta E}{\Delta t} = \frac{E_T}{\Delta t} \tag{2-32}$$

Instantaneous tractive power is therefore the product of the instantaneous torque and the instantaneous angular velocity [14], [16].

$$\mathrm{P}_{\mathrm{TR}}(t) = T_{TR}\omega(t) \tag{2-33}$$

2.4 **Montreal Metro MR73 Drive Train**

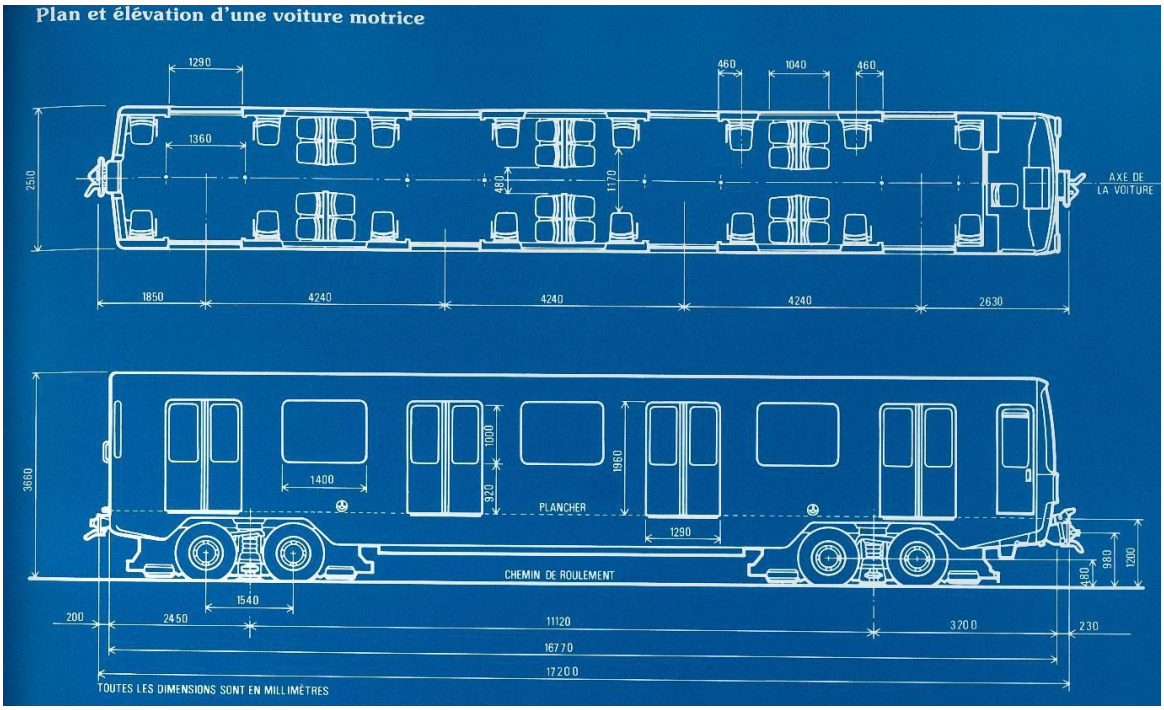

Figure 2-3: MR73 Train-set Schematic adopted from [13]

The train-sets have five possible compositions. We call M the train-set with motors and R the trailer. The five following compositions exist.

Table 2-1: Train-set Compositions [13]

M- One train-set
MR- One train-set with a trailer
MRM- Two train-sets with a trailer (called unit)
MRM MRM- Two units
MRM MRM MRM- Three units

These combinations in Table 2-1 have the following detailed information.

Table 2-2: Characteristics of the Combinations of the Train-sets [13]

Type of Car	Number of Passengers			Estimation of the masses kg		
	Seated	Standing	Total	Passengers	Empty	Full
M	40	120	160	10890	27450	38340
MR	40	120	160	10890	20960	31850
MRM	120	360	480	32670	75860	108530
MRM MRM	240	720	960	65340	151720	217060
MRMMRMMRM	360	1080	1440	98010	227580	325590

Table 2-3: Mechanical Parameters [13]

Rated Speed	45 mph
Maximum Speed	55 mph
Type of bogie	2 bogies with 2 axles per car on tire or iron wheel, 1 motor per differential axle
Transmission Ratio	Reducer + Differential gives 12.5:1
Maximum Slope	1 %

Table 2-4: Tire Rotational Inertia [18], [19]

Tire width	300 mm
Aspect ratio	60 %
Mass	20 kg
Tread to sidewall thickness ratio	2
Total Rotational Inertia (per tire)	3.1675 kg/m^2

Table 2-5: Traction Motor Parameters [13]

Type of motor	DC Series
Model	BBC (Brown Boveri Canada) Ancestor of ABB motors
Power	125 kW
Nominal Current	400 amps
Nominal Voltage	340 Volts
Assumed motor inertia [15]	8 kg/m2

A sample drive cycle (red line) and acceleration profile (blue line) of the

Montreal metro is shown in Figure 2-4.

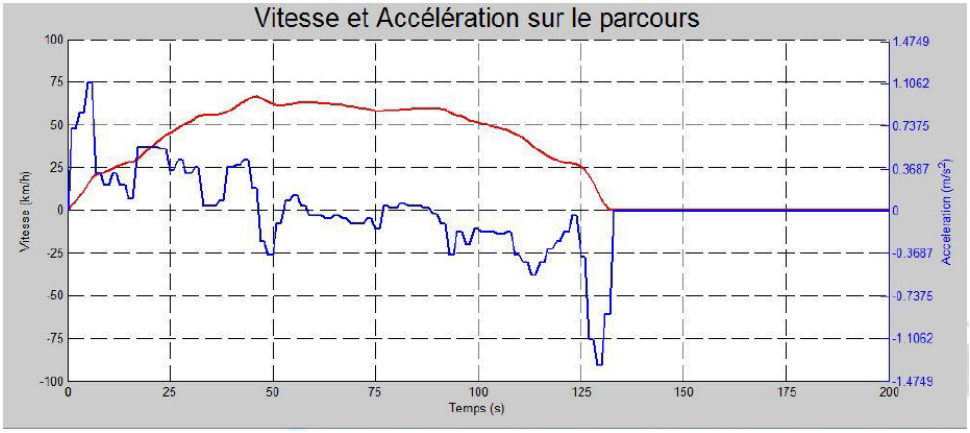

Figure 2-4: Speed and Acceleration VS time of MR73 Train-set, Yellow line, Montreal Metro [13]

2.5 **Mechanical Study of the Train-set Model MR73**

The "MRMMRMMRM" configuration is chosen for this study. There are nine cars in this configuration among which three are trailers. There are two bogies per car. Each bogie has two axles and each axle is connected to two tires. Therefore, each car has eight tires and four motors. As such, in this configuration, there are 24 motors and 72 tires.

The drive cycle in Figure 2-4 is simplified as seen in Figure 2-5 for the purpose of calculations.

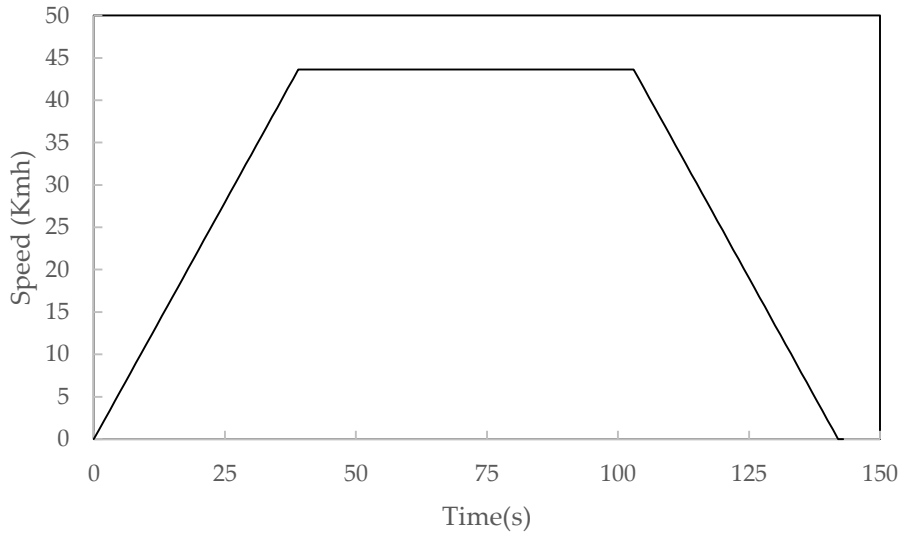

Figure 2-5: Simplified Drive Cycle of MR73 Train-set

As seen in Figure 2-5, the drive cycle consists of three modes: acceleration, constant speed, and deceleration or braking. In this section the tractive torque and power for each mode will be calculated. Before proceeding to the calculation section, some variables are fixed.

Among the total 72 tires of the train-set under study, 48 are connected to the motors; the rest are moving the three trailers. Therefore, the traction force should be divided by 48 to get the force per tire.

$$F_t = \frac{F_{TR}}{48} \tag{2-34}$$

Torque at tire is equal to the product of tire tractive effort and its radius. As such:

$$T_t = F_t r_{tire} \tag{2-35}$$

Each motor is connected to two tires. Total torque referred to the motor shaft is [14]:

$$T_m = \frac{2\ T_t}{\eta\ GR} \tag{2-36}$$

Tire linear and rotational acceleration and deceleration will be calculated here from the parameters given in Table 2-2, Table 2-3, Table 2-4, Table 2-5, and Table 2-6. The Maximum metro speed in most routes is about 72 km/h. Therefore, the maximum speed is taken as 72 km/h instead of 88 km/h. Tire linear acceleration from equation (2-20) is given for the acceleration period as:

$$a_{tire} = \frac{dV(t)}{dt} = 0.48(m/s^2)$$

Tire rotational acceleration from equation (2-21) is:

$$\alpha_{tire} = \frac{0.48}{0.48} = 1\,(\mathrm{rad}/\mathrm{s}^2)$$

$$\alpha_{tire} = 9.55\,(\mathrm{rpm}/\mathrm{s})$$

The motor acceleration from equation (2-22) is:

$$\alpha_{motor} = \alpha_{tire} GR = 9.55 \times 8 = 76.4\,(\mathrm{rpm}/\mathrm{s})$$

Tire deceleration is the negative of acceleration. The motor deceleration calculation follows the same rule.

$$\alpha_{motor} = \alpha_{tire} GR = -9.55 \times 8 = -76.4 \left(^{\mathrm{rpm}}/_{\mathrm{s}}\right)$$

Table 2-6: MR73 Train-set Parameters [13]

Train-set length	3660 mm
Train-set width	2500 mm
Frontal surface of the train-set	9.15 m^2
Tire Radius	480 mm
Air Density ρ	1.204 kg/m^3
Aerodynamic drag coefficient (C_D)	0.4
% Grade	1 %
GR	8
Gear Efficiency(transmission efficiency)	98 %
Metro Car Configuration	'MRMMRMMRM'
Metro Car Weight	325590 kg
Number of motors	24
Line Voltage	750 Volts
Motor Efficiency	90 %
Generator Efficiency	70 %
coefficient of rolling resistance (C_0)	0.01
C_1	6×10-6
Acceleration of gravity (g)	9.8 m/s^2

2.5.1 Power and Torque Calculation

To calculate the power and torque with the simplified drive cycle of Figure 2-5, a Matlab/Simulink model is developed which is shown in Figure 2-6. The code in the Matlab Function block in Figure 2-6 is based on equations presented in sections 2.2 and 2.3 is available in Appendix 1. The input of this block is the

machine speed which is derived from the drive cycle using equation (2-16). The output of the block is the load power and torque profiles.

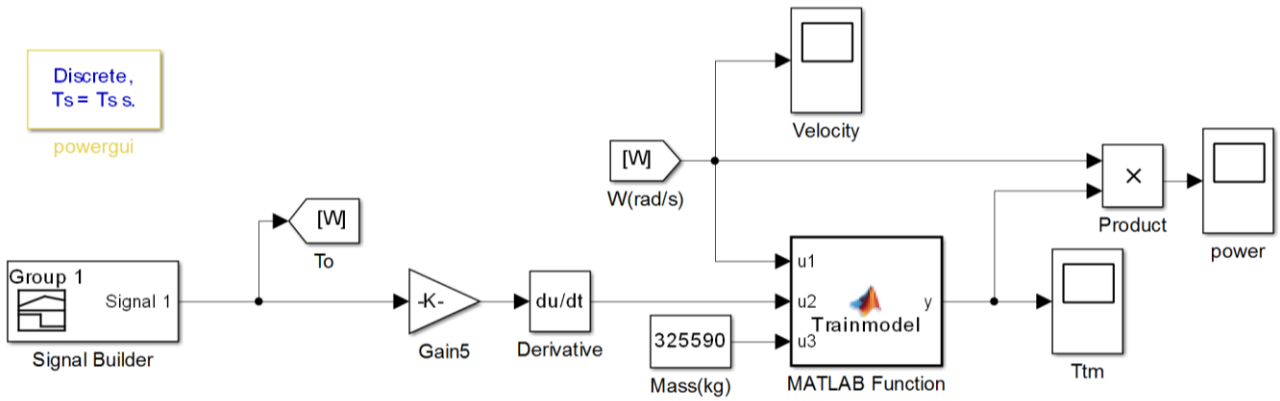

Figure 2-6: Matlab/Simulink Metro Model Block

The signal builder block is used to produce the machine speed of Figure 2-7. The motor load torque from the simulation block is shown in Figure 2-8. The torque in acceleration period starts from 16.5 kN.m and reaches 16.8 kN.m at the end of the drive cycle period. In constant speed period, torque is 5 kN.m. In deceleration period, the torque is -4 kN.m at the beginning of the period and reaches -4.45 kN.m at the end. The averaged torque in each mode is shown in Table 2-7.

Table 2-7: Averaged Motor Side Total Torque

Mode	T_{TM} kN.m
Acceleration	16.65
Constant Speed	5
Deceleration	-4.225

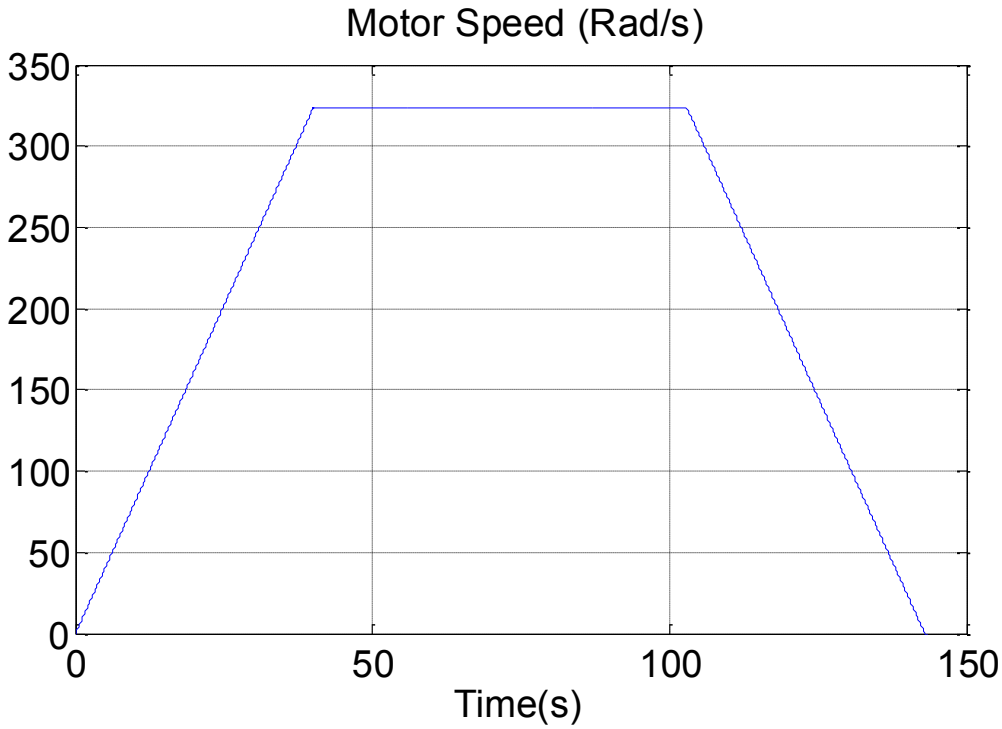

Figure 2-7: Motor Speed Calculated from MR73 Metro Train Drive Cycle

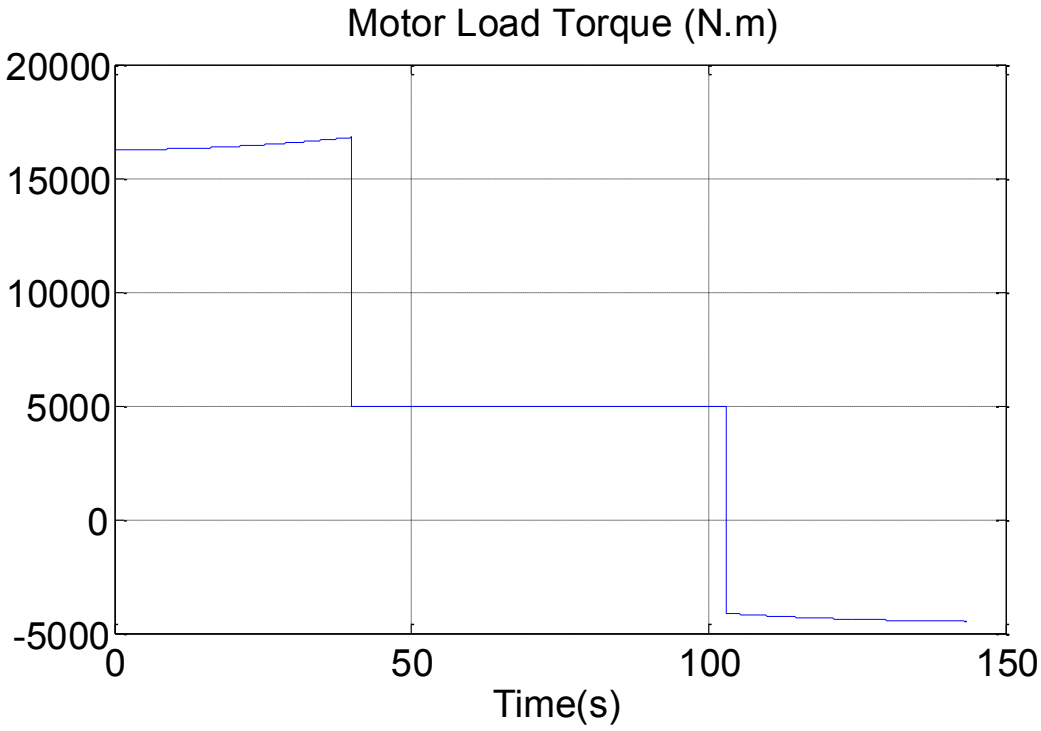

Figure 2-8: Motor Side Total Torque (T_{TM})

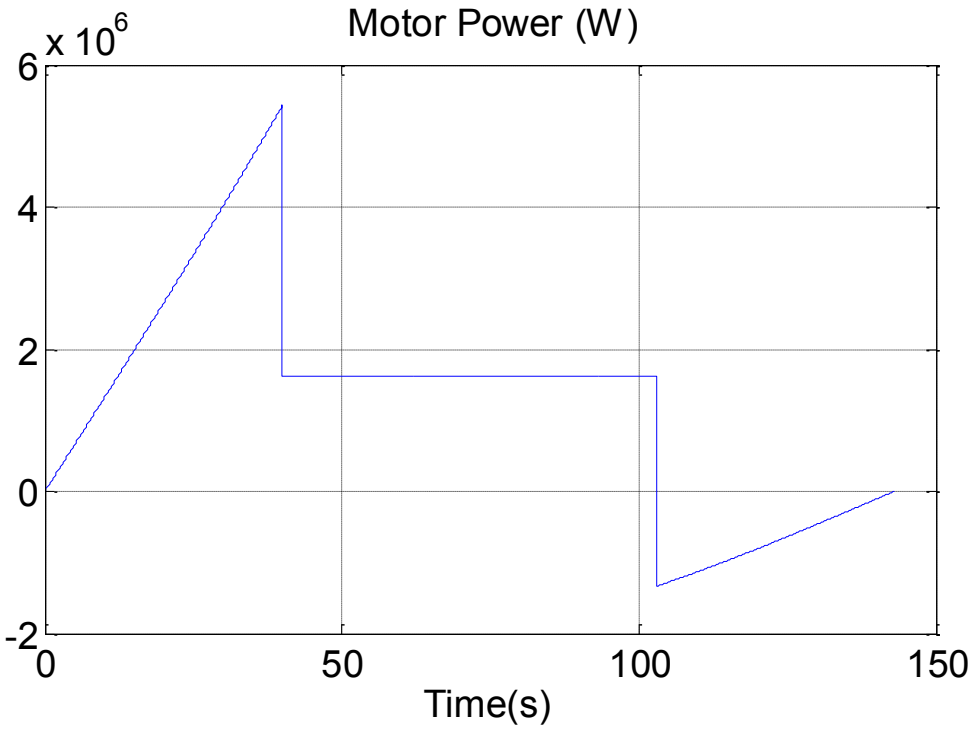

Figure 2-9: Motor Power profile

The motor total power which is multiplication of instantaneous speed and torque is shown in Figure 2-9. The average power in each mode is calculated from equation (2-37) and shown in Table 2-8.

$$\overline{P_{TR}} = \frac{1}{\Delta t}\int_{0}^{\Delta t} P_{TR}(t)dt \qquad (2\text{-}37)$$

Table 2-8: Averaged Motor Power

Mode	Power MW
Acceleration	2.7
Constant Speed	1.625
Deceleration	-0.6650

The details of calculations in each mode are presented in Appendix 2 and the results are shown in Table 2-9, Table 2-10, and Table 2-11.

Table 2-9: Cnstant Speed Mode Calculation Results

Constant speed	19.44 m/s
β	0.6°
F_{gxT}	33413 N
F_{Roll}	39254 N
F_{AD}	831 N
F_{TR}	73.498 kN
F_t	1.53 kN.m
T_t	0.735 kN.m
$\eta_{motor}\eta_{transmisson}$	0.88 %
T_{TR}	35.3 kN.m
T_{TM}	5 kN.m
T_{motor}	0.21 kN.m
E_T	25 kWh
$P_{TR,average}$	1.43 MW
$P_{TM,average}$	1.625 MW

Table 2-10: Acceleration Mode Calculation Results

Final speed	19.44 m/s
Acceleration (a)	0.48 m/s2
Acceleration time	40 s
V(t)	0.48t m/s
β	0.6°
F_{gxT}	33413 N
$F_{Roll} + F_{AD}$	45287 N
F_a	168800 N
F_{TR}	244.5 kN
F_t	5.0875 kN.m
T_t	2.445 kN.m

$\eta_{motor}\eta_{transmission}$	0.88 %
T_{TR}	117.2 kN.m
T_{TM}	16.65 kN.m
T_{motor}	695 N.m
E_T	25.9 kWh
$P_{TR,average}$	2.376 MW
$P_{TM,average}$	2.7 MW

Table 2-11: Braking Mode Calculation Results

Initial speed	19.44 m/s
Deceleration time	40 s
Deceleration (a)	-0.48 m/s^2
V(t)	-0.48t m/s
β	0.6°
F_{gxT}	33413 N
$F_{Roll} + F_{AD}$	34997N
F_{Loss}	68410 N
Distance travelled	384 m
E_{Loss}	7.3 kWh
F_a	168800 N
F_{net}	100390 N
E_{net}	10.7 kWh
T_{TR}	- 48.19 kN.m
T_{TG}	-4.156 kN.m
$T_{generator}$	-0.173 kN.m
$P_{TR,average}$	-963 kW
$P_{TG,average}$	-665 kW

Per motor load torque on motor side is shown in Table 2-12 and illustrated in Figure 2-10.

Table 2-12: Per Motor Load Torque on Motor Side

Mode	T_m N.m
Acceleration	695
Constant Speed	210
Deceleration	-173

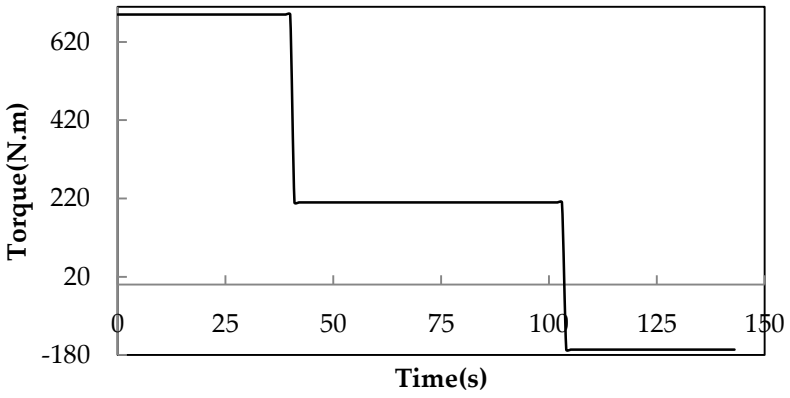

Figure 2-10: Per Motor Load Torque on Motor Side

2.6 **Summary**

In this chapter the Montreal metro train-set model MR73 was introduced. The forces acting on a moving vehicle was briefly discussed and calculated for MR73 train-set. Then, the procedure of calculating the demanded power and torque from the calculated forces was explained and a Matlab/Simulink model was developed to do this task for MR73 train-set. The power and torque calculation was done for a nine car composition. The results will be used to analyse the hybridization of the MES via ultra-capacitors in chapter 4.

Chapter 3: Ultra-Capacitor

3.1 Introduction

The ultra-capacitor will be introduced and its equivalent model will be presented. Sizing of the ultra-capacitor bank will then be done for the full and scaled metro system rating.

3.2 The Ultra-Capacitor

The ultra-capacitor is an energy storage device that is able to handle rapid fluctuations in energy level. Ultra-capacitors have a significantly lower energy density, but higher power density compared with batteries. Batteries use chemical processes to store energy which can then be released as electricity. Ultra-capacitors however store energy through charge separation. As such, the need for chemicals is reduced which allows a longer life span for ultra-capacitors.

The physics of the electrolytic capacitors were described first by Hermann von Helmholtz back in 1853. He established that the interaction between a conductor and the electrolyte inside a capacitor happens by electrostatic relations while no chemical reactions involved in the process. The ultra-capacitor is based on this

theory and it is an enhanced version of the original capacitor design [3], [20].

3.3 Equivalent Model of the Ultra-Capacitor

The basic equivalent model of an ultra-capacitor consists of [21], [22]: a) the capacitor, C_0, b) the Equivalent Series Resistance (ESR) that represents the losses during charge and discharge, c) the resistance R_{Leak} in parallel with C_0 and ESR resistance, which represents the self-discharge effect. The equivalent circuit model of the ultra-capacitor is shown in Figure 3-1.

The real ultra-capacitor model includes all the parts that are used in the basic model plus some additional parts such as a variable capacitance. The variable capacitance is nonlinearly varying with the voltage that is applied across the terminals of the ultra-capacitor. The relation is found in the measurement test data and used in the model in a lookup table. Adding more components improves the accuracy of the model. An accurate model is needed where the load power profile has rapid and repetitive changes which requires the ultra-capacitor should respond fast and equal to the load demand. However, for metro transit application an accurate model is not required since metro has an approximately fixed drive cycle. In most routes only one acceleration and one deceleration occurs per driving cycle. Therefore, the basic model shown in Figure 3-1 will be

used for simulations in this thesis.

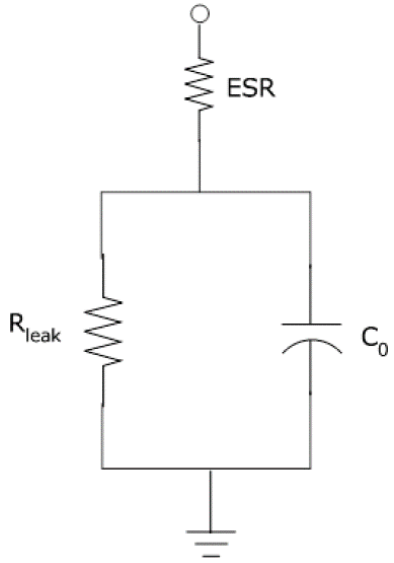

Figure 3-1: Equivalent circuit of an ultra-capacitor adopted from [3]

3.4 Criteria for Ultra-Capacitor Bank Design

The first step in ultra-capacitor bank sizing is to define the system requirements, and then determine the total energy needed. The following steps should be followed [23]:

1) The maximum ultra-capacitor bank voltage is determined when designing the system in which it is used. The voltage variation of the ultra-capacitor bank is kept between 50% and 100% of its maximum voltage. Thus, its available energy is 75% of the total energy stored according to equation (3-1) . Then, the total capacitance is determined based on equation (3-1) after substituting the demanded energy and solving for C_{Total};

$$E_{\text{Total}} = \frac{1}{2} C_{\text{Total}} \left(V^2{}_{\text{Total max}} - V^2{}_{\text{Total min}} \right) \quad (3\text{-}1)$$

2) 20-40% of C_{Total} is added to the total capacity as a safety margin to compensate the I^2R losses;

3) Next step is to calculate the number of cells in series considering maximum cell voltage;

4) Cell-level capacitance is calculated;

5) Finally, the number of cells in parallel is calculated by dividing the total capacitance on cell-level capacitance;

The above method will be used for sizing in the section 3.5.

3.5 **Ultra-Capacitor Bank Sizing**

Ultra-capacitor bank sizing for the full scale metro system rating as derived in chapter 2 will be done here. The design will be done with Maxwell 125 Volts modules.

3.5.1 Ultra-capacitor sizing for metro to provide the acceleration energy

The power profile of the metro train-set with rated load is shown in Figure 2-9. The load average power is considered to be the constant speed power which is 1.625 MW. The ultra-capacitor is discharged whenever the instantaneous power demand is greater than the average power and charged whenever the power demand is lower than the average power. Thus, the ultra-capacitor bank discharge energy which provides the acceleration energy can be computed as:

$$E_{DCH} = \frac{1}{\eta_M} \int_{T_1}^{T_2} (P_{\max} - P_{AV}) dt \qquad (3\text{-}2)$$

In calculating the motor load torque and power profiles in chapter 2, the motor and transmission efficiency were taken into account. Hence, in equation (3-2) the efficiency of 100 percent is assumed. From Figure 2-9, the instantaneous power reaches 1.625 MW at $T_1 = 12\ s$. At $T_2 = 40\ s$ the instantaneous power reaches the maximum of 5.4 MW. Therefore, from equation (3-2), the acceleration energy is:

$$E_{DCH} = \int_{12}^{40} \left(\frac{5.4 - 1.625}{40 - 12}\right) t\ dt = 98.28(\text{MJ})$$

The regenerative braking energy is calculated, it is denoted as E_{CH} since it charges the ultra-capacitor bank. T_3 is the time that instantaneous power decreases below 1.625 MW and T_4 is the time that it reaches zero. The period

between T_3 and T_4 is 40 seconds which is used in the equation (3-3) below to calculate the charging energy.

$$E_{CH} = \eta_G \int_{T_3}^{T_4} (P_{AV} - P_{\min}) dt \tag{3-3}$$

$$E_{CH} = \int_0^{40} (-\frac{1.33}{40})\ t\ dt = -26.6(MJ)$$

The ultra-capacitors are required to meet the acceleration peak energy of 98.28 MJ within an acceleration period of 28 seconds. A maximum voltage of 625 Volts is chosen for the ultra-capacitor bank [24]. Therefore from equation (3-1) the total capacitance is:

$$C_{\text{Total}} = \frac{8E_{\text{Total}}}{3\ V^2{}_{\text{Total max}}} = 671(F)$$

Ten percent capacitance is added to compensate for the I^2R losses. Hence, C_{Total} is $738\ F$. The Maxwell 125 Volts module is chosen for the sizing calculation which has 63 F of capacitance. Since the maximum voltage is 625 Volts, we can put five modules in series which gives the capacity of 12.6 F. Dividing the 738 F by 12.6 F gives the number of five module packs needed to be placed in parallel as 59. The total number of individual modules needed is therefore, $\left(\frac{738}{12.6}\right) \times 5 = 293$. The results of the sizing are shown in Table 3-1. The AES mass is 5.7 percent of the train's mass. The AES mass is 5.7 percent of the set of train's mass. The cost of 293 modules for just one train is quite high. Therefore, the size of the AES is

reduced by sizing it to provide only the peak acceleration energy, instead of the whole acceleration energy. This is presented next.

Table 3-1: Ultra-capacitor sizing for one train to provide the whole acceleration energy

Ultra-capacitor	Maxwell 125 V modules
Nominal Voltage	625 Volts DC
# of Modules	293
Energy Stored	108 MJ
Max Power	3.86 MW
Mass of modules	18.6 tons
Mass of the train	325.6 tons
Capacitance	738*F*

3.5.2 Ultra-capacitor sizing for metro to provide the peak acceleration energy

The peak acceleration energy is similarly calculated from Figure 2-9, equation (3-2) and equation (3-3). To get the peak acceleration energy, the average energy during the peak acceleration period of 28 seconds is calculated and deducted from the acceleration energy. The MES will provide the average power of 1.625 MW during acceleration.

$$E_{ACC} = \int_{12}^{40} \left(\frac{5.4 - 1.625}{40 - 12}\right) t \, dt = 98.28(\text{MJ})$$

$$E_{AV} = P_{AV} \Delta t = 1.625 \times 28 = 45.5(\text{MJ})$$

$$E_{DCH} = E_{ACC} - E_{AV} = 52.78(\text{MJ})$$

It is assumed that the AES is discharged before the beginning of the deceleration

mode. Since the braking energy is less than the 52.78 MJ ultra-capacitor bank energy capacity, it can absorb all the available regenerative braking energy.

The required peak acceleration energy is 52.78 MJ, over an acceleration period of 28 seconds. The maximum ultra-capacitor bank voltage is 625 Volts. Hence, total capacitance from equation (3-1) is:

$$C_{\text{Total}} = \frac{8E_{\text{Total}}}{3\ V^2_{\text{Total max}}} = 360(F)$$

Ten percent of capacitance is added to compensate the IR^2 loss. Hence, C_{Total} is 396 F. With the same analogy in section 3.5.1, five modules with 12.6 F capacitance are used. The total number of modules needed is $\left(\frac{396}{12.6}\right) \times 5 = 157$. The results of the sizing are shown in Table 3-2. The number and mass of the modules is more reasonable with this sizing method compared to the previous one. The AES mass is 3 percent of the set of train's mass.

Table 3-2: Ultra-capacitor sizing for one train to provide the peak acceleration energy

Ultra-capacitor	Maxwell 125 V modules
Nominal Voltage	625 Volts DC
# of Modules	157
Energy Stored	58 MJ
Max Power	2.07 MW
Mass of modules	9.954 tons
Mass of the train	325.6 tons
Capacitance	323 F

3.6 **Scaling Down Procedure**

The train drive was modeled in section 2.5 in a Matlab/Simulink function block. To get a reasonable load torque for the 2 Hp machine a few changes are made in the initial metro train modeling. As seen in Figure 2-7, in the initial metro model, the machine speed goes up to 323.2 rad/s. This speed is scaled by half since the Baldor PMDC machine in the lab cannot reach this speed. In addition, to reduce the simulation time but maintaining the same acceleration and deceleration values, the period of the drive cycle is reduced. The acceleration and deceleration periods are divided by two and the constant speed period is reduced to 43 seconds. A 17 seconds stop period is also considered at the end of the drive cycle. The stop period represents the metro stop time at each station. As such, the final modified drive cycle for simulation is as shown in Figure 3-2.

To lower torque to match the 2 Hp machine, the mass of the metro is reduced in calculations. A modification is also made on the aerodynamic drag force. Since this force depends only on velocity, it does not change by changing the mass of the train. After considering the proportion of this force in the overall tractive force, it is divided by 25 for simulation. The rest of the parameters are kept constant as the initial metro model.

Therefore the mass of the train with the maximum number of passengers was

modified to 100 kg. To examine various load profiles, simulations with 20 percent less and more than the rated mass will be done. The machine load torque profile and power profile are shown in Figure 3-3 and Figure 3-4 .

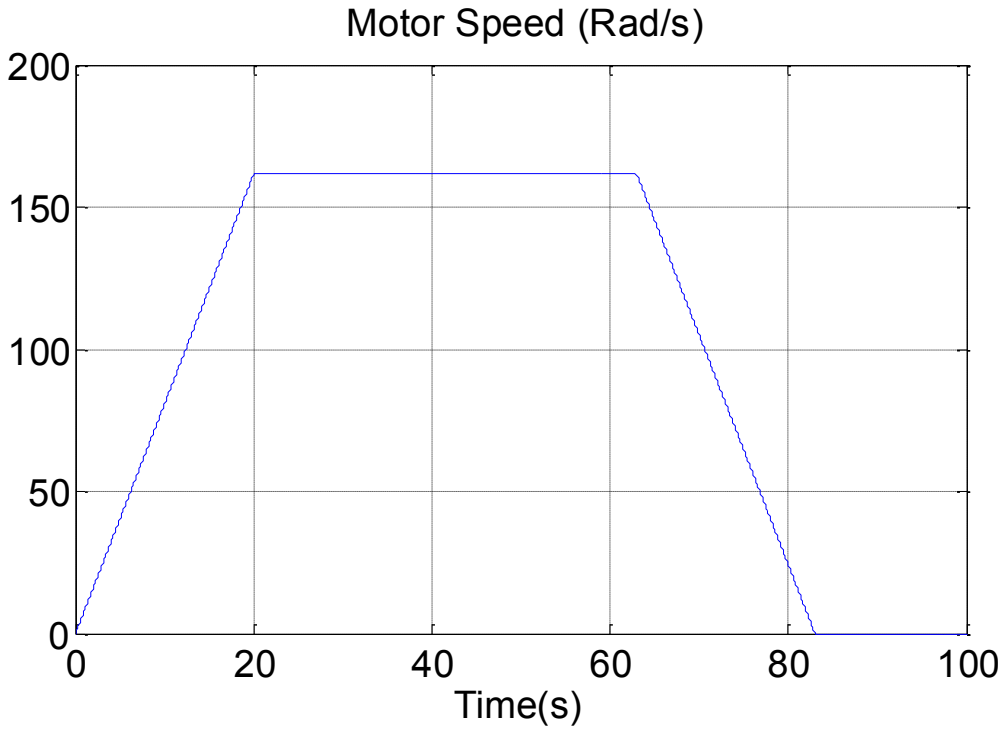

Figure 3-2: Drive cycle used for simulation

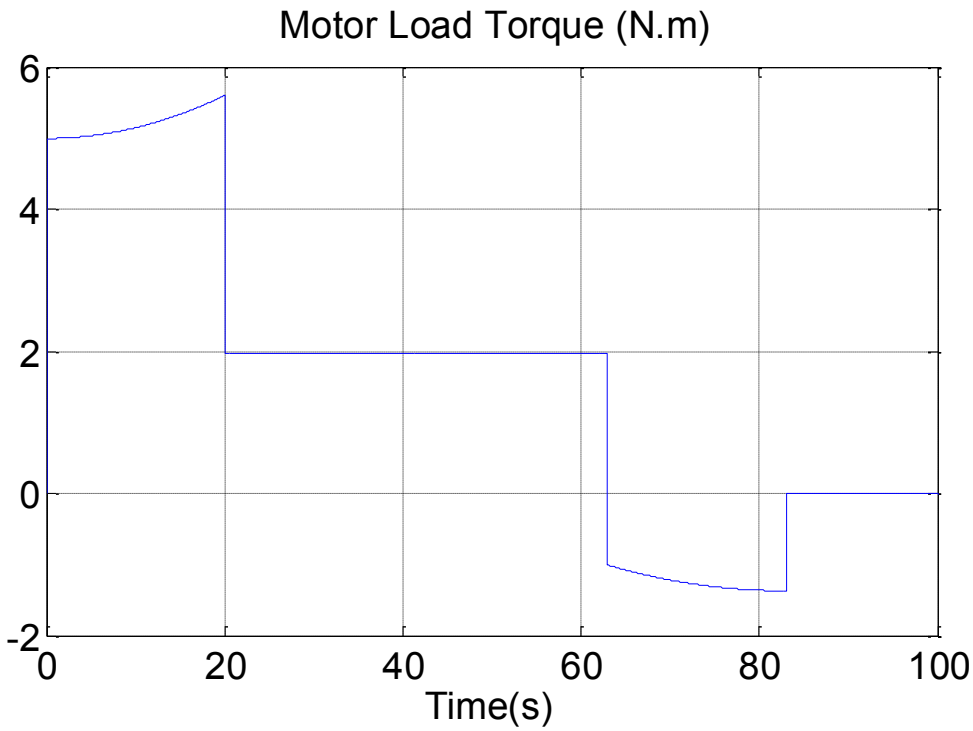

Figure 3-3: Motor load torque profile

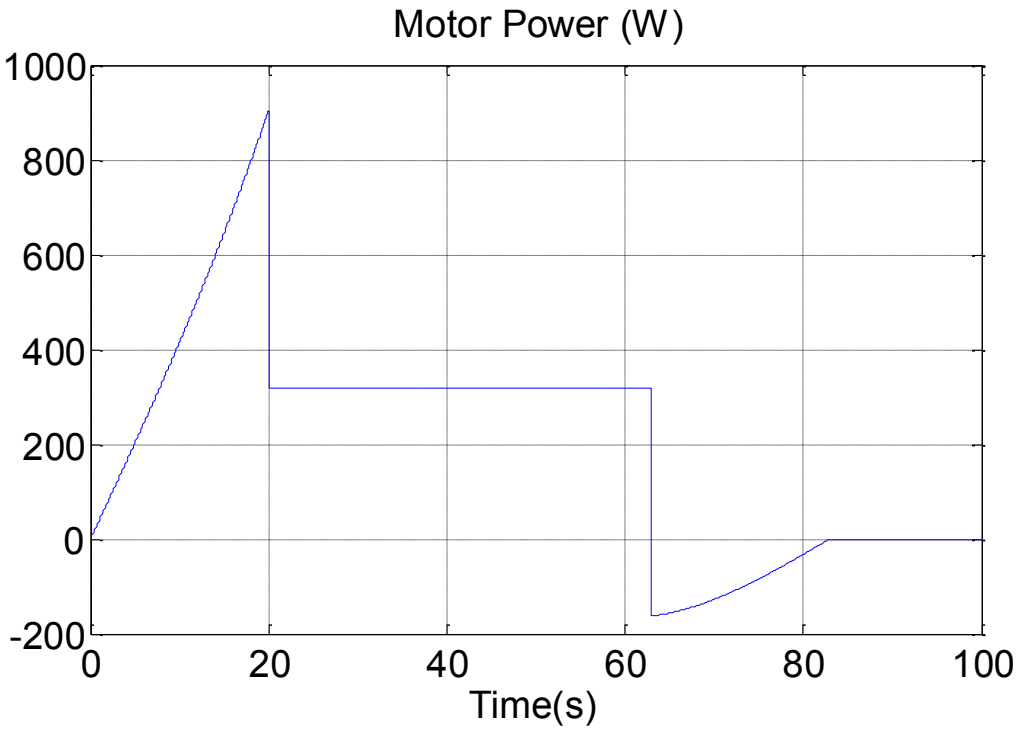

Figure 3-4: Motor power profile

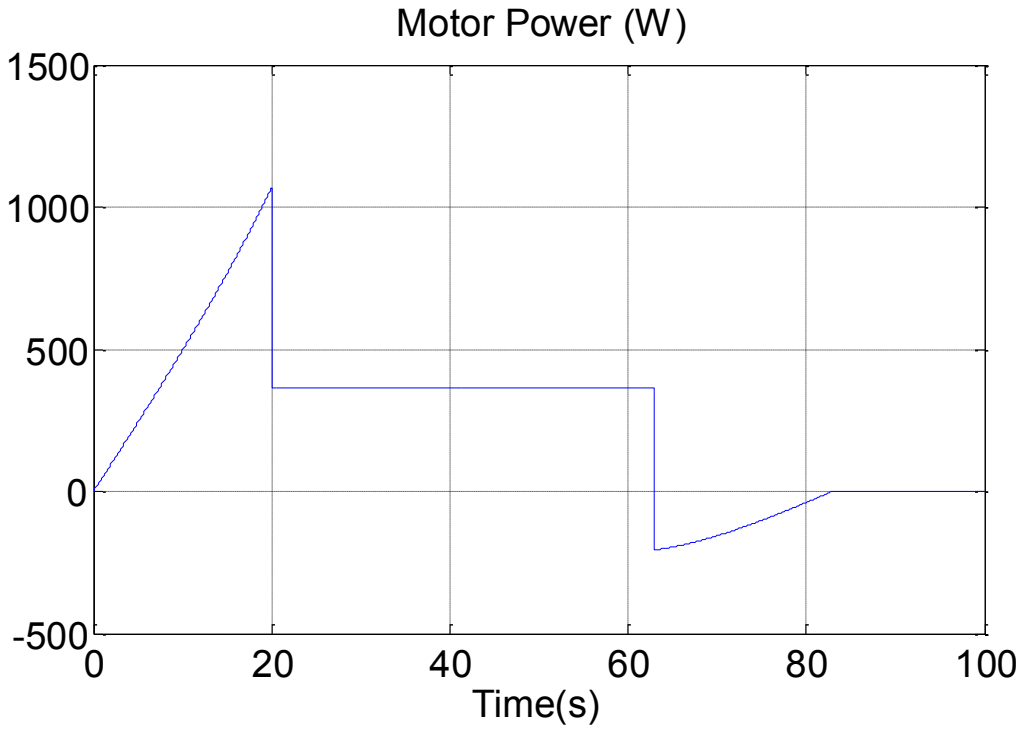

Figure 3-5: Motor power profile with 20% more than rated load

3.6.1 Ultra-capacitor sizing for the PMDC machine load to provide the acceleration energy

The power–time profile of the 2 Hp PMDC machine with rated load is shown in Figure 3-4. For sizing the ultra-capacitor bank, the power-time profile of 20 percent more than rated load, shown in Figure 3-5, will be considered since it consumes more energy during acceleration. The load average power is the constant speed power of 360 W. The ultra-capacitor is discharged whenever the instantaneous power is greater than the average power and charged whenever the power is lower than the average power. Thus, the ultra-capacitor bank

discharge energy which provides the acceleration energy is calculated from equation (3-2).

In calculating the motor load torque and power profiles, the motor and transmission efficiency is taken into account. Hence, in equation (3-2) the efficiency of 100 percent will be considered. From Figure 3-5, the instantaneous power reaches 360 W at $T_1 = 12\ s$. At $T_2 = 40\ s$ the instantaneous power reaches the maximum of 1080 W. Hence, from equation (3-2), the acceleration energy is:

$$E_{DCH} = \int_{7}^{20} \left(\frac{1080 - 360}{13}\right)\ t\ dt = 9720(\text{J})$$

The regenerative braking energy is also calculated. T_3 is the time that instantaneous power decreases below 360 W and T_4 is the time that it reaches zero. The period between T_3 to T_4 is 20 seconds which is used in equation (3-3) to calculate the regenerative energy. The generator efficiency is assumed to be 100 percent since it is already considered in deriving the load power.

$$E_{CH} = \int_{0}^{20} \left(-\frac{200}{20}\right)\ t\ dt = -2000(J)$$

The regenerative braking energy is about 15 percent of the acceleration peak energy. Now ultra-capacitor sizing will be done for the calculated energy of 9720 J. The maximum voltage of the ultra-capacitor bank is 40 Volts. Therefore from equation (3-1) the total capacitance is:

$$C_{\text{Total}} = \frac{8E_{\text{Total}}}{3\ V^2_{\text{Total max}}} = 16.2(F)$$

Twenty percent of capacitance is added to compensate the I^2R losses. Hence, C_{Total} is 19.44 F. The Maxwell 310 F cells are chosen for sizing [25]. Since the maximum voltage is 40 Volts, we can put sixteen cells in series which gives the capacitance of 19.375 F. The calculated total capacitance is close enough to the designed capacitance, hence no packs in parallel are needed. The results of the sizing calculation are shown in Table 3-3.

Table 3-3: Ultra-capacitor sizing for PMDC machine load to provide the whole acceleration energy

Ultra-capacitor	Maxwell 310 F Cells
Nominal Voltage	40 Volts DC
# of cells	16
Energy Stored	11625 J
Max Power	894 W
Mass	0.992 kg
Mass of the train	120 kg
Capacitance	19.375 F
ESR	0.0.0352 ohms

The mass of the ultra-capacitor bank is 0.83 percent of the set of train cars' mass. With the same analogy used for the first sizing for the initial metro model in section 3.5.1, the size of the AES will be reduced by sizing it only to provide the peak acceleration energy in the next section.

3.6.2 Ultra-capacitor sizing for PMDC machine load to provide the peak acceleration energy

The peak acceleration energy is calculated from data in Figure 3-5, equation (3-2) and equation (3-3). To get the peak acceleration energy the average energy during the peak acceleration period of 13 seconds is calculated and deducted from the acceleration energy. The MES will provide the average power of 360 W during acceleration.

$$E_{ACC} = 9720(\text{J})$$

$$E_{AV} = P_{AV}\Delta t = 360 \times 13 = 4680(\text{J})$$

$$E_{DCH} = E_{ACC} - E_{AV} = 5040(\text{J})$$

It is assumed that the AES is discharged before beginning of the deceleration mode. Since the braking energy is less than the 5040 J ultra-capacitor bank energy capacity, it can store the regenerative braking energy.

The required energy is the acceleration peak energy of $E = 5040$ J. The peak acceleration period is 13 seconds. The maximum ultra-capacitor bank voltage is 40 volts. Hence, total capacitance from equation (3-1) is:

$$C_{\text{Total}} = \frac{8E_{\text{Total}}}{3\ V^2{}_{\text{Total max}}} = 8.4(F)$$

Twenty percent of capacitance is added to compensate the I^2R losses. Hence,

C_{Total} is 10.08 F. The Maxwell 150 F cells are chosen for sizing. Since the maximum voltage is 40 Volts, we can put sixteen cells in series which gives a capacitance of 9.375 F. The capacitance is close enough to the designed capacitance, hence no packs in parallel are needed. The results of the sizing are shown in Table 3-4.

Table 3-4: Ultra-capacitor sizing for the PMDC machine load to provide the peak acceleration energy

Ultra-capacitor	Maxwell 150 F cells
Nominal Voltage	40 Volts DC
# of cells	16
Energy Stored	5625 J
Max Power	433 W
Mass	0.512 kg
Mass of the train	120 kg
Capacitance	9.375 F
ESR	0.224 ohms

The mass of the ultra-capacitor bank is 0.43 percent of the set of train's mass. This scaled down sizing represents the second sizing for the initial metro model in section 3.5.2, where it was shown to be more technically and financially reasonable, compared to the first sizing method.

3.7 **Summary**

The ultra-capacitor was introduced in this chapter. A suitable ultra-capacitor model was selected for the metro transit application and the choice of model was

justified. A sizing method was developed then applied for the Montreal metro system. Since the results of the sizing to supply the whole acceleration energy were not financially and technically reasonable, a second sizing method, where the AES provides only the peak acceleration energy was developed. The results of the second sizing method were acceptable.

For the purpose of simulation, the initial full scale metro model was scaled down. The scaling down procedure was explained, then the sizing procedure was done for the new model. The two previously developed sizing methods were applied to the scaled model, where the results are used in chapter 6.

Chapter 4: DC/DC Converters

4.1 Introduction

The bidirectional DC/DC converter topology used in this thesis is a buck-boost topology shown in Figure 4-1. It interfaces the ultra-capacitor to the load DC bus. In this section we will go through the operation principals of the bidirectional DC/DC converter in detail. First, the design and operation of the converter is explained. Secondly, the filter capacitor of the converter as well as the components is sized according to the operation requirements. Thirdly, the average model of the converter is presented. Due to its multiple switching stages, the operation of a DC/DC converter is nonlinear, hence, its average model is needed to capture the converter performance. Finally, PI controllers are designed to remove the steady state errors and capture the transient response of the converter. The sizing of components, controller design and modeling are conducted assuming an ideal converter. In practical design, it is crucial that the power losses and efficiency aspects are taken into account [3], [26], [27].

A boost DC/DC converter is needed to be interfaced to the DC rail to control the power flow from the DC rail to the system. The same procedure as the buck-

boost is then followed for the DC rail boost converter and controller design.

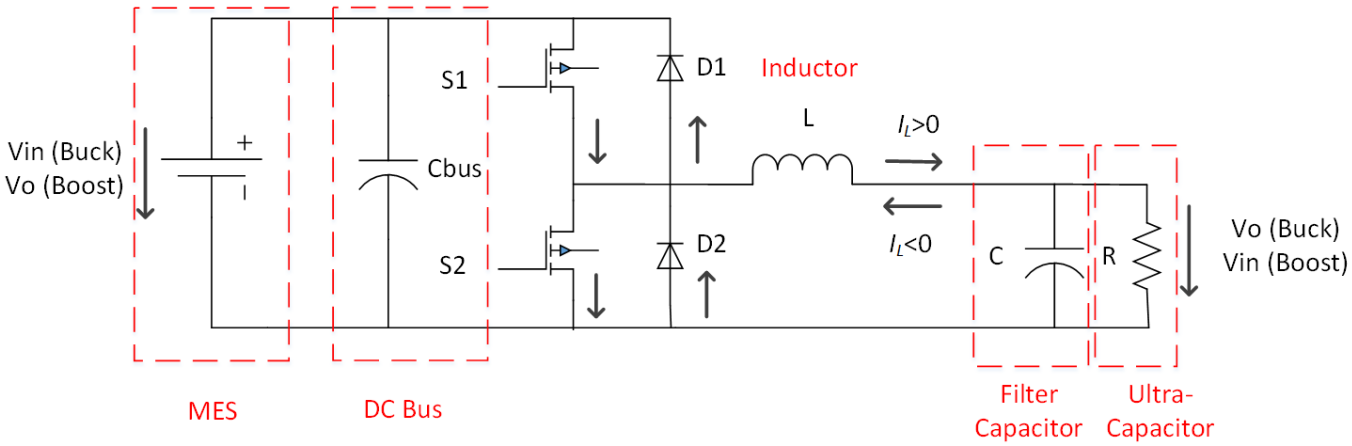

Figure 4-1: Schematic of the bidirectional DC/DC buck-boost converter [28]

4.1.1 Operation Principals of the Ultra-Capacitor Bidirectional DC/DC Converter

The ultra-capacitor two-quadrant switch mode converter is shown in Figure 4-1. The motor drive connected across the DC bus and the MES, DC rail, boost converter are not shown in Figure 4-1. This converter has two operation modes; step-down buck and step-up boost. It consists of two IGBT switches, S1/S2 along with the anti-parallel diodes D1/D2 in a half bridge configuration. When active power is transferred from the DC bus to the Ultra-capacitor, the average load current is positive, $I_L > 0$. When active power is transferred in the opposite direction from the ultra-capacitor to the DC bus, the average load current is negative, $I_L < 0$. It works in a step-down buck mode in the first case when

$I_L > 0$, and in a step-up boost mode in second case when $I_L < 0$ [3] , [29].

4.1.2 Buck mode

When the converter is operating in buck mode, power is transferred from the DC bus to the ultra-capacitor bank. The average inductor current is positive, $I_L > 0$. The ultra-capacitor voltage is defined as V_O and the DC bus voltage as V_{in}.

The basic characteristics in the buck mode are as follows. The input voltage is larger than the output voltage. The switch S1 opens and closes with a given switching frequency $T_s = t_{on} + t_{off}$. When the switch is closed during t_{on}, the inductor L voltage is equal to $v_L = V_{in} + V_O$. The diode D2 is reverse biased and does not conduct. The inductor stores energy and the resultant current increases at a constant rate as a function of time $i_L = \frac{(V_{in} - V_O)\ t}{L}$.

After t_{on}, the current is equal to $i_{L,peak} = \frac{(V_{in} - V_O)\ t_{on}}{L}$. Magnetic energy equivalent to $W = \frac{1}{2}\ L\ i^2_{L,peak}$ is now stored in the inductor. When the switch opens, the diode D2 becomes forward biased and the current begins to decrease with a constant rate of $i_L = i_{L,peak} - \frac{V_O\ t}{L}$. The current reaches its minimum value after t_{off}.

In steady state, this current is equal to the current value at the start of the switching period. The inductor has now transferred all of the stored energy to the load. Plots of the inductor current, voltage, and the switch value (on=1, off=0) can be seen in Figure 4-2.

The volt-seconds energy absorbed by the inductor during, t_{on}, is equal to area A in the v_L plot. The energy out during the discharge interval, t_{off}, is equal to area B. These areas are equal, hence:

$$Area\ A = Area\ B \tag{4-1}$$

$$(V_{in} - V_O)\ t_{on} = V_O t_{off} \tag{4-2}$$

$$\frac{V_O}{V_{in}} = \frac{t_{on}}{t_{on} + t_{off}} = \frac{t_{on}}{T_s} = D \tag{4-3}$$

where D is the duty ratio. The output filter capacitor C is assumed to be large enough such that the output DC voltage is assumed to be constant, $v_O \cong V_O$. The ripple-frequency element of the inductor current, $i_{L,ripple}$, sees a much smaller impedance through the filter capacitor than through the load resistance. As such, $i_C \simeq i_{L,ripple}$.

The correlation between the average currents can be found by supposing that the input power P_{in} equals the output power P_O neglecting losses related to the circuit components:

$$P_{in} = P_O \tag{4-4}$$

$$V_{in}\, I_{in} = V_O I_O \tag{4-5}$$

$$I_{in} = \frac{V_O}{V_{in}} I_O = D\, I_O \tag{4-6}$$

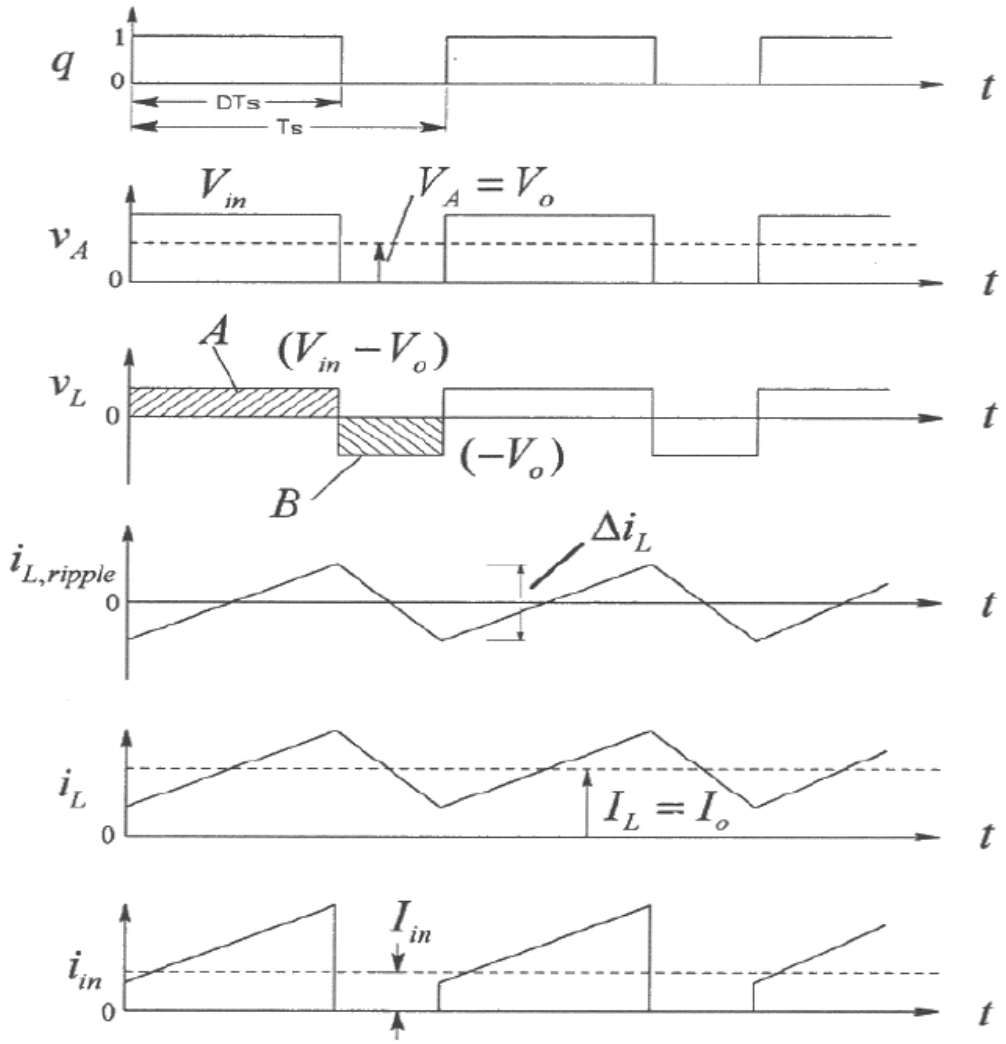

Figure 4-2: Graphical Representation of the inductor current, voltage and the switch value in buck mode. v_a is the voltage across the diode D2 [3]

4.1.3 Boost mode

When the bidirectional converter is operating in boost mode, power is transferred from the ultra-capacitor (load side) to the DC bus. The average inductor current is hence negative, $I_L < 0$. The ultra-capacitor voltage is titled $V_{in}(boost)$ and the DC bus voltage is $V_O(boost)$. In this mode, it is the switch S2 and diode D1 that are actively transferring energy. The inductor voltage oscillates between V_{in} and $V_O - V_{in}$. Plots of the inductor current, voltage, and the switch value (on=1, off=0) can be seen in Figure 4-3.

The average inductor voltage is zero during one period, so the volt-second areas are equal in magnitude as equation (4-1). Therefore:

$$V_{in}\ t_{on} = -(V_{in} - V_O)\ t_{off} \tag{4-7}$$

$$\frac{V_O}{V_{in}} = \frac{t_{on} + t_{off}}{t_{off}} = \frac{T_S}{t_{off}} = \frac{1}{1-D} \tag{4-8}$$

The average diode current I_{diode} equals the output current I_0. The ripple-frequency current component of the diode flows to the capacitor C_{bus}. The reason is that the path through the capacitor has a lower impedance than the load. Therefore, the capacitor current can be expressed as:

$$i_C(t) = i_{diode,ripple}(t) = i_{diode} - I_O \tag{4-9}$$

Equating the input power with the output power yields the following equation for the average currents:

$$\frac{I_O}{I_{in}} = 1 - D \tag{4-10}$$

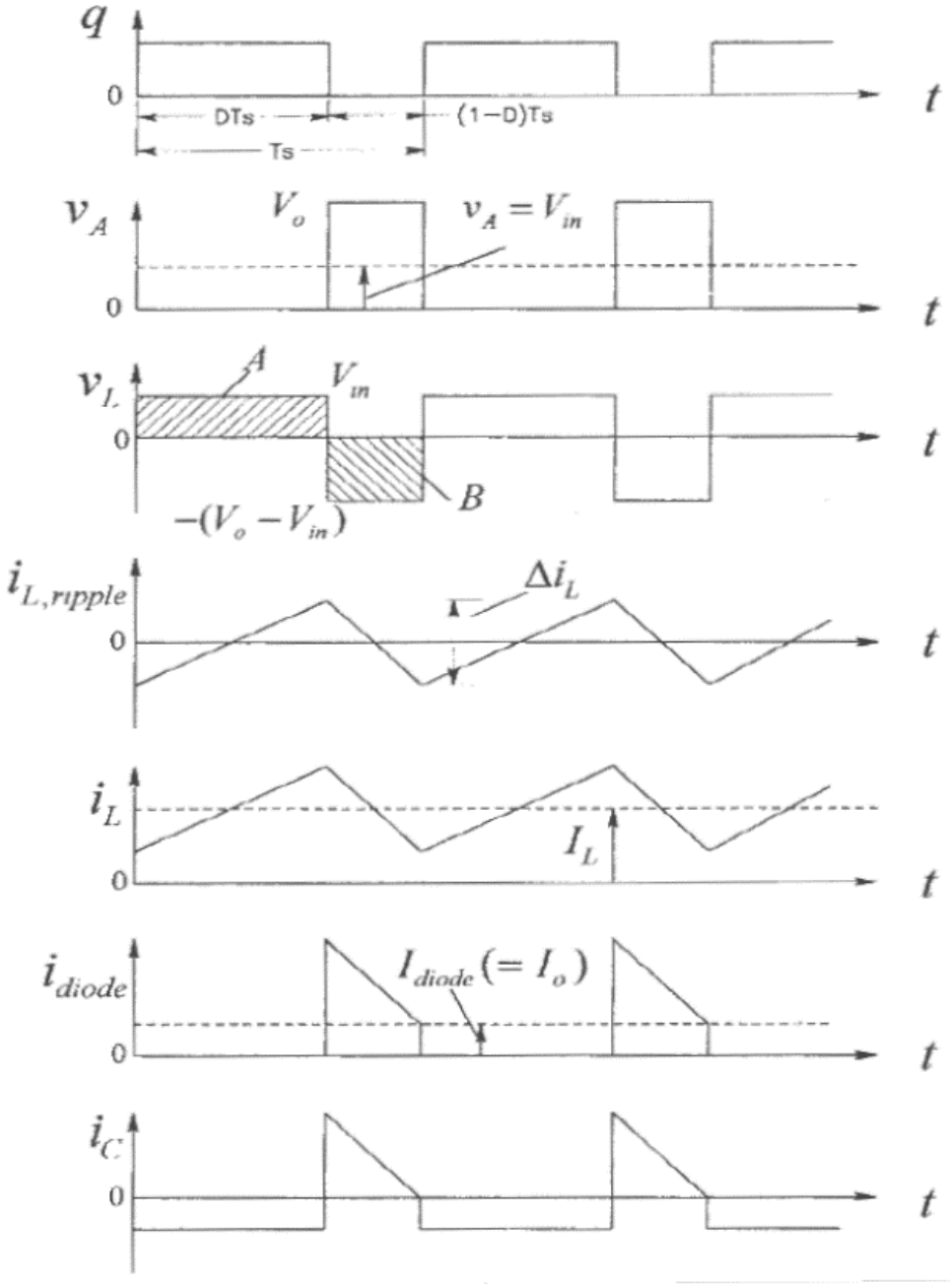

Figure 4-3: Graphical Representation of the inductor current, voltage and the switch value in boost mode [3]

Table 4-1: Predefined conditions in buck mode

V_{in}	180 Volts
V_o	20 - 40 Volts
f_S	10 kHz
$P_{O,nominal}$	1 kW
Range of P_O	(25 to 100 %)$P_{O,nominal}$
Output ripple($\Delta V_O/V_O$)	5 %

4.2 Filter Capacitor and Inductor Design of the Ultra-Capacitor Converter

4.2.1 Buck mode

In the selected converter topology the predefined operation conditions are presented in Table 4-1. Given a constant input voltage, V_{in}, a varying output voltage, V_O, constant switching frequency, f_S, and a chosen rated output power, Po, the optimal values of the filter capacitor and inductor can be calculated. Their ratings should be minimized in order to cut converter costs [30].

4.2.2 Design of the inductor in buck mode

$L_{\min}$ is the lowest inductance value required to keep the converter operating at the boundary of buck mode under all conditions. The conditions are based on the

predefined electrical parameters and states[1].

The inductor current decreases by lowering the duty ratio i.e. increasing the off time. The boundary value for the inductor current is defined as:

$$I_{LB} = \frac{1}{2} i_{L,peak} = \frac{t_{on}}{2L}(V_{in} - V_O) = \frac{DT_S}{2L}(V_{in} - V_O) \tag{4-11}$$

Rearranging the above equation gives:

$$L_{\min} = \frac{D}{2\ I_{LB} f_S}(V_{in} - V_O) \tag{4-12}$$

The average marginal load and inductor current is a function of P_O and V_O:

$$I_{LB} = I_{OB} = \frac{P_O}{V_O} \tag{4-13}$$

Choosing the lowest predefined value of 25 % of the nominal power, maximum D and minimum V_O, gives in the end the maximum value of $L_{\min}$ from equation (4-13):

$$L_{\min} = \frac{D \cdot (V_{in} - V_O)}{2 \cdot \frac{P_O}{V_O} \cdot f_S} = \frac{0.22 \cdot (180 - 20)}{2 \cdot \frac{250}{20} \cdot 10000} = 146.5 \mu H$$

The calculated inductance is multiplied with twenty, in order to ensure an

---

[1] In one-quadrant buck or boost-converters this boundary is known as the boundary of discontinuous conduction mode (DCM). When the converter goes in DCM, I_L cannot reverse through the diode, causing a zero inductor current for a finite time interval. In the bidirectional half-bridge converter this boundary is not discontinuous, since it is the boundary at which the current changes direction [3].

adequately reduced ripple current. This gives $L_{\min} = 3mH$. Current ripple for the maximum value of duty ratio in buck mode is calculated from:

$$\Delta i_L = \frac{V_{in} \cdot D(1-D)}{L_S \cdot f_S} \tag{4-14}$$

The current ripple from equation (4-14) is:

$$\Delta i_L = \frac{180 \cdot 0.22(0.77)}{0.003 \cdot 10000} = 1.02 \ \ amps$$

1.02 amps is an acceptable ripple for the ultra-capacitor current.

4.2.3 Design of the filter capacitor in buck mode

For calculating the optimum capacitance value, one can assume that the full ripple current flows through the capacitor, $i_c(t) \simeq i_{L,ripple}$, while the average current flows to the load, $I_L = I_O$. The peak-to-peak voltage ripple at the output ΔV_O is given by:

$$\Delta V_O = \frac{\Delta Q}{C} = \frac{1}{C}\frac{1}{2}\frac{\Delta i_L}{2}\frac{T_S}{2} \tag{4-15}$$

The peak-to-peak current ripple is defined by:

$$\Delta i_L = \frac{1}{L}(V_{in} - V_O) \ \ D \ T_S = \frac{1}{L} V_O (1-D) T_S \tag{4-16}$$

Substituting equation (4-16) into equation (4-15) gives:

$$\Delta V_O = \frac{T_S}{8C}\frac{V_O}{L}(1-D)T_S \tag{4-17}$$

Rearranging equation (4-17) with respect to the capacitance C gives:

$$C = \frac{T_S}{8L}\frac{V_O}{\Delta V_O}(1-D)T_S \qquad (4\text{-}18)$$

The capacitance is inversely proportional to L and the square of the switching frequency. It is also proportional to $\frac{t_{off}}{T_S} = (1-D)$. Using equation (4-18) with the calculated value for $L_{\min} = 0.3mH$ and required voltage ripple value of five percent, we see that the capacitance has a maximum when the duty ratio D is at its minimum. That is $D = 0.111$ in the buck mode when $V_O = 20\ Volts$. Substituting $f_S = \frac{1}{T_S}$ in equation (4-18):

$$C = \frac{(1-D)}{f_S{}^2 \cdot 8L_{\min}} \cdot \frac{V_O}{\Delta V_O} = \frac{(1-0.111)}{(10000)^2 \cdot 8 \cdot 0.0003 \cdot 0.05} = 74(\mu F)$$

The calculated capacitor is multiplied with ten, in order to ensure a sufficiently reduced voltage ripple. This gives $C = 0.74\ mF$. The calculated value of C gives the five percent voltage ripple by rearranging equation (4-17) and $L_{\min}$ equal to $3mH$:

$$\frac{\Delta V_O}{V_O} = \frac{T_S^2(1-D)}{8LC} = \frac{(1-0.111)}{8 \cdot 0.003 \cdot 0.00074 \cdot (10000)^2} = 0.05\%$$

The value of voltage ripple is below the required five percent ripple hence acceptable.

4.2.4 Boost mode

Table 4-2: Predefined conditions in boost mode

V_{in}	20 - 40 Volts
V_o	180 Volts
f_S	10 kHz
$P_{O,nominal}$	1 kW
Range of P_O	(50 to 100 %)$P_{O,nominal}$
Output ripple($\Delta V_O/V_O$)	5 %

The operation conditions in boost mode are predefined according to Table 4-2.

4.2.5 Design of the inductor in Boost Mode

The boundary value for the load current is defined as:

$$I_{OB} = \frac{T_S V_O}{2L} D(1-D)^2 \tag{4-19}$$

The minimum inductance required is then given by:

$$L_{\min} = \frac{T_S V_O}{2I_{OB}} D(1-D)^2 \tag{4-20}$$

The independent variables are now P_O and V_{in}. The average load boundary current can be stated as $I_{OB} = \frac{P_O}{V_O}$. Expressing D in terms of V_O and V_{in}, with $(1-D)^2 = (\frac{V_{in}}{V_O})^2$, and replacing I_{OB} in equation (4-20) gives:

$$L_{\min} = \frac{V_O^2 (\frac{V_O - V_{in}}{V_O})(\frac{V_{in}}{V_O})^2}{2\ P_O f_S} = \frac{(\frac{V_O - V_{in}}{V_O})(V_{in})^2}{2\ P_O f_S} \tag{4-21}$$

One realizes that $L_{\min}$ has a maximum when P_O is at its minimum. Differentiating equation (4-21) with respect to V_{in} gives a maximum when $V_{in} = \frac{2}{3}V_O = 120$ Volts. However, V_{in} falls within 20-40 Volts. To calculate $L_{\min}$ in this case, we simply assume the maximum duty ratio with I_0 calculated from the minimum output power with gives $L_{\min}$ from equation (4-21) as:

$$L_{\min} = \frac{180V \cdot 0.888 \cdot (0.111)^2}{2 \cdot (\frac{500W}{180V}) \cdot 10kHz} = 36(\mu H)$$

This is less than the minimum value that was derived for the buck mode. Therefore, the minimum value of the buck mode will be used.

The inductor current ripple in boost mode is calculated with the same equation (4-14) as in buck mode. The maximum inductor current ripple with $L_{\min} = 3mH$ for boost mode is:

$$\Delta i_L = \frac{V_{in,\max} \cdot D_{\max}(1 - D_{\max})}{L_S \cdot f_S} = \frac{40V \cdot 0.88(0.111)}{3(mH) \cdot 10(kHz)} = 0.13(amps)$$

This current ripple can be removed by the DC bus capacitor.

4.2.6 Design of the filter capacitor in boost mode

The capacitance at the load side should absorb all the ripple current that flows through D2. The peak to peak voltage ripple can then be expressed as:

$$\Delta V_O = \frac{\Delta Q}{C_{bus}} = \frac{I_O \cdot D \cdot T_S}{C_{bus}} \tag{4-22}$$

Reformulating equation (4-22) and articulating it in terms of V_{in} and P_O gives:

$$C_{bus} = \frac{I_O \cdot D \cdot T_S}{V_O} \cdot \frac{V_O}{\Delta V_O} = \frac{P_O(V_O - V_{in})}{V_O^3 \cdot f_S \cdot 0.05} \tag{4-23}$$

In this case C_{bus} is independent of the inductance value. C_{bus} is maximum when V_{in} is at its minimum and P_O is at its maximum. This leads to:

$$C_{bus} = \frac{1000 \cdot (180 - 20)}{(180)^3 \cdot 10000 \cdot 0.05} = 55(\mu F)$$

We multiply the minimum value with five in order to ensure a low current ripple. The calculated value of C_{bus} is $0.3mF$, with maximum $\frac{V_{in}}{V_O} = (1 - D)$, gives voltage ripple from equation (4-17) as:

$$\frac{\Delta V_O}{V_O} = \frac{T_S^2(1-D)}{8LC} = \frac{0.22}{8 \cdot 0.003 \cdot 0.0003 \cdot (10000)^2} = 0.03\%$$

This is less than the maximum allowable ripple of five percent. The model can be simplified since the ultra-capacitor bank acts also as a filter capacitor. Therefore, a filter capacitor is not used on the load side.

4.3 **PWM Control of DC/DC Converters**

Pulse Width Modulation technique (PWM) is a common switching method for DC/DC converters. With a given input voltage/current, the average output

voltage/current is controlled by controlling the switching of the semiconducting transistor. The switch control signal, $q(t)$, with a constant frequency, f_S, controls the state (on or off) of the transistor which typically has a value of unity when the transistor is on (short circuit) and the value zero when the transistor is off (open circuit). It is generated by comparing a control voltage V_c with a repetitive waveform voltage V_r of a frequency equal to f_S. When V_c is higher than V_r, the comparator generates the switch control signal, $q(t)$, that is sent to the transistor gate, turning it on. When V_c is lower than V_r, the comparator generates an output signal $q(t) = 0$. Example of a comparator signal with a saw tooth voltage V_r compared with the control input V_c can be seen in Figure 4-4. The duty ratio D can be expressed in terms of V_c and the peak of the saw tooth waveform, $\hat{V}_r$, as [3]:

$$D = \frac{t_{on}}{T_S} = \frac{v_C}{\hat{V}_r} \tag{4-24}$$

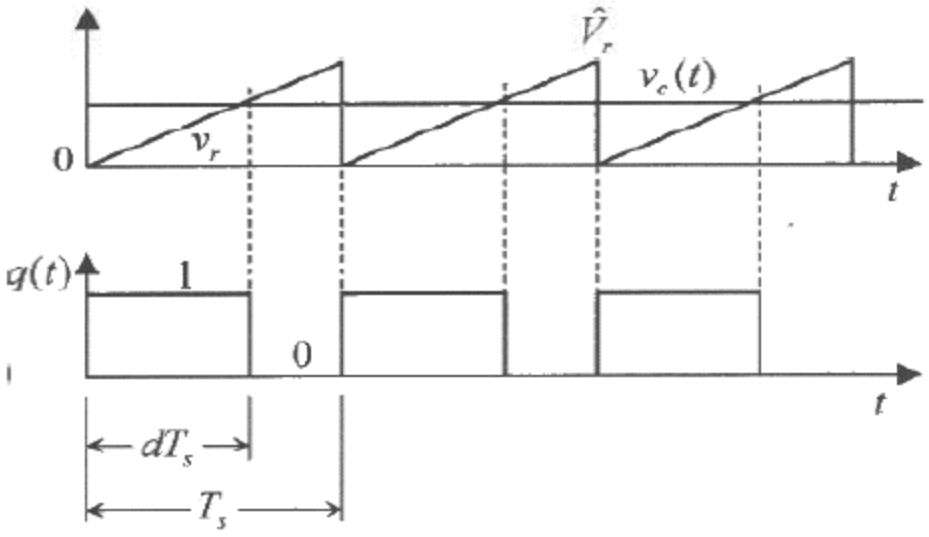

Figure 4-4: Pulse Width Modulation, comparator signal $v_C(t)$ compared with producing $v_r$the output $q(t)$ [3]

4.4 The Dynamic Average Model of the Ultra-Capacitor DC/DC Converter

Due to its multiple switching stages, the operation of a DC/DC converter is nonlinear. To be able to capture the converter performance it is beneficial to represent the average model of the converter circuit. Under a dynamic state, the converter duty-ratio and the average values of voltages and currents are time variant. Averaging results in a linear model of the plant linearized around the steady state DC operating point, assuming small time varying component known as AC perturbations. The average quantities can be expressed as the sum of its steady state DC value and the AC perturbations. Here, we will assume an ideal

converter and thereby ignore power losses in switches and diodes [27], [31].

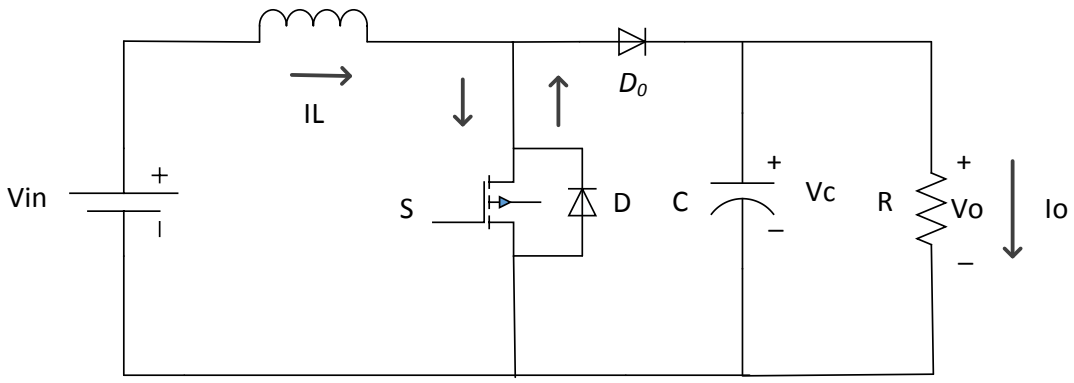

Figure 4-5: Boost DC/DC Converter

Although the ultra-capacitor converter is a bidirectional buck-boost, averaging is conventionally done for either boost or buck mode. The transfer functions derived from the buck or boost average model are used for controllers design. Through manual controller optimization, the controllers implemented in the buck-boost converter work for both modes. In this case, averaging is done for boost mode. For a boost converter in switch mode shown in Figure 4-5, the average voltage and current relationships in DC steady state are as follows:

$$V_O = \frac{V_{in}}{1-D} \tag{4-25}$$

$$I_O = I_{in} \cdot (1-D) = I_L \cdot (1-D) \tag{4-26}$$

State equations for each interval of operation are as the following:

Switch S is on:

$$L\frac{di_L}{dt} = v_{in} \tag{4-27}$$

$$C\frac{dv_O}{dt} = -\frac{v_O}{R} \tag{4-28}$$

Switch S is off:

$$L\frac{di_L}{dt} = v_{in} - v_O \tag{4-29}$$

$$C\frac{dv_O}{dt} = i_L - \frac{v_O}{R} \tag{4-30}$$

Averaging state equations over a switching cycle gives:

$$L\frac{di_L}{dt} = v_{in} - (1-D)\cdot v_O \tag{4-31}$$

$$C\frac{dv_O}{dt} = (1-D)\cdot i_L - \frac{v_O}{R} \tag{4-32}$$

Introducing perturbation in state variables such as the following:

It is assumed that $\bar{v}_C = \bar{v}_O$.

$$\begin{gathered}\bar{i}_L = I_L + \tilde{i}_L(t)\\ \bar{v}_{in}(t) = V_{in} + \tilde{v}_{in}(t)\\ \bar{v}_O(t) = V_O + \tilde{v}_O(t)\\ \bar{D}(t) = D + \tilde{d}(t)\end{gathered}$$

The letters with a bar '¯' represent the average dynamic values, the upper case letters are the steady state average values, and the letters with '~' represent the small signal perturbation. Substituting the average dynamic values in equation (4-31) and equation (4-32):

$$\begin{gathered}L\frac{d(I_L + \tilde{i}_L(t))}{dt} = V_{in} + \tilde{v}_{in}(t) - (1 - D - \tilde{d}(t))\cdot(V_O + \tilde{v}_O(t))\\ C\frac{d(V_O + \tilde{v}_O(t))}{dt} = (1 - D - \tilde{d}(t))\cdot(I_L + \tilde{i}_L(t)) - \frac{(V_O + \tilde{v}_O(t))}{R}\end{gathered}$$

Equating AC and DC quantities and proceeding with AC equations (neglecting

second order AC quantities) we get:

$$L\frac{d\tilde{i}_L(t)}{dt} = \tilde{v}_{in}(t) - (1-D)\cdot\tilde{v}_O(t) + V_O\cdot\tilde{d}(t) \tag{4-33}$$

$$C\frac{d\tilde{v}_O(t)}{dt} = (1-D)\cdot\tilde{i}_L(t) - I_L\cdot\tilde{d}(t) - \frac{V_O}{R} \tag{4-34}$$

Taking Laplace transform from equation (4-33) and equation (4-34) we get:

$$s\cdot L\cdot\tilde{i}_L(s) = \tilde{v}_{in}(s) - (1-D)\cdot\tilde{v}_O(s) + V_O\cdot\tilde{d}(s) \tag{4-35}$$

$$s\cdot C\cdot\tilde{v}_O(s) = (1-D)\cdot\tilde{i}_L(s) - I_L\cdot\tilde{d}(s) - \frac{\tilde{v}_O(s)}{R} \tag{4-36}$$

or

$$(s\cdot C + \frac{1}{R})\cdot\tilde{v}_O(s) = (1-D)\cdot\tilde{i}_L(s) - I_L\cdot\tilde{d}(s) \tag{4-37}$$

Putting equation (4-34), equation (4-35), and equation (4-36) in matrix form:

$$\begin{bmatrix} s\cdot L & 1-D \\ 1-D & -(s\cdot C + \frac{1}{R}) \end{bmatrix}\cdot\begin{bmatrix}\tilde{i}_L(s)\\ \tilde{v}_O(s)\end{bmatrix} = \begin{bmatrix}V_O\\ I_L\end{bmatrix}\cdot\tilde{d}(s) + \begin{bmatrix}1\\0\end{bmatrix}\cdot\tilde{v}_{in}(s) \tag{4-38}$$

$$\begin{bmatrix}\tilde{i}_L(s)\\ \tilde{v}_O(s)\end{bmatrix} = \begin{bmatrix} s\cdot L & 1-D \\ 1-D & -(s\cdot C + \frac{1}{R}) \end{bmatrix}^{-1}\cdot\begin{bmatrix}V_O\\ I_L\end{bmatrix}\cdot\tilde{d}(s) + \begin{bmatrix} s\cdot L & 1-D \\ 1-D & -(s\cdot C + \frac{1}{R}) \end{bmatrix}^{-1}\cdot\begin{bmatrix}1\\0\end{bmatrix}\cdot\tilde{v}_{in}(s) \tag{4-39}$$

Finally inverse matrix can be calculated and the converter transfer functions can be obtained by simply solving matrix (4-39). Control to output transfer function is [30], [32]:

$$\frac{\tilde{v}_O(s)}{\tilde{d}(s)} = \frac{(1-D)\cdot V_O - (L\cdot I_L)\cdot s}{(L\cdot C)\cdot s^2 + \frac{L}{R}\cdot s + (1-D)^2} \tag{4-40}$$

Control to input current transfer function is:

$$\frac{\tilde{i}_L(s)}{\tilde{d}(s)} = \frac{(C \cdot V_O) \cdot s + 2 \cdot (1-D) \cdot I_L}{(L \cdot C) \cdot s^2 + \frac{L}{R} \cdot s + (1-D)^2} \tag{4-41}$$

Current to output transfer function is:

$$\frac{\tilde{v}_O(s)}{\tilde{i}_L(s)} = \frac{(1-D) \cdot V_O - (L \cdot I_L) \cdot s}{(C \cdot V_O) \cdot s + 2 \cdot (1-D) \cdot I_L} \tag{4-42}$$

4.4.1 PI controller

Cascade compensation is a common method of compensation in which the proportional-integral (PI) controller is placed in series with the plant. PI compensator feeds the error (proportional) plus the integral of the error forward to the plant. Since it can ensure zero steady-state error when tracking DC quantities, it is usually used in DC/DC converters [3]. The block representation of this cascade PI compensation is shown in Figure 4-6.

The compensator transfer function is given as [3]:

$$G_c(s) = K_P + \frac{K_i}{s} = \frac{K_P \cdot s + K_i}{s} = \frac{K_i / K_P + s}{s} \cdot K_P \tag{4-43}$$

The PI controller places an open-loop pole at the origin, equation (4-43), which places a zero, $z = -\frac{K_i}{K_P}$, on the negative real axis, but close to the integrator's pole at the origin. Therefore, the two cancels out. The result is a fixed steady-state error without affecting the transient response. With only an integrator as the controller, the response will be slowed down which results in higher rise time.

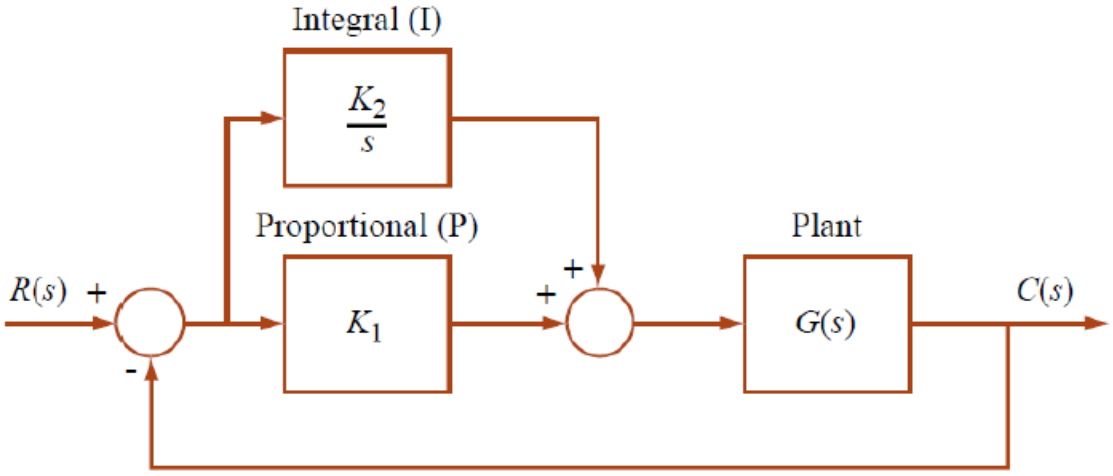

Figure 4-6: block representation of cascade PI compensation [3]

4.4.2 Control requirements

The DC/DC converter feedback controllers enable us to control the inductor current, i_L, flowing to and from the ultra-capacitor as well as the DC bus voltage. For current regulation in the feedback control system, the inductor current, i_L, is measured and compared with a reference value, $i_{L,ref}$. The difference between the two acts on the PI controller which produces the control voltage, $v_c(t)$. The control voltage is the input of the PWM block which produces a switching signal, $q(t)$. The switching signal is sent to the control gate of the IGBT transistors. The average value of this signal is the duty ratio D. The same procedure transpires for the voltage controller. The new open-loop transfer function becomes:

$$G_{OL}(s) = G_P(s) \cdot G_C(s) \tag{4-44}$$

Where $G_C(s)$ is the transfer function of the PI controller, $G_P(s)$ is the plant transfer function. The PWM block gain is assumed as unity, hence, does not appear in equation (4-44).

To simplify the modeling and simulations of the converter with the feedback controllers, the dynamic average representation, described in section 4.5, is implemented. The feedback controller system must be designed with the succeeding characteristics of a linear system:

1. Zero steady state error;

2. Fast response to changes in the input and output;

3. Low overshoot;

4. Low noise susceptibility;

For a given $G_P(s)$, the task is to properly tailor $G_C(s)$ so that $G_{OL}(s)$ satisfies the performance requirements listed above. In the feedback control analysis the main characteristics of the open-loop transfer function are:

1. The gain at low frequencies should be high to minimize the steady-state error, e_{SS}, in the output.

2. The cross-over frequency is the frequency at which the gain of $G_{OL}(s)$ becomes unity ($0dB$). This cross-over frequency, w_C, should be as large as possible, since the rise time, T_r, of the closed loop response is almost equal to $T_r \approx \frac{1}{w_C}$. However, it should be about an order of magnitude below the switching frequency, f_S, letting the load to respond fast to the transients, such as rapid changes of load. The cross-over frequency determines the speed of the PI controller response to various disturbances. The higher the cross-over frequency, the shorter is the rise time and the settling time, hence, the system stabilizes faster.

3. The phase margin is defined as: $PM = \phi_{OL} + 180^{\circ}$, where ϕ_{OL} is the phase angle of $G_{OL}(s)$ at the cross-over frequency. Phase margin, which should be a positive value, determines the transient response of the output to abrupt changes in the load. To have a stable system, the phase margin must be less than 180°.

When all is said, we will see when designing the controllers in section 4.4.3 that some of the above goals should be compromised in our system. The main reason is that despite linearizing the converter via average modeling, it still shows some nonlinear behaviour. The details will be discussed later in this chapter.

Table 4-3: The parameters of the system

V_{in}	30 Volts
V_O	180 Volts
f_S	10 kHz
$P_{O,nominal}$	1 kW
R	32.4 ohms
L	3 mH
C	300 μF

4.4.3 Ultra-capacitor converter controllers design

The PI controllers are designed here to satisfy the above mentioned requirements. The parameters of the system are as found in Table 4-3. The configuration of the current loop and the voltage loop is shown in Figure 4-7. The inner loop is chosen to be the current loop. The reference of the current loop is produced by the outer voltage loop. The voltage loop generates a current reference to maintain 180 Volts on the DC bus [32], [33].

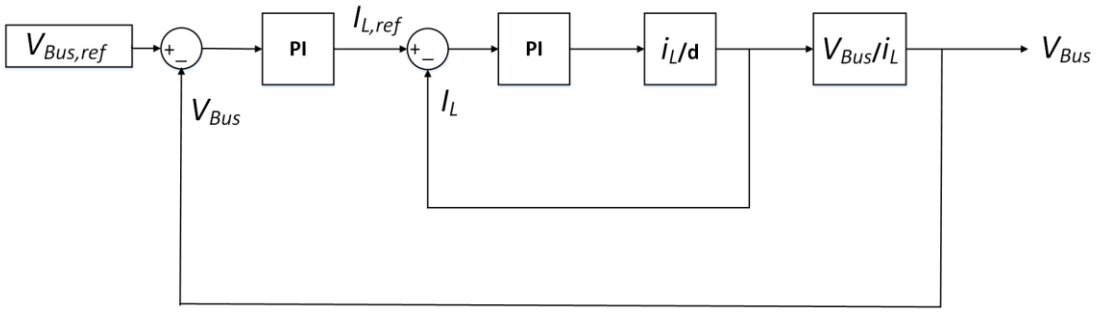

Figure 4-7: Block Diagram of the current and voltage control loops

4.4.3.1 Inner current loop controller design

First the inner current loop controller is designed. The inner current loop operates much faster than the outer voltage loop. The current controller can be designed assuming the outer loop has no effect on the operation of inner loop. The control to input current transfer function is as follows:

$$\frac{\widetilde{i}_L(s)}{\widetilde{d}(s)} = \frac{0.054 \cdot s + 11.22}{(9 \cdot 10^{-7}) \cdot s^2 + (9.259 \cdot 10^{-5}) \cdot s + 0.0289}$$

For controller design SISO tool in Matlab/Simulink is used. Bode plot and step response of the control to input current transfer function are shown in Figure 4-8 and Figure 4-9.

The step response shows that the system is not stable. The input step has a magnitude of one i.e. the system response should eventually converge to one. However, the response reaches 388 after 0.14 seconds which means that it is not able to track the input reference.

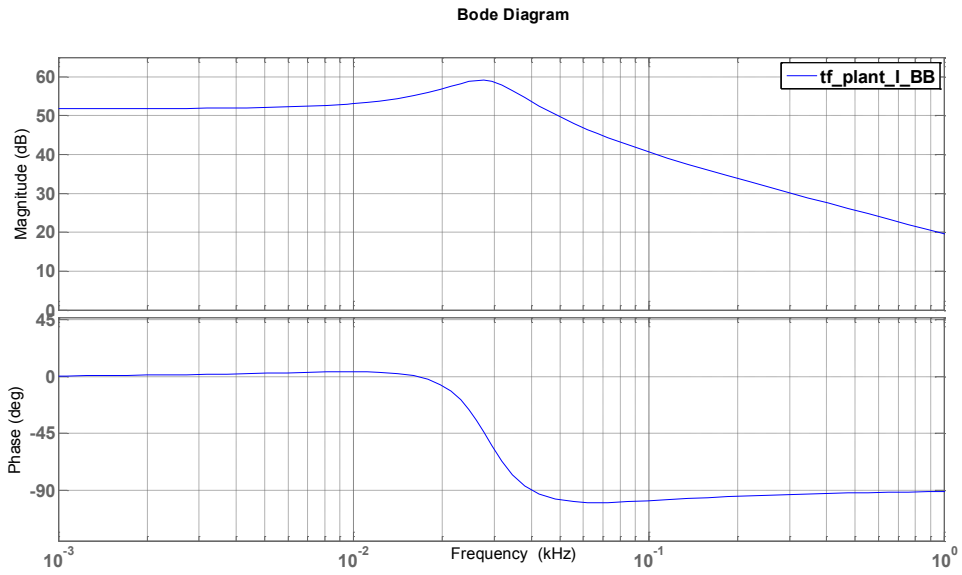

Figure 4-8: Bode diagram of control to input current transfer function / ultra-capacitor converter

After some testing, the following parameters were found to produce the desired response.

$$K_P = 0.1145$$
$$K_I = 15.475$$

The bode-plot of the open-loop system which is the control to input current transfer function in series with the controllers can be seen in Figure 4-10.

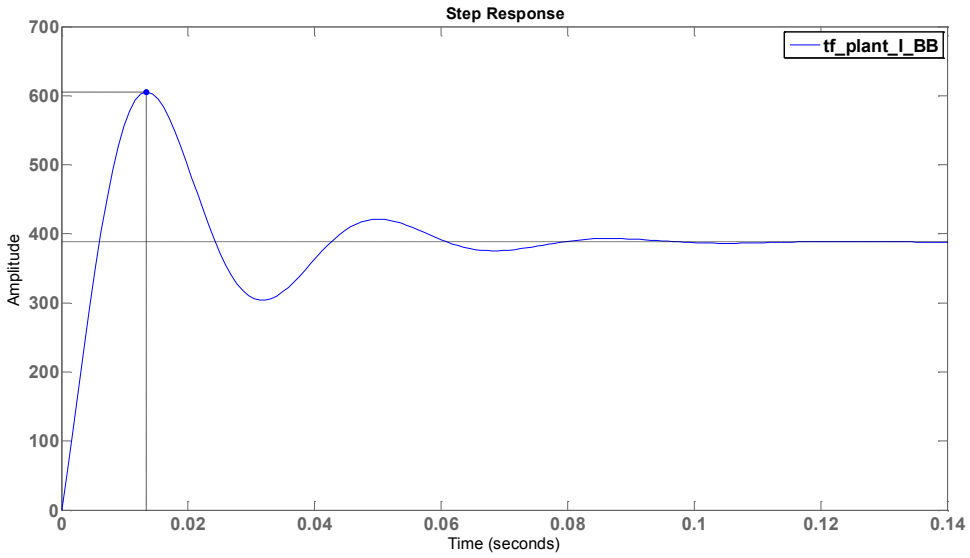

Figure 4-9: Step Response of control to input current transfer function / ultra-capacitor converter

The open-loop frequency response results in a phase margin of $PM = 88^{\circ}$ and a cross-over frequency $w_C = 6880\ rad/s \approx 1095\ Hz$. Hence, the switching frequency, f_S , is approximately 10 times higher than f_C , which is in accordance with the predefined requirements. Looking at the new step response of the closed-loop system gives the result shown in Figure 4-11.

The rise time is $T_r = 0.000292\ s$ and the settling time is $T_S = 0.00177\ s$. The overshoot is 2.63 percent which is within the reasonable range of five percent. Thus, placing the PI controller in cascade with the plant has effectively eliminated the steady state error and gives a satisfying transient response.

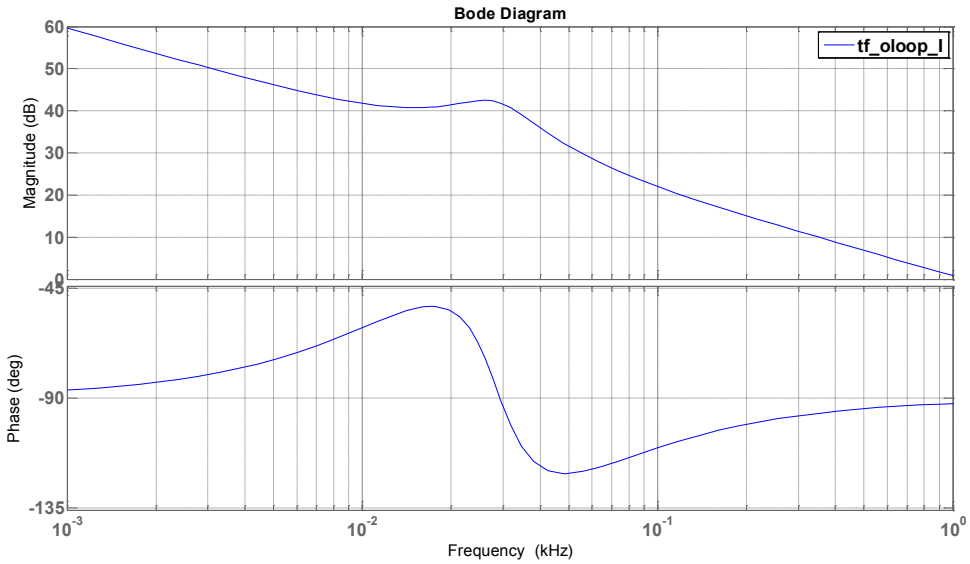

Figure 4-10: Bode plot the new open-loop transfer function of the current loop/ ultra-capacitor converter

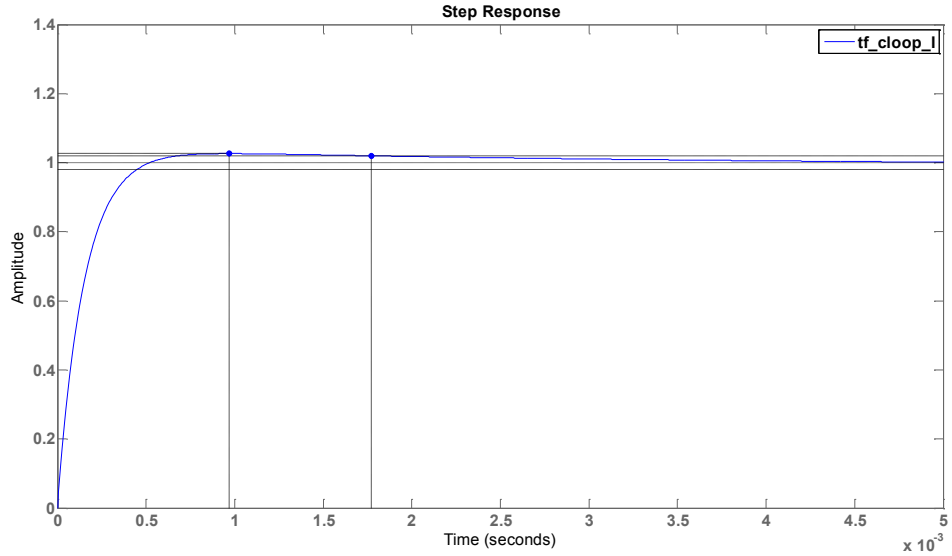

Figure 4-11: Closed-loop step response of the current loop/ ultra-capacitor converter with controller

4.4.3.2 Outer voltage loop controller design

The current to output transfer function is as follows:

$$\frac{\tilde{v}_O(s)}{\tilde{i}_L(s)} = \frac{(1-D)\cdot V_O - (L\cdot I_L)\cdot s}{(C\cdot V_O)\cdot s + 2\cdot(1-D)\cdot I_L} = \frac{30.6 - 0.099\cdot s}{0.054\cdot s + 11.22}$$

According to Figure 4-7 the open-loop transfer function in this case consists of inner current closed-loop including the current controller in series with the current to output transfer function. The transfer function is as follows.

$$G_V(s) = \frac{(-61.21\cdot 10^{-5})\cdot s^3 - 0.02071\cdot s^2 + 47.69\cdot s + (5.313\cdot 10^3)}{(4.86\cdot 10^{-8})\cdot s^4 + (34.9\cdot 10^{-5})\cdot s^3 + (0.1865)\cdot s^2 + 33.49\cdot s + 1948}$$

After observing the bode plot and step response of the open-loop system, outer voltage loop controller is designed. Preferably, the response speed of the inner loop should be at least ten times faster than the outer loop. Rise time has an almost inverse relation with cross-over frequency. Hence, for a damped system the maximum cross-over frequency of the outer loop should be chosen one tenth of the inner loop. After some testing, the following PID controller was found to be the best choice.

The proportional gain, K_P, is 0.1717; the integral gain, K_I, is 97.863, the derivative gain, K_D, is -0.001, and the filter coefficient, N, is 0.0092. The filter coefficient sets the location of the pole in the derivative filter.

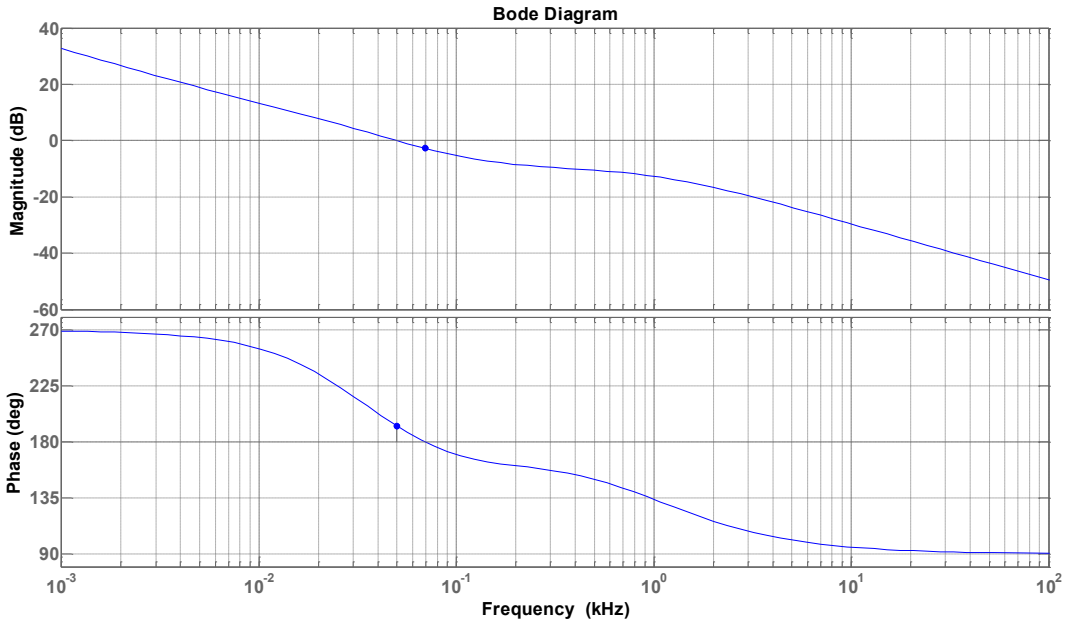

Figure 4-12: Bode plot the open-loop transfer function of the voltage loop/ ultra-capacitor converter

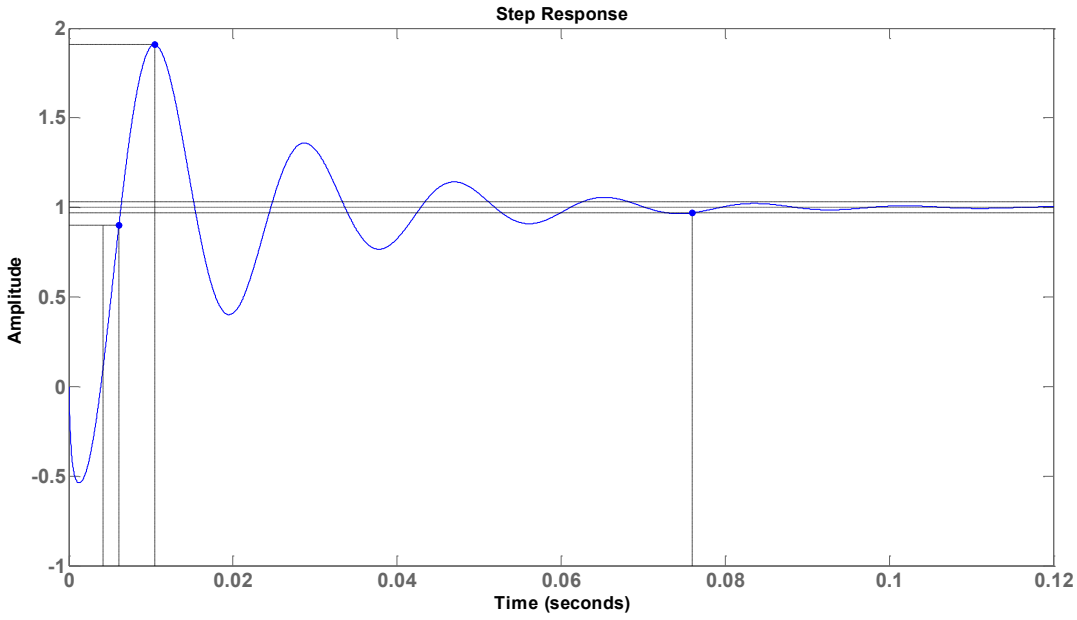

Figure 4-13: Closed-loop step response of the voltage loop/ ultra-capacitor converter with controller

Bode plot of the voltage open-loop transfer function with the controller and step

response of the closed-loop are shown in Figure 4-12 and Figure 4-13.

The step response goes negative first, then goes positive, ending with zero steady-state error. This is normal, when your transfer function contains positives zeros which makes the system a non-minimum phase system [RW.ERROR - Unable to parse: {{41 {{41MichaelAJohnson,MohammadH.Moradi2005}}] [34]. This phenomenon does not affect the system operation in simulation.

In the open-loop bode plot, the cross-over frequency and phase margin are two important values that must be examined for evaluating the performance of a closed voltage regulation loop [35], [36], [19]. Simulation results show that in case of this nonlinear plant, i.e., DC/DC converter, the controllers with low cross-over frequency will:

a. make the system very sensitive to proximity with respect to the operating point ;
b. result in large over-shoot when applied to the nonlinear system which is attributed to their slow transient response;

and therefore do not show desirable results. In conclusion, what we need is a controller with a small rise time which results in higher cross-over frequency. The designed PI controller gives a cross-over frequency of $f_C = 50\ Hz$ and a

phase margin of $PM = 13°$. The cross-over frequency is about 20 times smaller than the current loop controller cross-over frequency. This makes the inner loop about 20 times faster than the outer loop which is in compliance with the condition mentioned earlier. The phase margin is smaller than $180°$, but it is relatively small. On the other hand, the overshoot in closed loop step response is 91 percent which is way out of the range of five percent. The high overshoot as well as the small phase margin is a trade-off for the low rise time. The rise time is $T_r = 0.00195\ s$ and the settling time is $T_S = 0.076\ s$ which are adequately small.

Simulation results show that a controller that has a larger value of cross-over frequency results in lower overshoot when applied to system. The controller will be implemented in the whole system; the results will be presented in chapter 6. It will be validated in simulation that placing the PI controller in cascade with the plant has effectively eliminated the steady state error and gives a satisfying transient response.

4.5 DC Rail Boost Converter

4.5.1 Introduction

A boost converter as shown in Figure 4-5 is interfaced with a DC source that represents the DC rail in the metro system. This converter regulates the DC bus

voltage or controls the current flowing from the source to the DC bus with respect to the control algorithm employed. In other words, it controls the power transfer from the DC rail which is the MES to the rest of the system, i.e., ultra-capacitor bank and the motor drive.

4.5.2 Components design of the boost converter

The principals of the operation of a boost converter are already explained in this chapter hence are not discussed here. The parameters of the converter are shown in Table 4-4.

Table 4-4: Predifined conditions of the DC rail boost converter

V_{in}	120 Volts
V_o	180 Volts
f_S	10 kHz
$P_{O,nominal}$	540 W
Range of P_O	(50 to 100 %)$P_{O,nominal}$
Output ripple($\Delta V_O/V_O$)	5 %

No output filter is used for this converter, hence its output current is a pulse train current. The load connected to this converter and the DC bus is a motor drive. The inductor used in the motor drive converter, along with the DC bus capacitor, is capable of smoothening the motor drive input current. The system works satisfactorily in simulations without the boost converter output filter.

An inductor value of $L = 3\ mH$ is chosen which gives a reasonable current ripple

of $\Delta i_L = 0.87\ amps$ calculated from equation (4-14) below:

$$\Delta i_L = \frac{V_{in,\max} \cdot D_{\max}(1 - D_{\max})}{L_S \cdot f_S} = \frac{120V \cdot 0.33(0.66)}{3(mH) \cdot 10(kHz)} = 0.87\ (amps) \qquad (4\text{-}45)$$

The output voltage ripple is taken care of with the DC bus filter capacitor. The voltage ripple is calculated below from equation (4-17).

$$\frac{\Delta V_O}{V_O} = \frac{T_S^2(1-D)}{8LC} = \frac{0.66}{8 \cdot 3mH \cdot 0.3mF \cdot (10kHz)^2} = 0.09\% \qquad (4\text{-}46)$$

The ripple is below five percent which meets the design goal.

4.5.3 DC rail boost converter controller design

To have more control flexibility separate PI controllers are designed for current and voltage control. An inner current controller loop and an outer voltage controller loop will be designed based on the theory explained in section 4.5.

In the case of this thesis, the output power of the boost converter varies from 50% to 100 % of the nominal load power. Hence, an output power of 66 percent of nominal power, $P_O = 360\ W$, is considered in the controller design. The system works for the longest relative period with the selected output power. The selected power gives a resistive load value of $R = 90\ ohms$.

4.5.3.1 Inner current loop controller design

Transfer function of control to input current from equation (4-41) is as follows:

$$\frac{\tilde{i}_L(s)}{\tilde{d}(s)} = \frac{0.054 \cdot s + 4.02}{(9 \cdot 10^{-7}) \cdot s^2 + (3.333 \cdot 10^{-5}) \cdot s + 0.4489}$$

Bode plot and step response of the control to input current transfer function are shown in Figure 4-14 and Figure 4-15 respectively. The step response shows that the system is not stable. The input step has a magnitude of one i.e. the system response should eventually converge to one. However, the response reaches 8.96 after 0.3 seconds which means that it is not able to track the input reference. Now the steady state error can be removed by cascade PI compensation. This will be seen later when studying the error of the new closed-loop system with the PI controller. After some testing, the following parameters were found to produce the desired response:

$$K_P = 0.0138$$
$$K_I = 25.7558$$

The bode plot of the open-loop response with these parameters can be seen in Figure 4-16. The open-loop frequency response results in a phase margin of $PM = 60°$ and a cross-over frequency $f_C = 526\ Hz$. Hence, the switching frequency, f_S, is approximately 20 times higher than f_C, which is in accordance with the predefined requirements. Looking at the new step response of the closed-loop system gives the result shown in Figure 4-17.

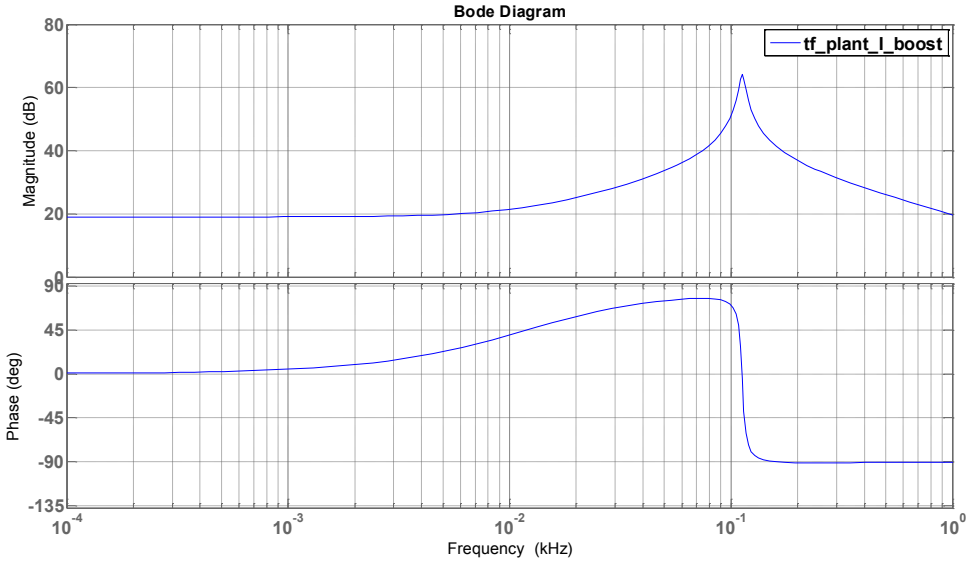

Figure 4-14: Bode diagram of control to input current transfer function / DC rail converter

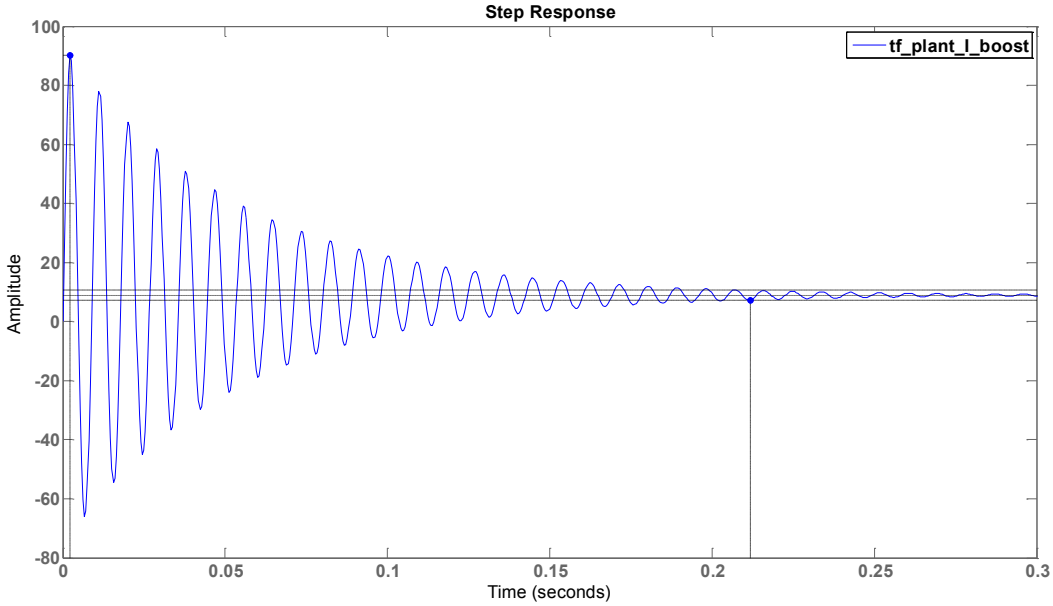

Figure 4-15: Step response of control to input current transfer function / DC rail converter

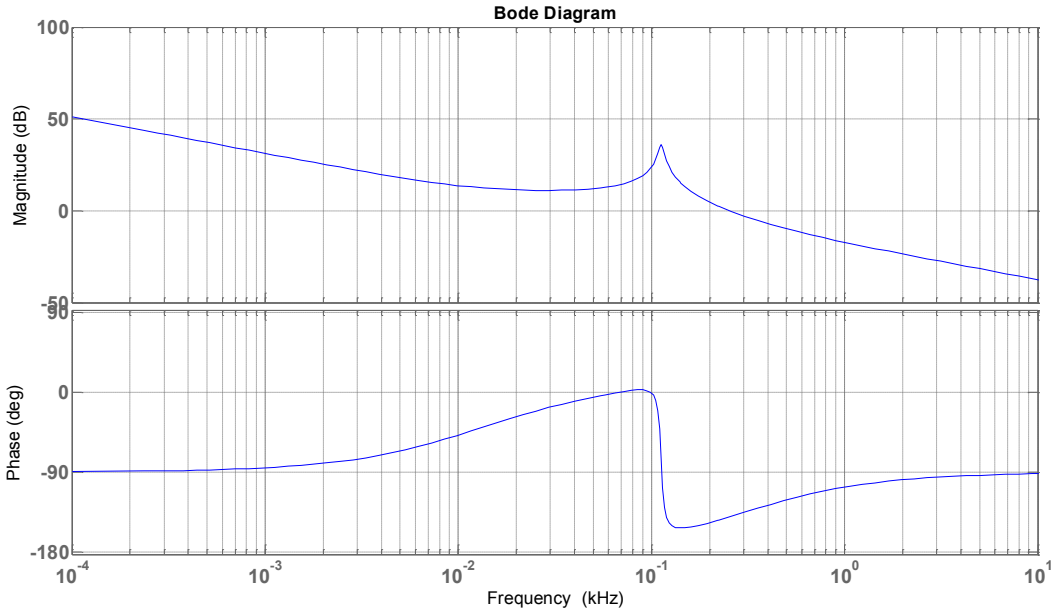

Figure 4-16: Bode plot the new open-loop transfer function of the current loop/ DC Rail converter

The rise time is $T_r = 0.000453\ s$ and the settling time is $T_S = 0.0451\ s$. The overshoot is 7.44 percent which is reasonable. Thus, placing the PI controller in cascade with the plant, has effectively eliminated the steady state error and gives a satisfying transient response.

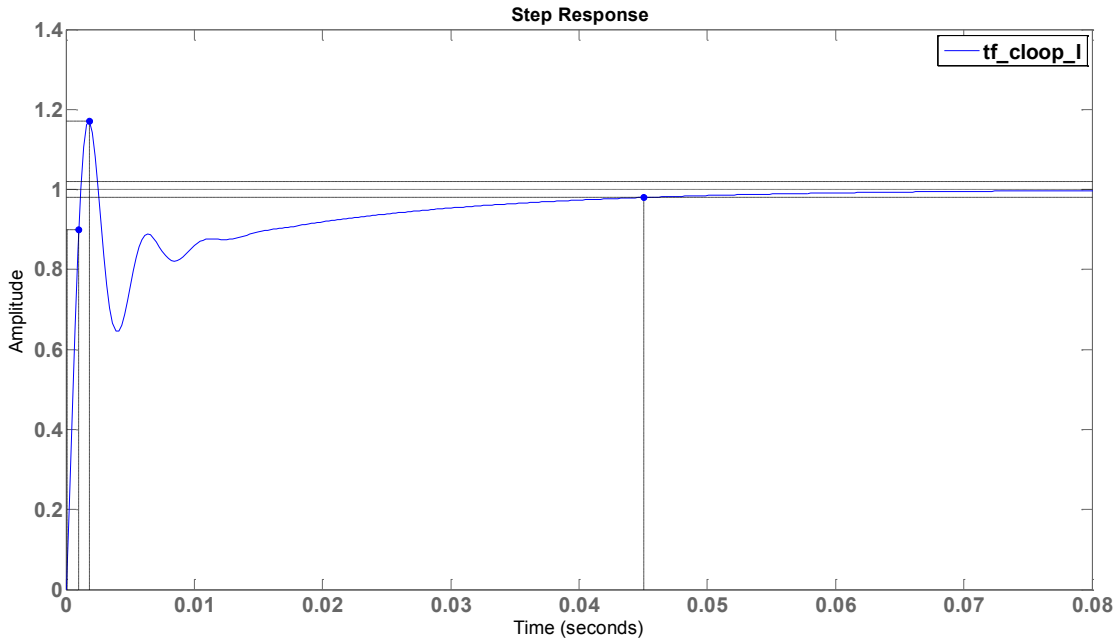

Figure 4-17: Closed-loop step response of the current loop/ DC rail converter with controller

4.5.3.2 Outer voltage loop controller design

The current to output transfer function from equation (4-42) is as follows:

$$\frac{\tilde{v}_O(s)}{\tilde{i}_L(s)} = \frac{120.6 - 0.009 \cdot s}{0.054 \cdot s + 4.02}$$

According to Figure 4-7 the open-loop transfer function in this case consists of inner current closed loop including the current controller in series with the current to output transfer function. The transfer function is as follows:

$$G_V(s) = \frac{(-6.707 \cdot 10^{-6}) \cdot s^3 + 0.07685 \cdot s^2 + 173.5 \cdot s + (1.249 \cdot 10^4)}{(4.86 \cdot 10^{-8}) \cdot s^4 + (4.566 \cdot 10^{-5}) \cdot s^3 + (0.1055) \cdot s^2 + 13.21 \cdot s + 416.2}$$

After plotting the bode plot and step response of the open-loop system, a PI controller with $K_P = 0.49$ and $K_I = 100$ is designed as the outer voltage loop

controller. Bode plot of the voltage open-loop transfer function in series with the designed controller and step response of the closed loop are shown in Figure 4-18 and Figure 4-19.

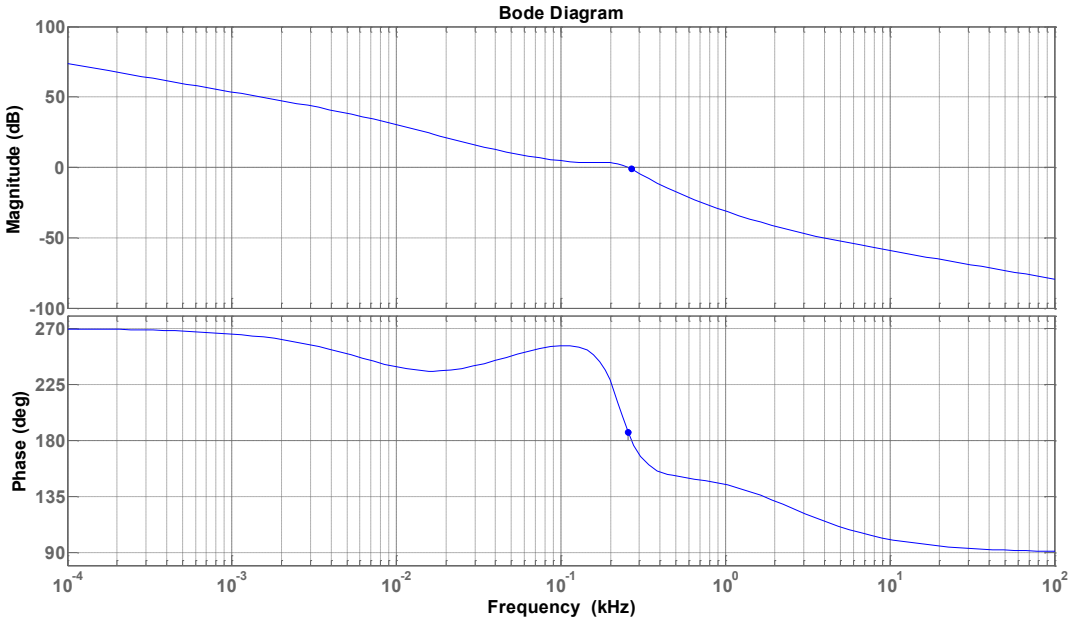

Figure 4-18: Bode plot the open-loop transfer function of the voltage loop/ DC rail converter

The cross-over frequency of the voltage loop controller is $f_C = 256\ Hz$ which is about half of the current loop controller cross-over frequency of $526\ Hz$.

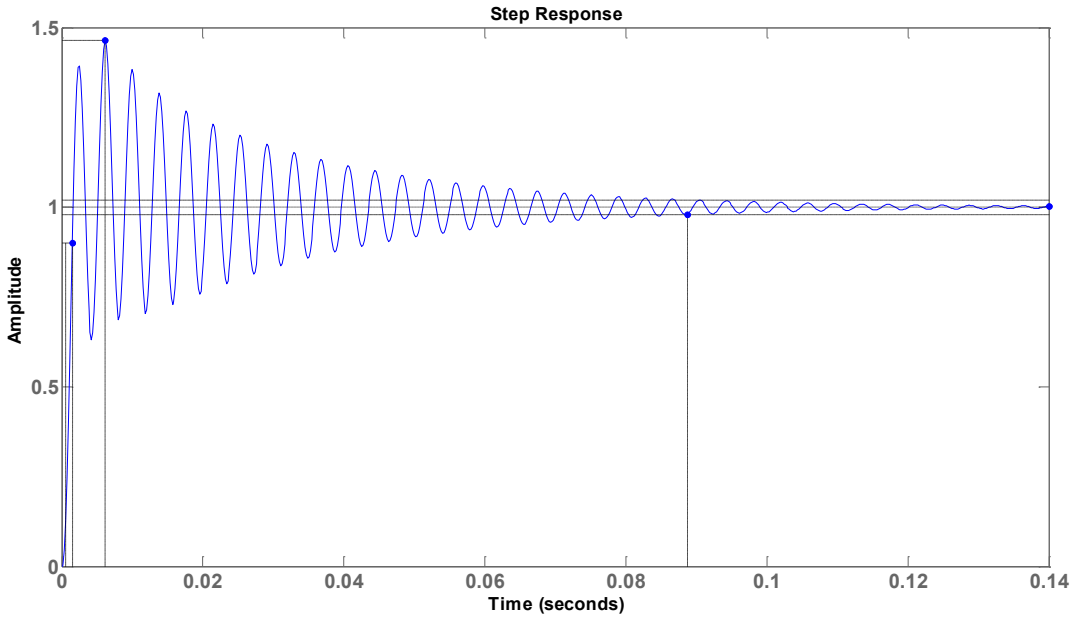

Figure 4-19: Closed-loop step response of the voltage loop/ DC rail converter with controller

The response of the inner loop is twice faster than the outer loop. Rise time has an almost inverse relation with cross-over frequency. Hence, for a damped system, the maximum cross-over frequency of the outer loop should be chosen as a tenth of the inner loop. Here the voltage loop cross-over frequency is chosen as half of the current loop to obtain the lowest possible voltage over shoot. The simulation results consolidate the theory expressed.

Similar to the voltage closed-loop step response and open-loop bode plot in section 4.5.3, a small phase margin of $PM = 6.5°$ in bode plot is obtained. The overshoot due to a step input is 46.4%. The high overshoot as well as the small phase margin is a trade-off for the low rise time. The rise time is $T_r = 0.000975\ s$

and the settling time is $T_S = 0.0887\ \ s$ which are adequately small.

4.6 **Summary**

In this chapter, the ultra-capacitor interfaced bidirectional DC/DC converter was designed. The control requirements for the application of this thesis were defined. The converter average model was presented and used to design and analyze PI controllers based on the control requirements of this application. In designing the controllers, the issue of the converter inherited nonlinearities was considered and effective solutions are employed. Then, the same steps are taken for the DC rail Boost converter and controller design. The PI controllers designed for both buck-boost and boost converters will be used in simulation in chapter 6.

Chapter 5: Baldor CDPWD3585 PMDC Machine Drive Design

5.1 Introduction

In this chapter the Baldor CDPW3585 PMDC machine, which is selected to represent the metro traction motor, is studied. Experimental tests are done to extract the 2 Hp machine parameters in the PEER laboratory at Concordia University. A bidirectional current drive is designed for the scaled down load power profile to allow the speed and current control in both acceleration and regenerative braking modes. The designed converter as the drive is a buck-boost converter. Speed regulation is done by use of cascaded PI controllers. The machine with its drive is simulated in Matlab/Simulink and the results are presented.

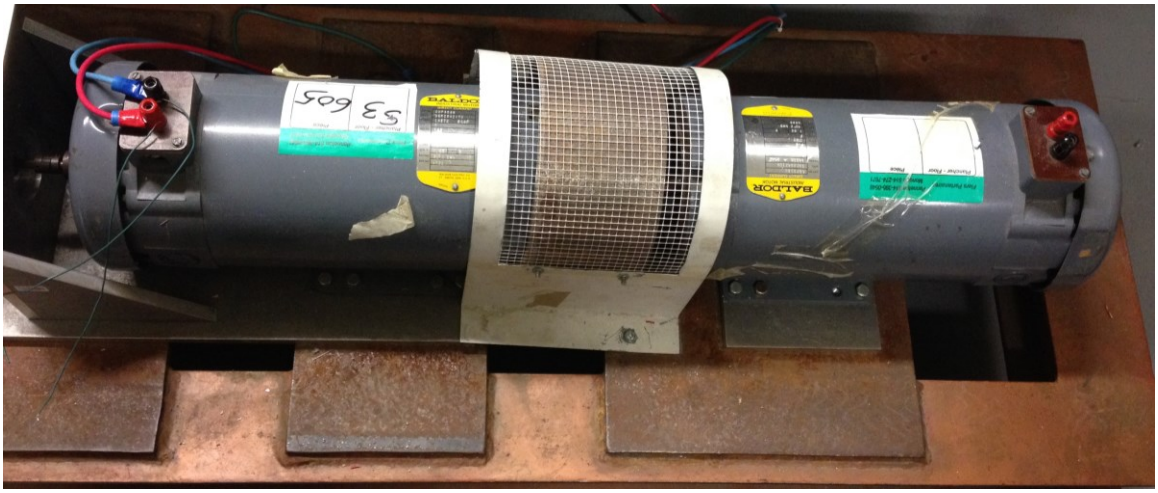

Figure 5-1: The tested Baldor CDPW3585 PMDC machine

5.2 Measuring the Machine Parameters

The motor model used in simulations requires parameters that are extracted using experimental tests. This allows the identification of the motor circuit parameters.

The following parameters were determined [37], [38], [39]:

- Armature Resistance, R_a
- Armature Inductance, L_a, and Armature Resistance from AC Test
- Back-EMF Constant, K_E
- Motor Torque Constant, K_T

The motor nameplate data is presented in Table 5-1.

Table 5-1: Motor Nameplate data

Model	Baldor CDPWD3585
Power	2 Hp
Voltage	180 Volts
Current	8.5 amps
Frequency	60 Hz
Speed	1750 RPM

5.2.1 Measuring armature resistance, R_a

The armature resistance can be measured by utilizing the Ohm's law directly. The shaft is constrained, and then a DC voltage is applied to the armature terminals. The current through the armature is measured. The armature resistance is found by R = V/I, where V is the voltage across the terminals. The measured values at three different voltages are shown in Table 5-2.

Table 5-2: Resistance test results

Voltage, Volts	Current, amps	Resistance, ohms
5	1.9	2.63
8	3.7	2.16
10	4.9	2.04

The average resistance is therefore R= 2.27 ohms.

5.2.2 Armature inductance L_a, and armature resistance measurement from AC test

The armature is connected to a 60 Hz AC voltage source at standstill. The voltage

(V_{ac}) and the current (I_{ac}) at the armature terminals are measured by use of an oscilloscope phasor-analyzer which is used to determine the angle, θ, between the current and the voltage.

$$X_a = \frac{V_{ac}}{I_{ac}} \sin\theta \tag{5-1}$$

The inductance is then calculated as:

$$L_a = \frac{x_a}{2\pi f} \tag{5-2}$$

The results of the measurements are shown in Table 5-3.

Table 5-3: Inductance test results

V_{ac}, Volts	I_{ac}, amps	Power , W	Angle, θ°
12.23	1.8	14.44	49
12.53	2	15.77	51

The average value of L_a is then calculated from equation (5-1) and equation (5-2) which is 0.013 H.

5.2.3 Back-EMF constant, K_E

To measure the Back-EMF constant, the DC machine was rotated by a prime mover with its armature open circuited. The Back-EMF was measured at the armature terminals for the rated speed of 1750 rpm to 606 rpm, in a decreasing manner. The measurements are repeated at descending intervals of 100 rpm, i.e. 1650 rpm, 1550 rpm until the machine stalls (100 rpm). The data from

measurements are as shown in Table 5-4, while Figure 5-2 shows a plot of the back-EMF as a function of speed. The slope of this curve is the Back-EMF constant that satisfies the relation:

$$E_a = K_E \omega \tag{5-3}$$

$$K_E = \frac{E_a}{\omega} \tag{5-4}$$

Which can also be expressed as:

$$K_E = \frac{\Delta E_a}{\Delta \omega} \tag{5-5}$$

The measured K_E is 1 Volts.s/rad.

Table 5-4: Back-EMF Constant Measurement

$Ea\ Volts$	N RPM
65.4	606
73.4	682
81.7	758
89.7	834
98	912
106	984
114.4	1062
122.3	1136
130.7	1212
138.6	1286
147	1364
154.8	1438
163.3	1512
171.1	1588
179.5	1662
187.3	1734
195.8	1812

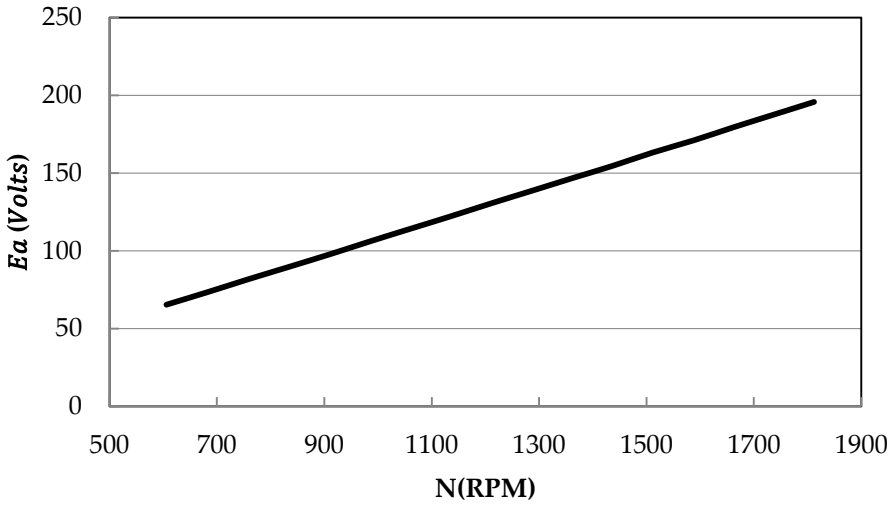

Figure 5-2: Back-EMF Constant Curve, Voltage verses Speed

5.2.4 Motor torque constant K_T

The motor torque constant (K_T) can be computed from the voltage constant(K_E).

From equating electrical power to mechanical power we have:

$$E \times I = T \times \omega \tag{5-6}$$

which can be rearanged as :

$$\frac{E}{\omega} = \frac{T}{I} \tag{5-7}$$

Where $K_T = \frac{T}{I}$ is the torque constant. It is determined as:

$$K_T \left[\frac{\text{N.m}}{\text{amps}}\right] = K_e \left[\frac{Volts}{\text{rpm}}\right] \times \frac{1}{9.554} \tag{5-8}$$

A summary of the PMDC machine parameters are shown in Table 5-5. The

Coulomb friction torque, viscous friction coefficient and inertia are taken from the datasheet.

Table 5-5: PMDC machine parameters

Back EMF constant, V/RPM	0.105
Total Inertia, kg.m^2	0.012
Viscous friction coefficient, B_m N.m.s	0.00001
Coulomb friction torque, T_f N.m	0
Armature Resistance , ohms	2.27
Armature Inductance, H	0.013
Rated Torque, N.m	8.15

In the next section a bidirectional current drive will be designed for the machine which is then used for speed regulation. The current and speed PI controllers are also designed.

5.3 **Motor Drive Converter and Controller Design**

The selected converter for the motor drive is a buck-boost converter which was fully analysed in chapter 4. The converter inductor was determined as 3 mH. For the control scheme, speed regulation is done since the motor should follow the train drive cycle. The outer speed loop produces the current reference, which is then used to generate the duty-ratio of the PWM generator blocks. The current reference value is calculated in such a way as to allow the machine to track the desired drive cycle speed.

The mathematical modeling of the PMDC motor with IGBT based chopper

converter and PI controllers is presented next.

5.3.1 PMDC Machine

The schematic diagram of the PMDC machine is shown in Figure 5-3.

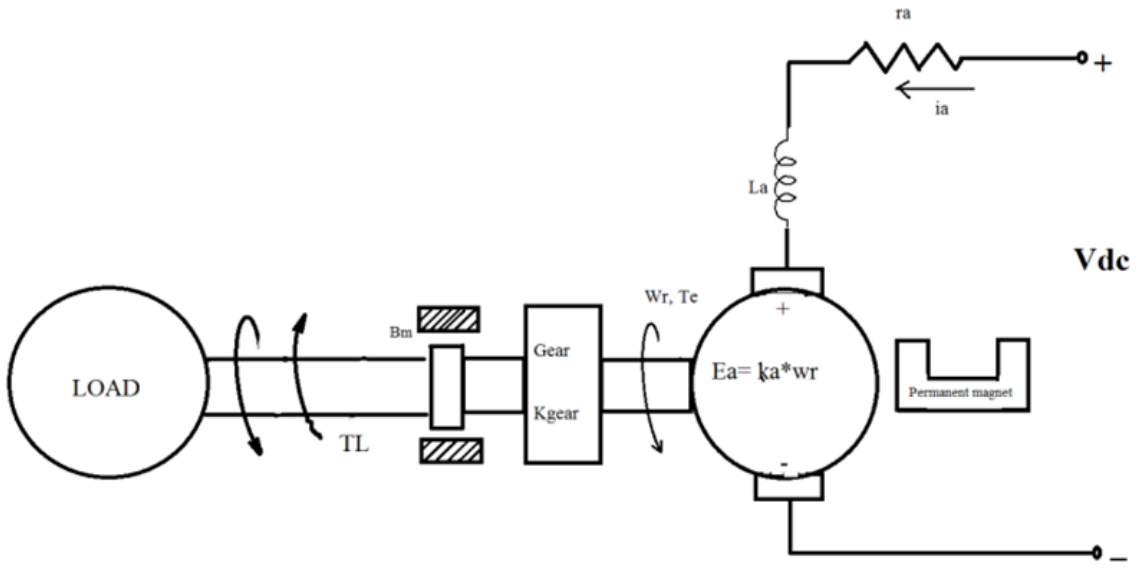

Figure 5-3: Schematic Diagram of DC machine [40]

To find the transfer function of the block diagram for the open-loop system, a differential equation to describe the system dynamics is used. Kirchhoff's voltage law is used to determine the armature voltage as [41], [40].

$$V_a = I_a\, r_a \; + L_a \frac{dI_a}{dt} + E_a \tag{5-9}$$

The Back-EMF, E_a is generated by the rotation of the armature conductors at speed ω_{em} in the presence of field flux, and is given by:

$$E_a = K_E \omega_{em} \tag{5-10}$$

The permanent magnets in PMDC machine produce a constant field electromagnetic torque, T_{em} is given by:

$$T_{em} = K_T I_a \tag{5-11}$$

Where, K_T is the torque constant of the motor.

The viscous friction torque is:

$$T_V = B_m \, \omega_{em} \tag{5-12}$$

The interaction of T_{em} (electromagnetic torque generated) with the load torque, T_L is given by:

$$T_{em} - T_V - T_L = J \ \frac{d\omega_{em}}{dt} \tag{5-13}$$

$$K_T I_a \ - T_V - T_L = J \ \frac{d\omega_{em}}{dt} \tag{5-14}$$

Taking Laplace transforms of equation (5-13) and equation (5-14), we get:

$$V(s) = I_a \ (s) \ r_a \ + s \ L_a I_a(s) + E_a(s)$$

$$I_a(s) = \frac{V(s) - E_a(s)}{r_a \ + s \ L_a}$$

$$\omega_{em}(s) = \frac{1}{s \ J_{eq}} (T_{em}(s) - T_V(s) - T_L)$$

The block diagram of the complete PMDC machine drive is shown in Figure 5-4.

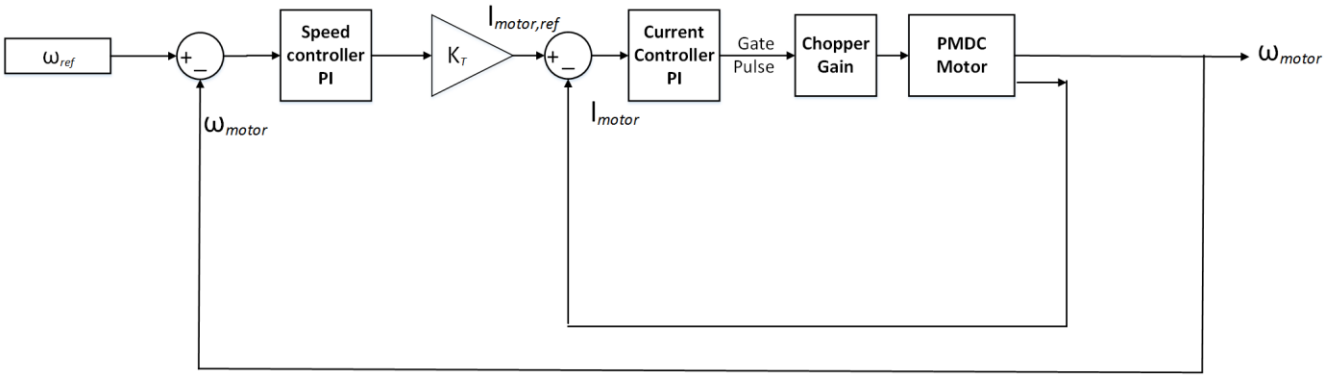

Figure 5-4: Block Diagram of a Complete Drive System [37]

5.3.2 PI controllers design

Cascade speed and torque controllers are employed for the motor. The outer speed loop outputs the armature current reference used by the current controller to obtain the electromagnetic torque needed to reach the desired speed. The armature current regulator is based on a second PI controller. The regulator controls the armature current by computing the appropriate duty ratios of the fixed frequency pulses of the two IGBT devices (Pulse Width Modulation). This generates the average armature voltage needed to obtain the desired armature current and thus the desired electromagnetic torque. For proper system behavior, the two IGBT devices have opposite instantaneous pulse values.

The inputs to the current controller are current reference and the armature current flowing through the motor as inputs. The current reference is provided

by the speed controller during speed regulation. Similar to cascade controllers designed in chapters 4 and 5, the inner loop should be a couple of times faster than the outer loop.

The buck-boost converter is represented as the chopper block in Figure 5-4. The average value of the converter is used for controller design. The average current and voltage values are calculated from boost converter equations as described in chapter 4.

The PMDC transfer function, which is the plant is expresses as:

$$G_I(s) = K_{PWM} \frac{1/r_a}{1 + s\,\tau_e} \tag{5-15}$$

Where $\tau_e = \frac{L_a}{r_a}$ and K_{PWM} is the average converter gain. Following the steps stated in section 4.4.3, the succeeding values of proportional and integral gains are obtained as:

$$K_P = 1$$
$$K_I = 102$$

The speed to output torque transfer function is derived assuming the viscous and load toques are equal to zero.

$$\frac{\omega_{em}(s)}{T_{em}(s)} = \frac{1}{s\,J_{eq}} \tag{5-16}$$

The following PI controller gains are designed for the speed loop:

$$K_P = 0.8$$
$$K_I = 0.98$$

The simulation results of the motor drive are shown in Figure 5-5.

In Figure 5-5, the reference speed is the purple line and the resultant motor speed is the blue line. The motor speed is following the reference perfectly.

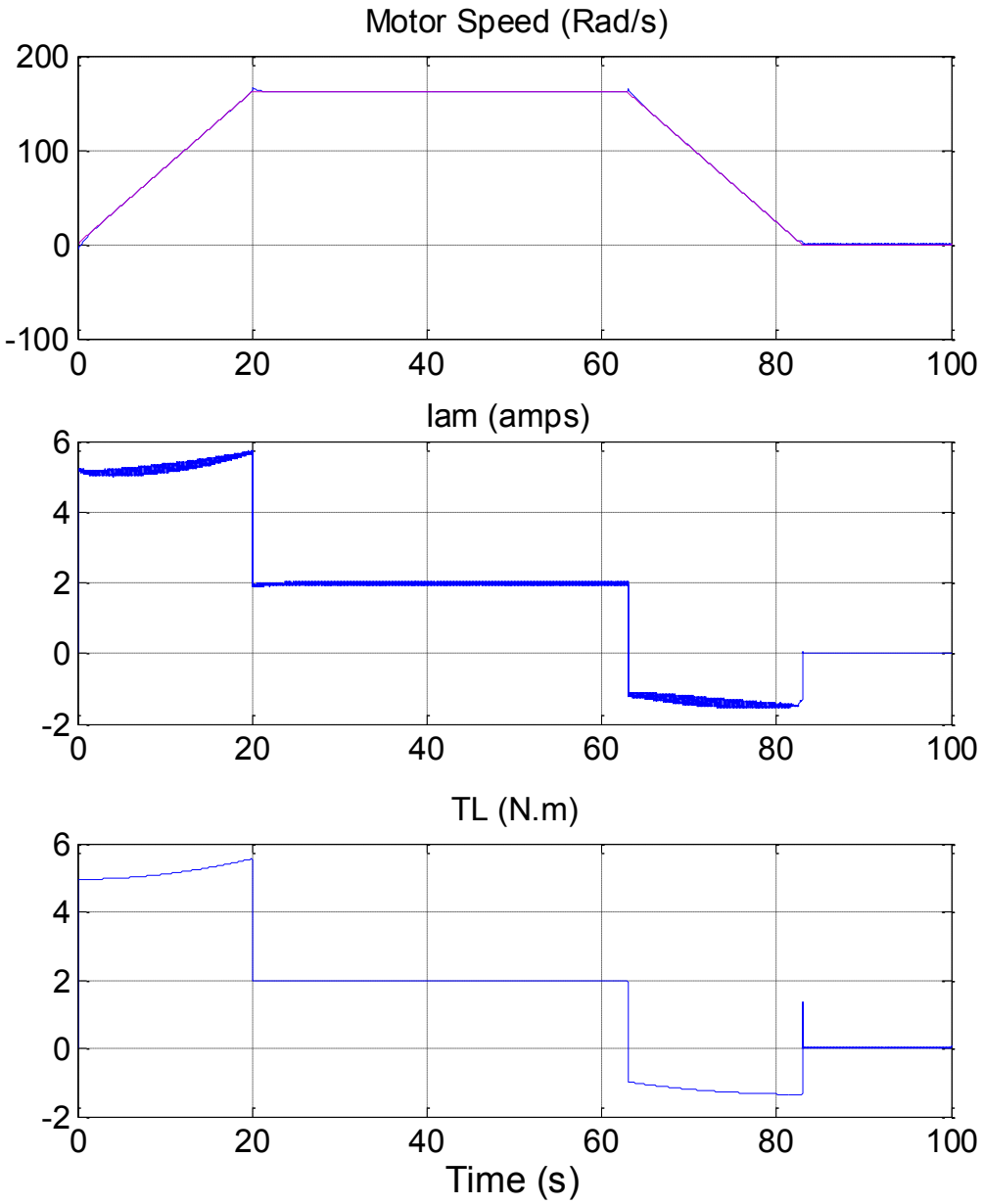

Figure 5-5: Machine speed, armature current and the input load torque

5.4 **Summary**

In this chapter the parameters of a 2 Hp Baldor CDPW3585 PMDC machine were

experimentally determined. The parameters were used to model the machine and perform speed regulation in Matlab/Simulink environment. PI controllers were designed to meet the time domain requirements of the machine's controlled drive.

Chapter 6: Control Strategy and Simulation Results

6.1 Introduction

The supervisory control strategy is developed in this chapter. The method used in [3] is adopted then modified for this application. Compared to methodologies used in the literature, the control scheme developed here enables simpler dynamics, superior regulation capability and ease of control.

The complete system that will be simulated consists of the following:

I. Controlled bidirectional current PMDC motor drive developed in chapter 5;
II. Buck-boost converter interfaced with the ultra-capacitor bank developed in chapter 4;
III. Boost converter interfaced with the DC rail developed in chapter 4;

All the three components above are simulated with the designed PI controllers. The control strategy is proposed and simulated in two phases based on two possible ultra-capacitor bank sizes for the Montreal metro system discussed in chapter 3. In the first phase, the method used in [3] is adopted then modified for

this application. The control strategy works well with ultra-capacitor bank sized to provide the acceleration energy. However, it does not work for the ultra-capacitor bank sized to provide the peak acceleration energy which has a smaller capacity compared to the first ultra-capacitor bank. To this end, a second control strategy is established in the next phase in which the control functionality of the converters are changed in a way to produce the desired results.

6.2 **Moving Average**

Moving average is an active peak power smoothing control strategy that could eliminate fast transients in DC source current and voltage. If P_{Load} is the instantaneous power required by the load, then the moving averaged power, P_m, is defined as:

$$P_m = \frac{1}{T_m}\int_0^{T_m} P_{Load}dt \qquad (6\text{-}1)$$

where T_m is the moving time window, which should be defined agreeing to the frequency of the applied load. P_m represents the desired power profile of the DC source. The current reference is determined by the following method: First, the calculated moving average power, P_m, is subtracted from the actual load power, P_{Load}, which defines the amount of power left, that should be covered by the

ultra-capacitor bank.

$$P_{UC,ref} = P_{Load} - P_m \tag{6-2}$$

Second, the $P_{UC,ref}$ is divided by the measured instantaneous ultra-capacitor bank voltage V_{UC} to produce the current reference going to the current controller as:

$$I_{UC,ref} = \frac{P_{UC,ref}}{V_{UC}} \tag{6-3}$$

$I_{UC,ref}$ is then sent to the controller where the measured inductor current I_L is subtracted from it, producing an error signal. The error is sent to the PI controller [3]. The expressed current reference generator in Matlab/Simulink can be seen in Figure 6-1.

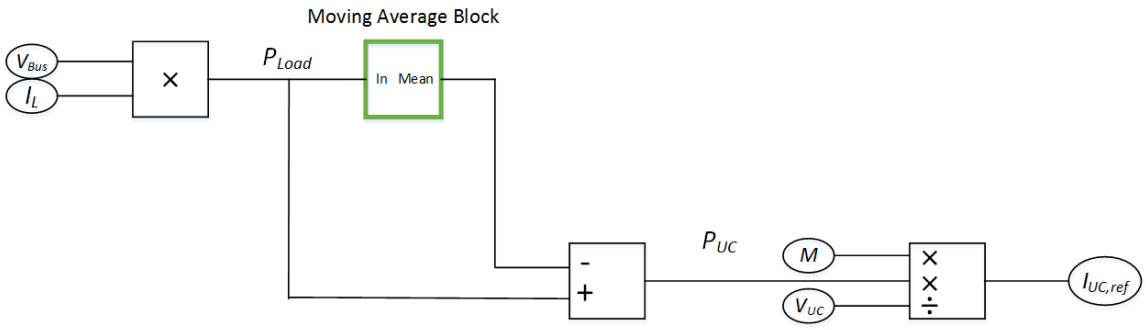

Figure 6-1: Moving Average Block in Matlab/Simulink [3]

6.3 Over and Under-Voltage Protection

The voltage variation of the ultra-capacitor bank should be kept between 50% and 100% of its maximum voltage. If the state of charge of the ultra-capacitor bank is close to 100 %, it could lead to its terminal voltage rise above the rated

voltage. This may eventually damage the ultra-capacitor bank. Therefore, there is a need to protect the ultra-capacitor bank from exceeding the rated voltage. An under-voltage protection at around half the rated voltage is also necessary since continuous discharging below this boundary could degrade the ultra-capacitor performance over time.

One way to implement a control strategy for voltage protection in the Matlab/Simulink model, is to formalize a logic block which takes the state of charge of the ultra-capacitor bank, SoC_{UC}, and the load current, I_{Load},as inputs, and generates a dimensionless value, M, ranging between zero and unity, based on a set of rules. M can then be multiplied with the ultra-capacitor bank current reference, $I_{uc,ref}$, which leads the ultra-capacitor bank into different modes of operation depending on its state of charge and the type of present loading [3]. The modified current reference is then:

$$I'_{uc,ref} = M \cdot I_{uc,ref} \tag{6-4}$$

The set of rules could be formulated according to equation (6-4) which is based on six operation regions.

$$M = \begin{cases} 0 & if \quad I_{Load} < 0 \quad SoC_{UC} \geq 100\% \\ 1 & if \quad I_{Load} > 0 \quad SoC_{UC} \geq 100\% \\ (-20 \cdot SoC_{UC}) + 20 & if \quad I_{Load} < 0 \quad SoC_{UC} > 95\% \\ 1 & if \quad 25\% \leq SoC_{UC} \leq 95\% \\ 0 & if \quad I_{Load} > 0 \quad 25\% < SoC_{UC} \\ 1 & if \quad I_{Load} < 0 \quad 25\% < SoC_{UC} \end{cases}$$

The first rule defines a hard upper limit where $M = 0$, when $SoC_{uc} = 100$ %. The modified current reference becomes zero, preventing the ultra-capacitor bank to become overcharged. When the load is positive (during energy transfer out of the ultra-capacitor bank), the ultra-capacitor is expected to discharge. Therefore, when $I_{Load} > 0$ and $SoC_{uc} = 100\%$, the logic block produces $M = 1$.

The third rule defines an upper transition region, where M smoothly decays to zero as SoC_{uc} goes from 95% towards 100 %. The values of the slope and the constant, here 20, determine the rate by which M changes in this region.

The fourth rule defines the normal operation region where $M = 1$ and $I'_{uc,ref} = I_{uc,ref}$. The fifth rule is to prevent discharging the ultra-capacitor below half of the rated voltage. This rule defines a lower limit with producing $M = 0$, when $SoC_{uc} < 25\%$. Finally, the sixth rule is to charge the ultra-capacitor bank even when SoC_{uc} is below 25 percent while the load current is negative (during energy transfer to the ultra-capacitor bank). Regardless the value of SoC_{uc}, it is desired for the energy coming from the load to be used for charging the ultra-

capacitor bank capacitor. Therefore, when $I_{Load} < 0$ and $SoC_{uc} < 25\%$, the logic block produces $M = 1$.

For a real system, a dissipative resistor bank is needed to be connected across the DC bus. This resistor is switched on to dissipate the regenerative braking energy in case of ultra-capacitor converter failure.

6.4 Simulations Results of Control Strategy 1

In the first control strategy, the MES interfaced boost converter works in voltage control mode to regulate the DC bus voltage around 180 Volts. Buck-boost converter works in current control mode. The current reference is generated from the moving average block that is explained in section 6.2. The size of the ultra-capacitor bank was determined in section 3.6.1 and presented in Table 3-3. The moving time window, T_m, should be chosen in a manner to fully utilize the ultra-capacitor bank ,.i.e., to fully discharge and charge it in one driving cycle.

In simulation, it is observed that reducing T_m below a certain limit affects the performance of the system. The reason is that the DC rail converter is a unidirectional current converter. Hence, the ultra-capacitor bank should be discharged whenever the power flow is from load to the DC bus. As such, the

ultra-capacitor bank can take the power flowing to the DC bus. Otherwise, the DC bus voltage builds up, resulting in system failure. This voltage can also damage the switches and diodes of the converters. Any T_m value below 40 s, leads to the above-mentioned problem for the system under study.

Among the other values of moving time window, $T_m = 60\ s$ fully utilizes the ultra-capacitor bank; it discharges almost completely during acceleration, starts to recharge a few seconds before the beginning of the deceleration and becomes completely charged by the end of one full cycle (100 s).

$P_{UC,ref}$ increases for T_m values over 60 s. As such, the ultra-capacitor bank capacity should also increase. This can be considered depending on the application as well as the load profile.

With this strategy and the selected value of 60 s for T_m , it is not possible to size the ultra-capacitor bank smaller that the capacity of Table (3-3). The reason is again voltage built up in the DC bus during regeneration. The current coming from the DC source is not analysed for percentage ripple and harmonics. It is assumed to be a pure DC source. The complete system simulation results are presented in sections 6.4.1, 6.4.2, and 6.4.3.

6.4.1 Results of rated load

The results of simulation with the rated 100 kg train mass are shown in Figure 6-2, Figure 6-3, and Figure 6-4. In Figure 6-3 the averaged boost converter output current is shown instead of its initial value. Since, the boost output current is a pulse train current which is the normal characteristic of the converter. As explained in section 4.6.2, the system is able to work with the pulse train current of the MES because this current will be smoothened by the motor drive converter. The control strategy works with this average current value, hence, it is presented here. It can be seen that the ultra-capacitor converter is providing the peak current during acceleration ($I_{converter,out}$). As such, the DC rail boost converter output current is smoothened around it average value (I_s). The ultra-capacitor current follows very closely its reference shown in purple (I_{UC}). The last graph in this figure is the machine armature current (I_a). The MES and AES are providing the demanded machine current, hence, the machine is working as it is supposed to.

From Figure 6-2, it is observed that the DC bus voltage is following the 180 Volts reference voltage with reasonable ripple percentage. The ultra-capacitor voltage shown in the same figure discharges to about its half-rated voltage first and then

recharges to its rated voltage in a full driving cycle.

In Figure 6-4, the machine performance is shown. The motor speed is following the reference speed in purple and the machine current is copying the load torque which comes from the metro model block. The results of simulation with the same strategy are shown for 20 percent more and less than rated train mass to emulate various possible real time situations.

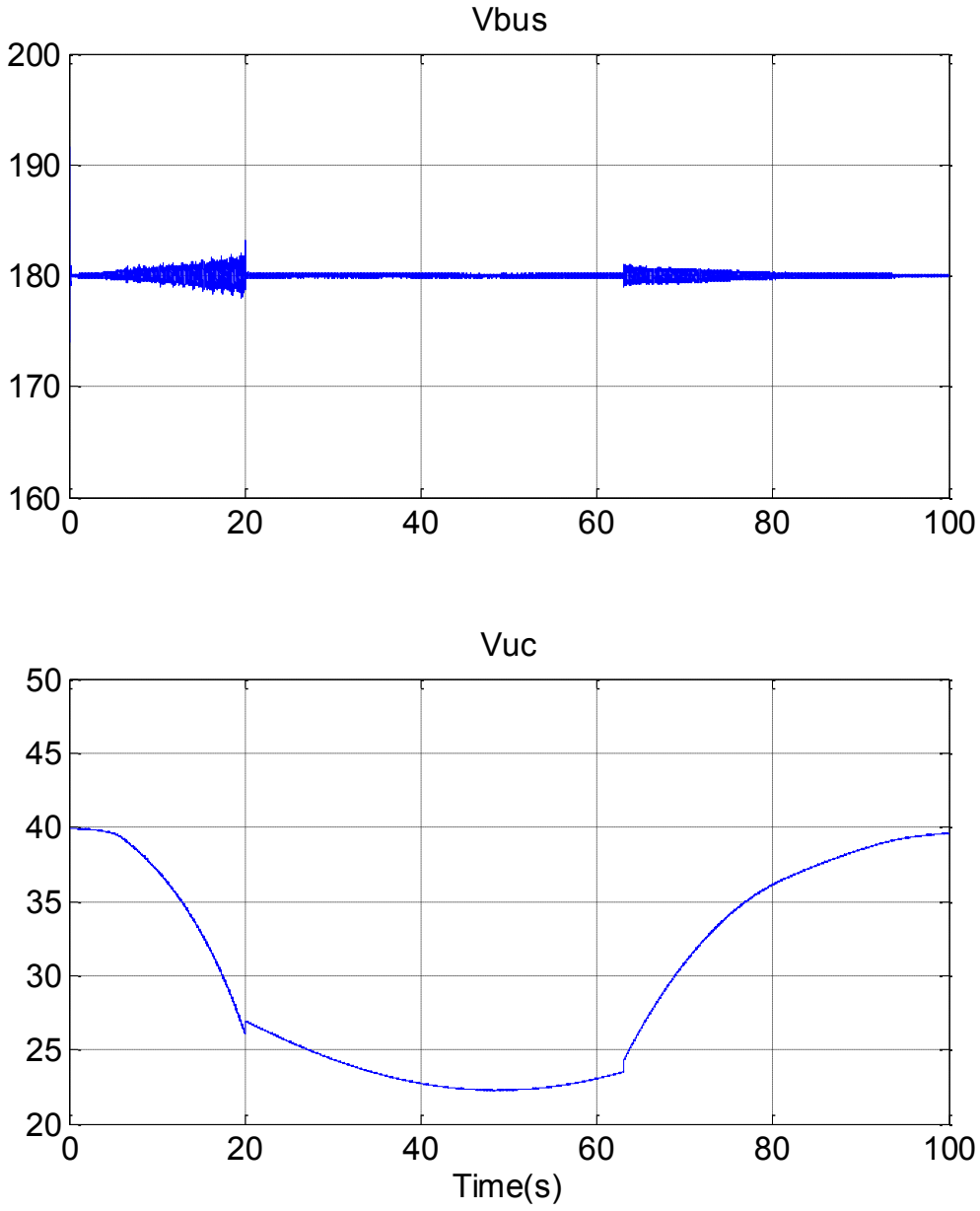

Figure 6-2: DC bus voltage and Ultra-capacitor bank voltage/Rated Load/Strategy1

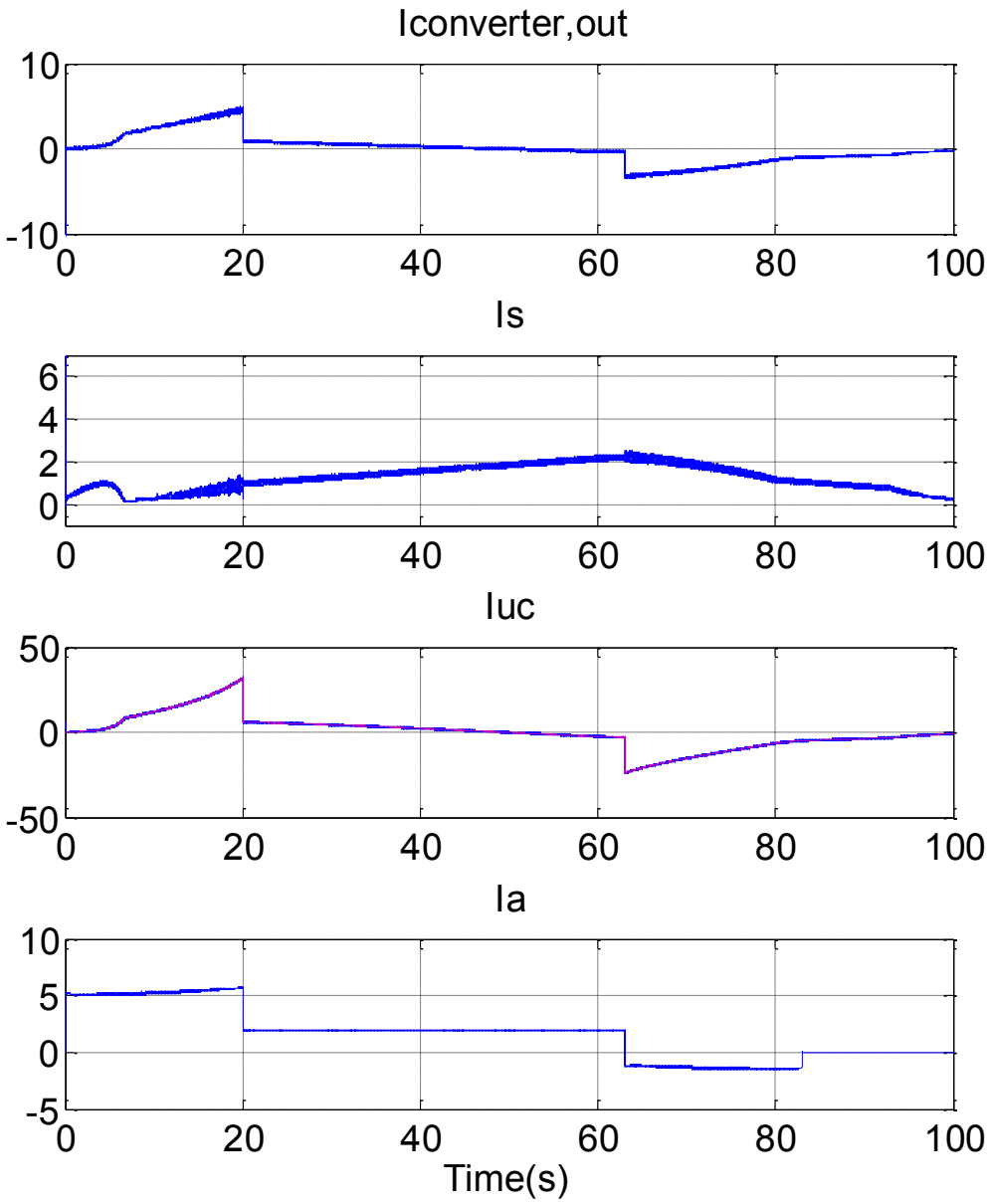

Figure 6-3: Averaged ultra-capacitor converter output current, Averaged DC rail boost converter output current, ultra-capacitor current, and motor drive current/Rated Load/ Strategy1

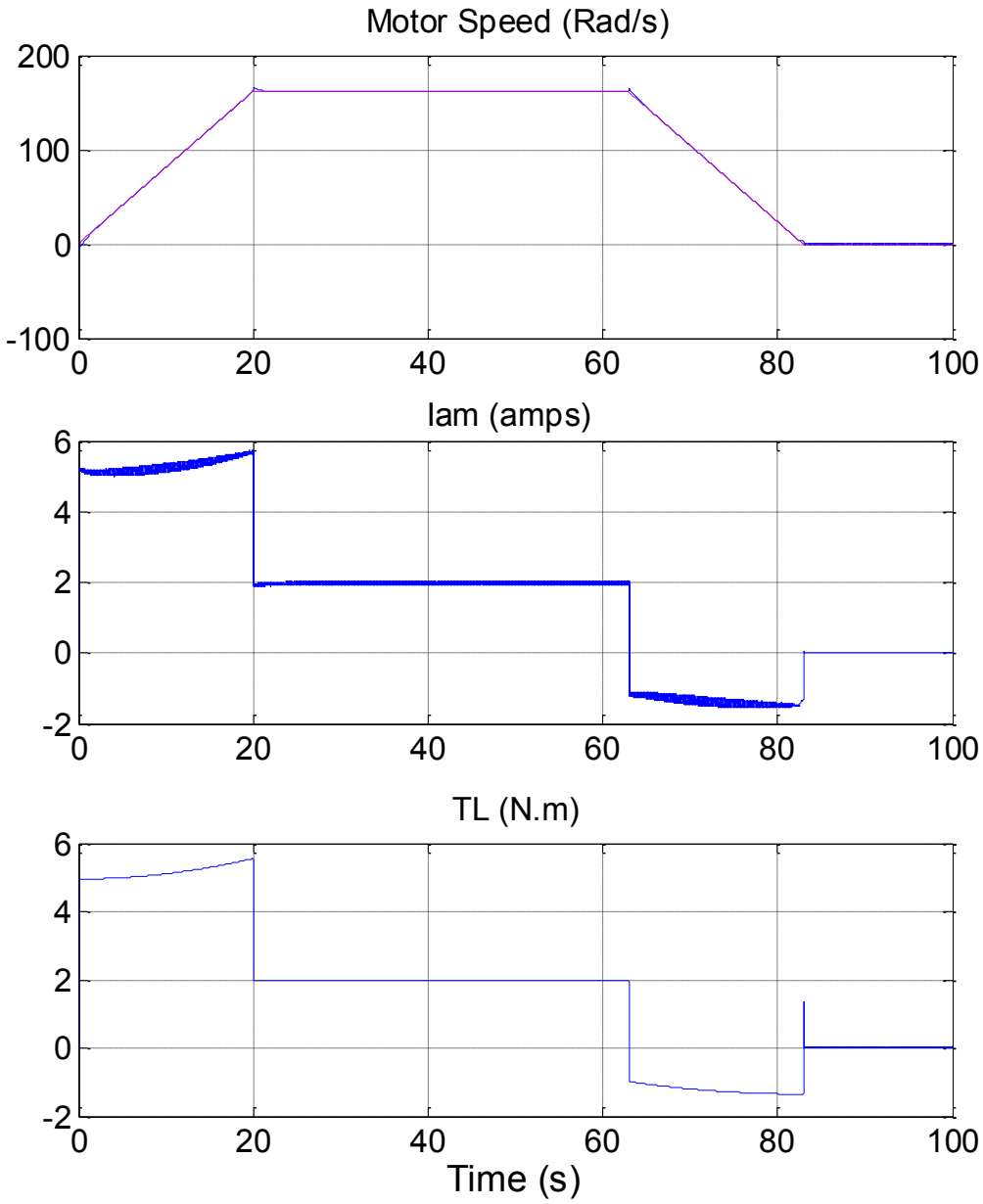

Figure 6-4: Motor speed, Armature current, and Load torque/Rated Load/Strategy1

6.4.2 Results of 20% more than rated load (120 kg)

From Figure 6-5, Figure 6-6, Figure 6-7 it can be seen that the system works satisfactorily with more than rated load. Moreover, the ultra-capacitor bank is

fully used. It is important to verify whether the ultra-capacitor bank is fully used with this load and the tuned average time window. Another important quality that needs to be verified is DC bus voltage control during braking. The simulation results confirm that the system is able to handle more than rated load while satisfying of the above mentioned requirements.

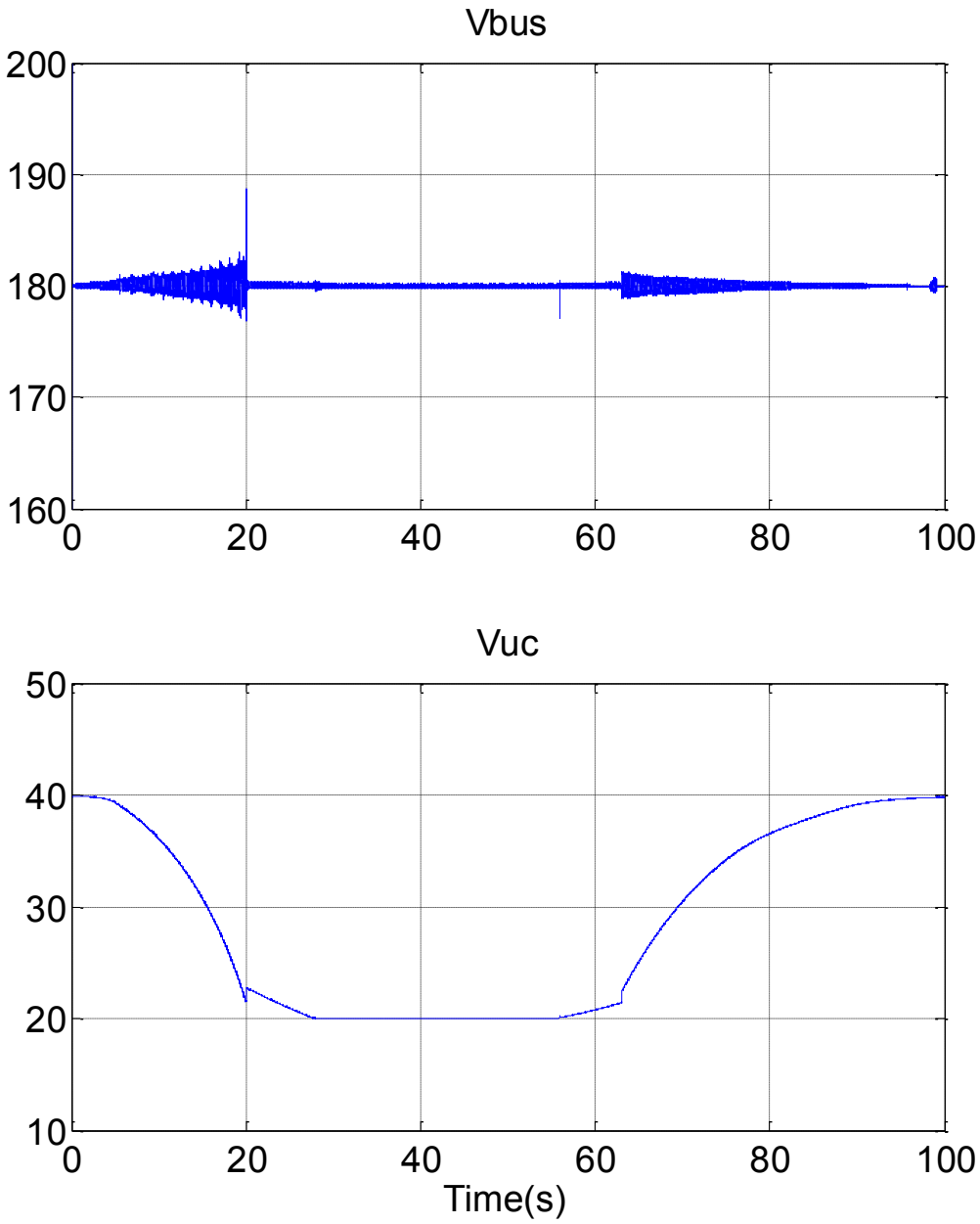

Figure 6-5: DC bus voltage and Ultra-capacitor bank voltage/20 % more than Rated Load/Strategy1

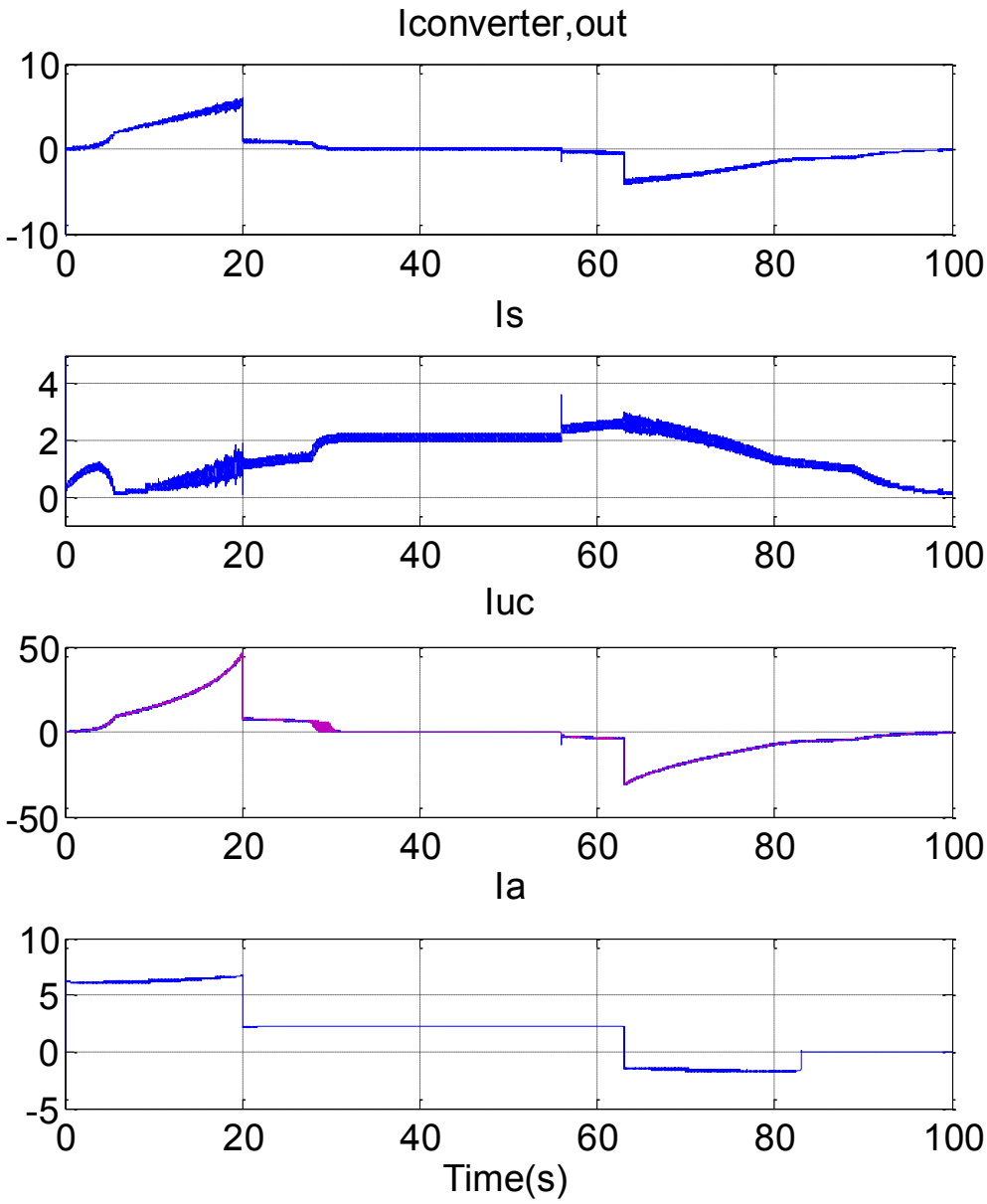

Figure 6-6: Averaged ultra-capacitor converter output current, Averaged DC rail boost converter output current, ultra-capacitor current, and motor drive current/20 % more than Rated Load/Strategy1

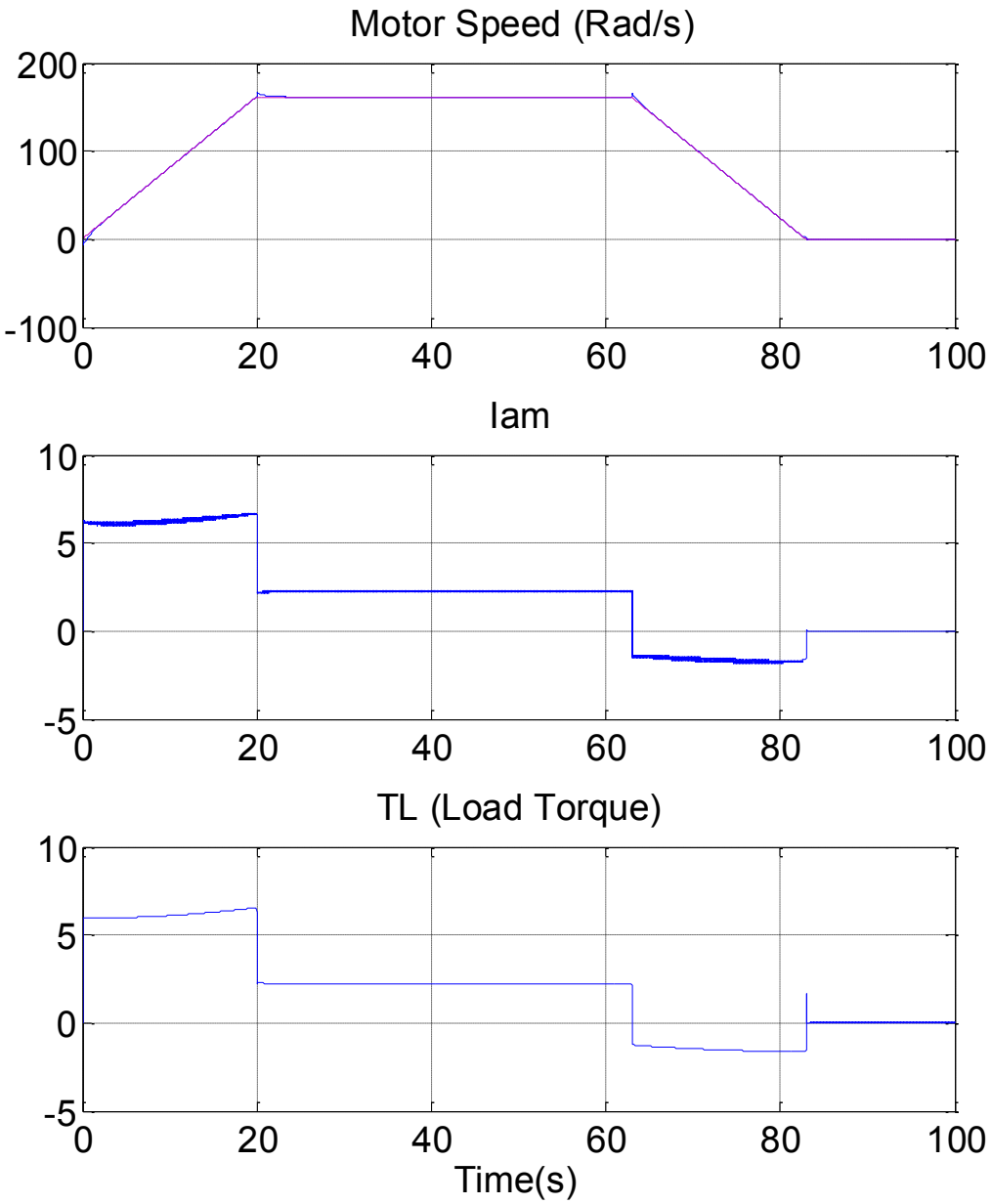

Figure 6-7: Motor speed, Armature current, and Load torque/20 % more than Rated Load/Strategy1

6.4.3 Results of 20% less than rated load (80 kg)

In this section, the simulation results are also satisfying the requirements mentions in section 6.4.2. This simulation is also done to verify ultra-capacitor

full utilization with the tuned average time window as well as the DC bus voltage regulation.

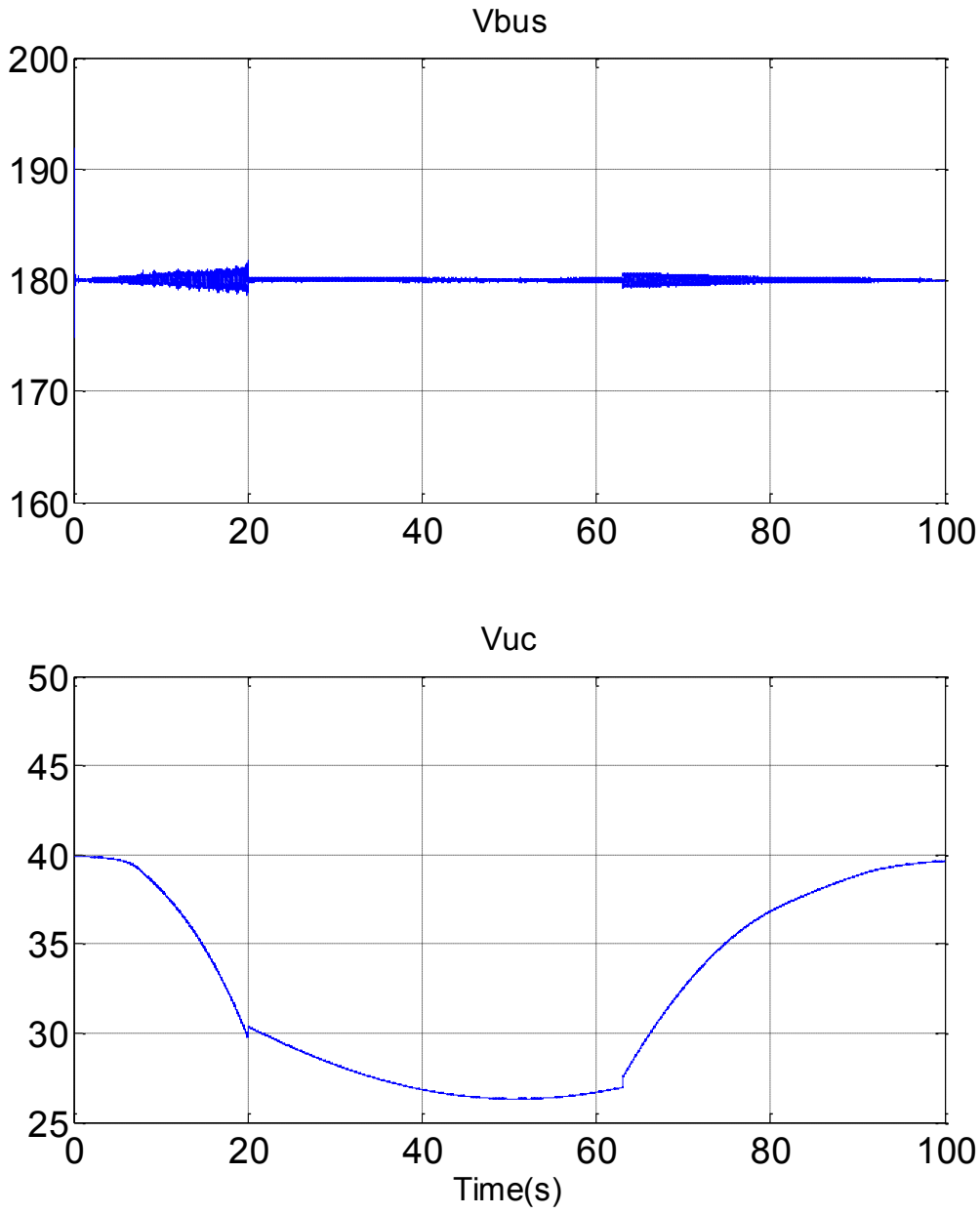

Figure 6-8: DC bus voltage and Ultra-capacitor bank voltage/20 % less than Rated Load/Strategy1

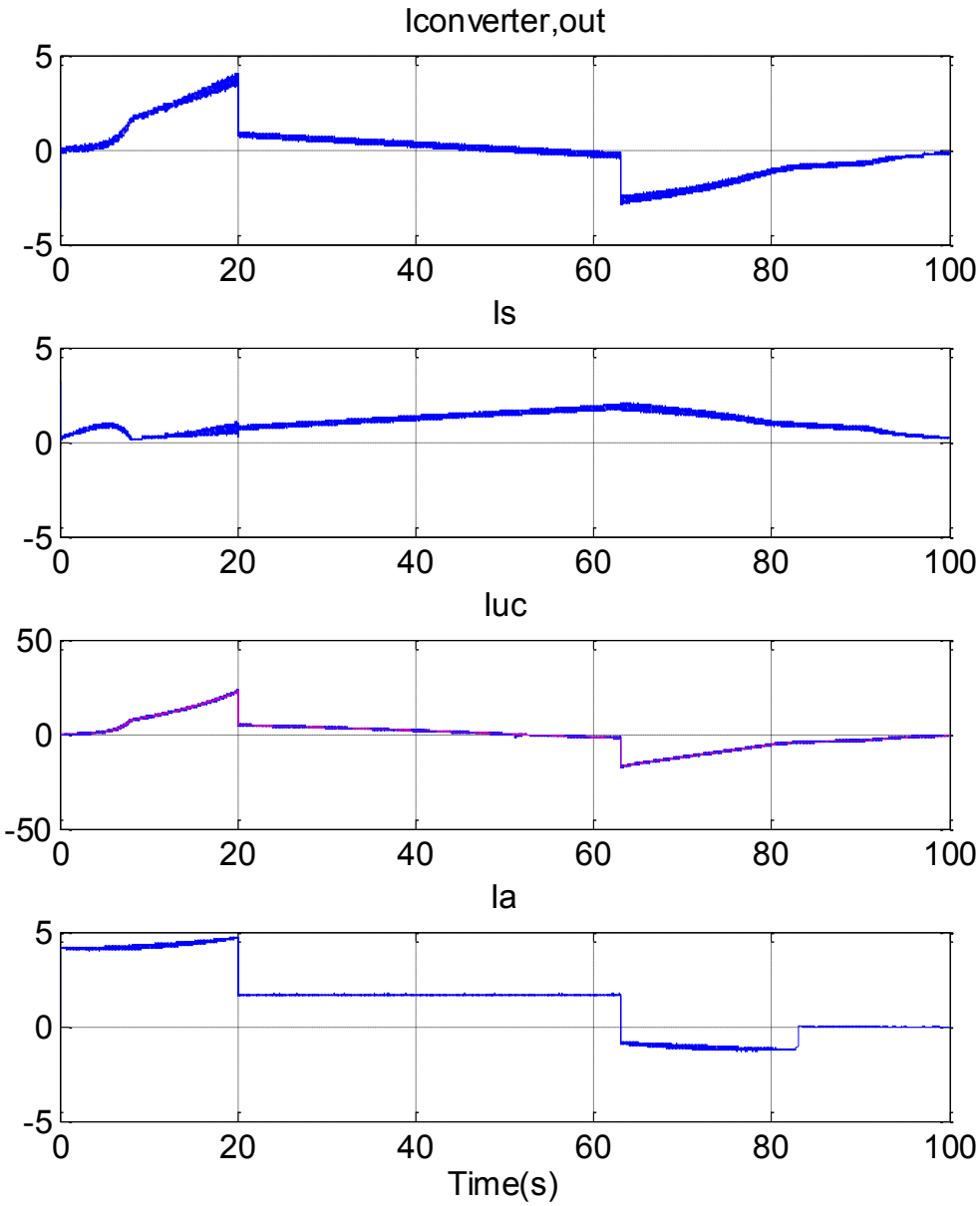

Figure 6-9: Averaged ultra-capacitor converter output current, Averaged DC rail boost converter output current, ultra-capacitor current, and motor drive current/20 % less than Rated Load/Strategy1

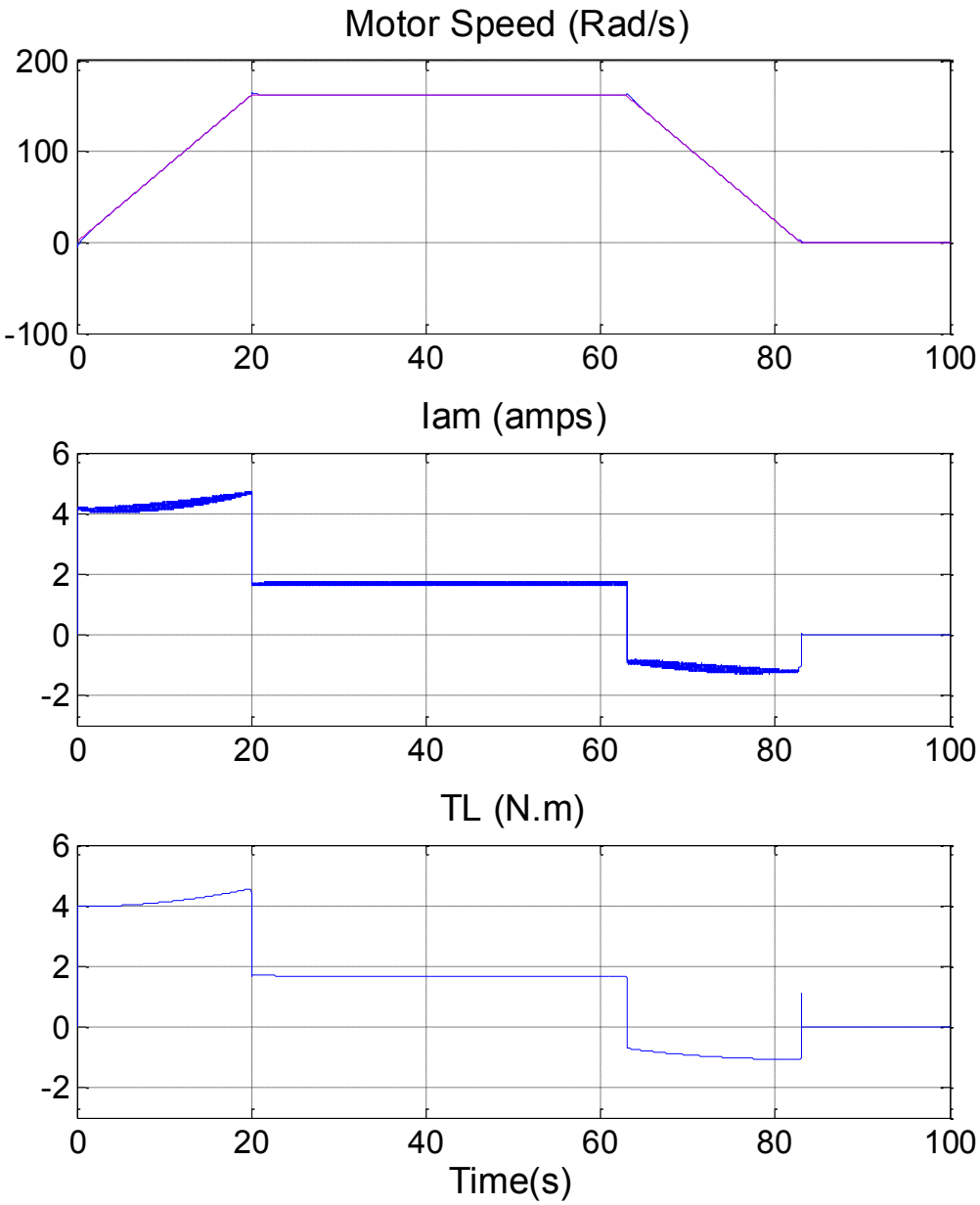

Figure 6-10: Motor speed, Armature current, and Load torque/20 % less than Rated Load/Strategy1

6.5 Simulations Results of Control Strategy 2

The control strategy developed in section 6.4 does not work for the ultra-capacitor bank size which were discussed in section 3.6.2, Table 3-4. The sizing shown in Table 3-4 is more reasonable according to the discussion in section 3.5,

i.e., sizing the ultra-capacitor bank to provide the peak acceleration energy. Here the need for another control algorithm comes to the picture.

The second control strategy works as the following: The ultra-capacitor buck-boost converter works in voltage control mode to regulate the DC bus voltage. The DC rail boost converter works in current control mode to provide the average load power. The moving average block is used to calculate the average load power by equation (6-1). However, here, the average load power is divided by the DC bus voltage to generate the DC rail boost converter current reference. As such, the average power coming from the DC rail can be controlled to satisfy the load requirements. After trying various values of T_m, 10 s is found to fully utilize the ultra-capacitor bank. The results of simulation with the rated load are shown in the section 6.5.1.

6.5.1 Results of rated load

The DC bus voltage is shown in Figure 6-11. The voltage ripple is within the desired range of five percent, with a five-percent overshoot at the end of acceleration period (t=20(s)) and 2.5 percent at the beginning of the deceleration period (t=63(s)). The two significant overshoots happen because now the DC bus voltage is being controlled with ultra-capacitor converter, hence, it is sensitive to

ultra-capacitor current behavior. The DC bus voltage overshoots at t=20 s and t=63 s when ultra-capacitor current has an abrupt change as seen in Figure 6-12. These overshoots are still in the defined range, therefore, not harmful to the system. The ultra-capacitor voltage fully discharges during acceleration then gets recharges to its rated voltage during constant speed and braking periods.

The ultra-capacitor current follows its reference in Figure 6-12. The DC rail peak current is reduced with the help of the ultra-capacitor bank current. The DC rail current and the ultra-capacitor bank current are providing the machine current during one complete cycle, thus, the system works satisfactorily.

The machine drive simulation results are shown in Figure 6-13. The machine speed closely follows the drive cycle and the demanded machine is being provided by MES and AES. The simulation results of 20 percent more and less than the rated train mass are presented in sections 6.5.2 and 6.5.3 to verify the ultra-capacitor bank full utilization and DC bus regulation under other possible loads.

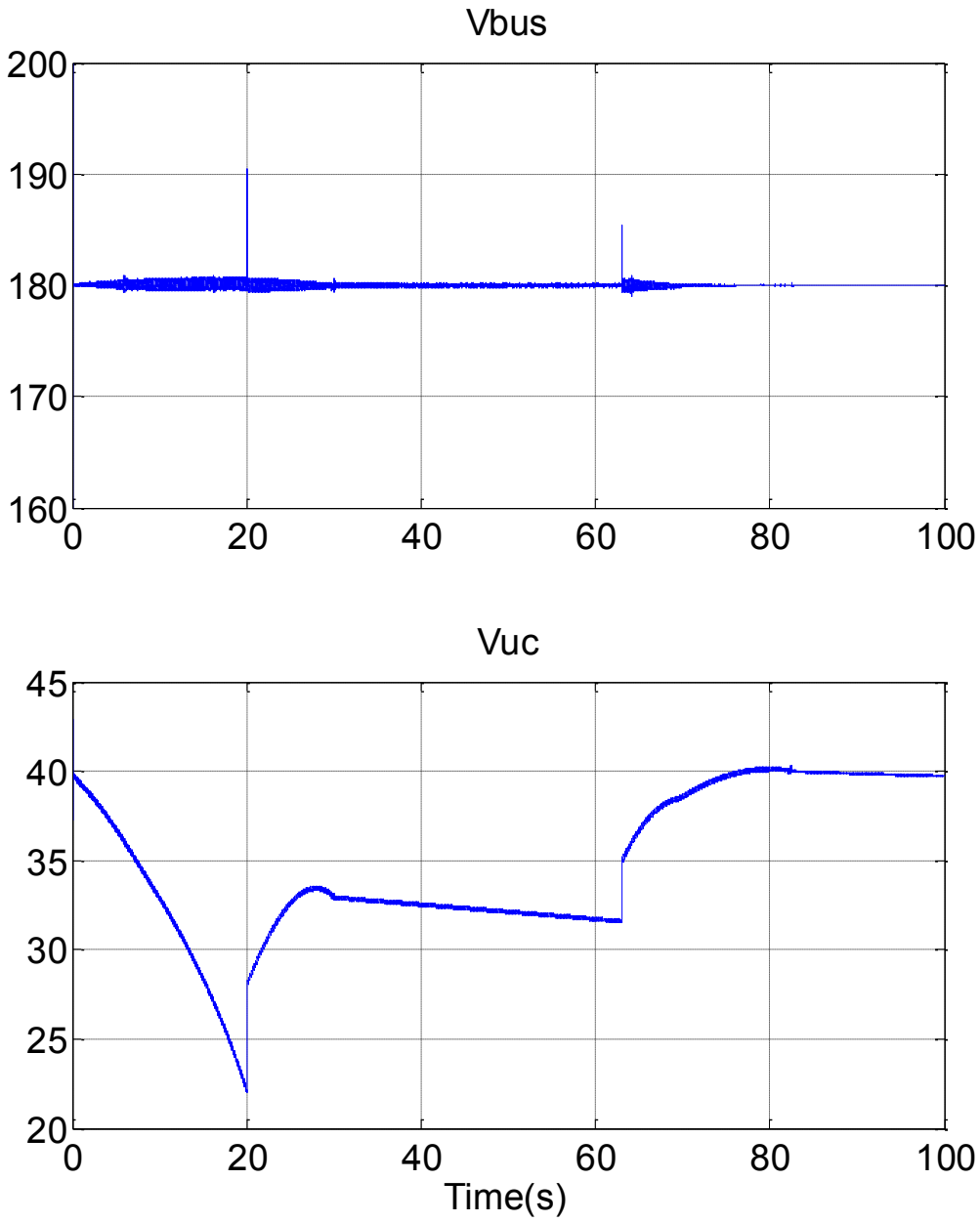

Figure 6-11: DC bus voltage and Ultra-capacitor bank voltage/Rated Load/Strategy2

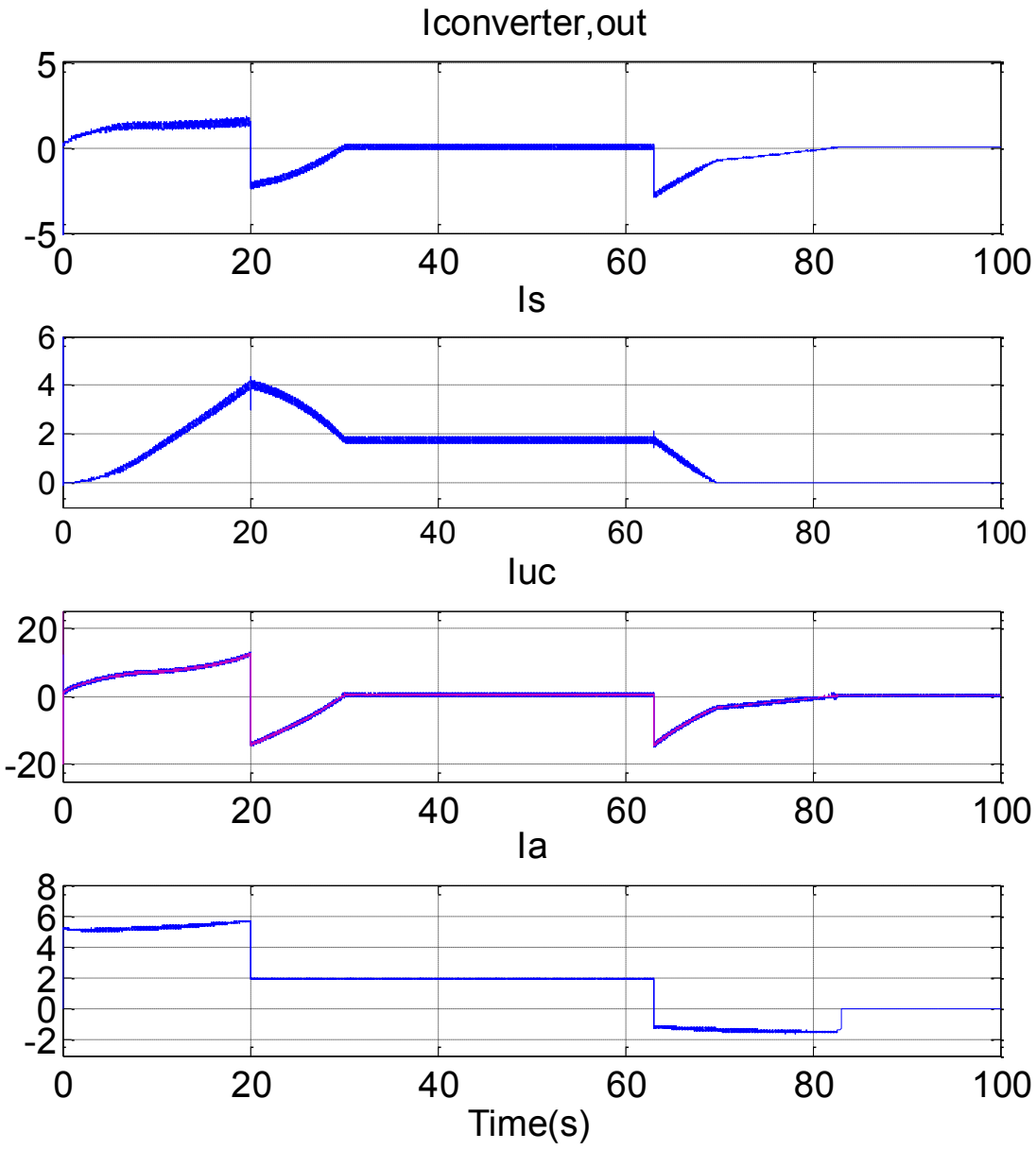

Figure 6-12: : Averaged ultra-capacitor converter output current, Averaged DC rail boost converter output current, ultra-capacitor current, and motor drive current/Rated Load/ Strategy2

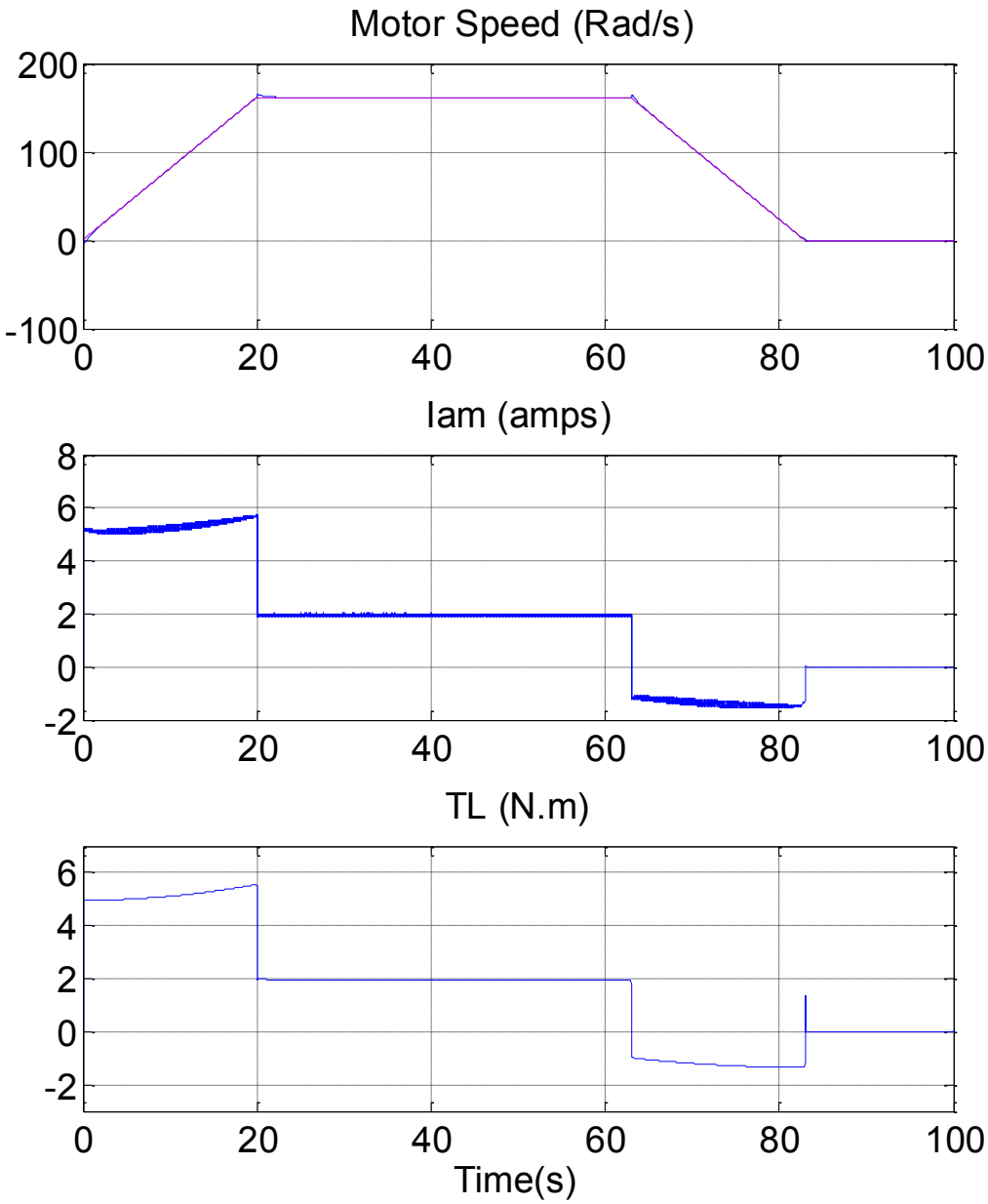

Figure 6-13: Motor speed, Armature current, and Load torque/Rated Load/Strategy2

6.5.2 Results of 20% more than rated load (120 kg)

From Figure 6-14, Figure 6-15, and Figure 6-16 it can be seen the ultra-capacitor bank is fully with moated load with tuned average time window. The DC bus

voltage is also within the desired range specially during braking. Therefore, the system is able to handle more than rated load while satisfying of the above mentioned requirements.

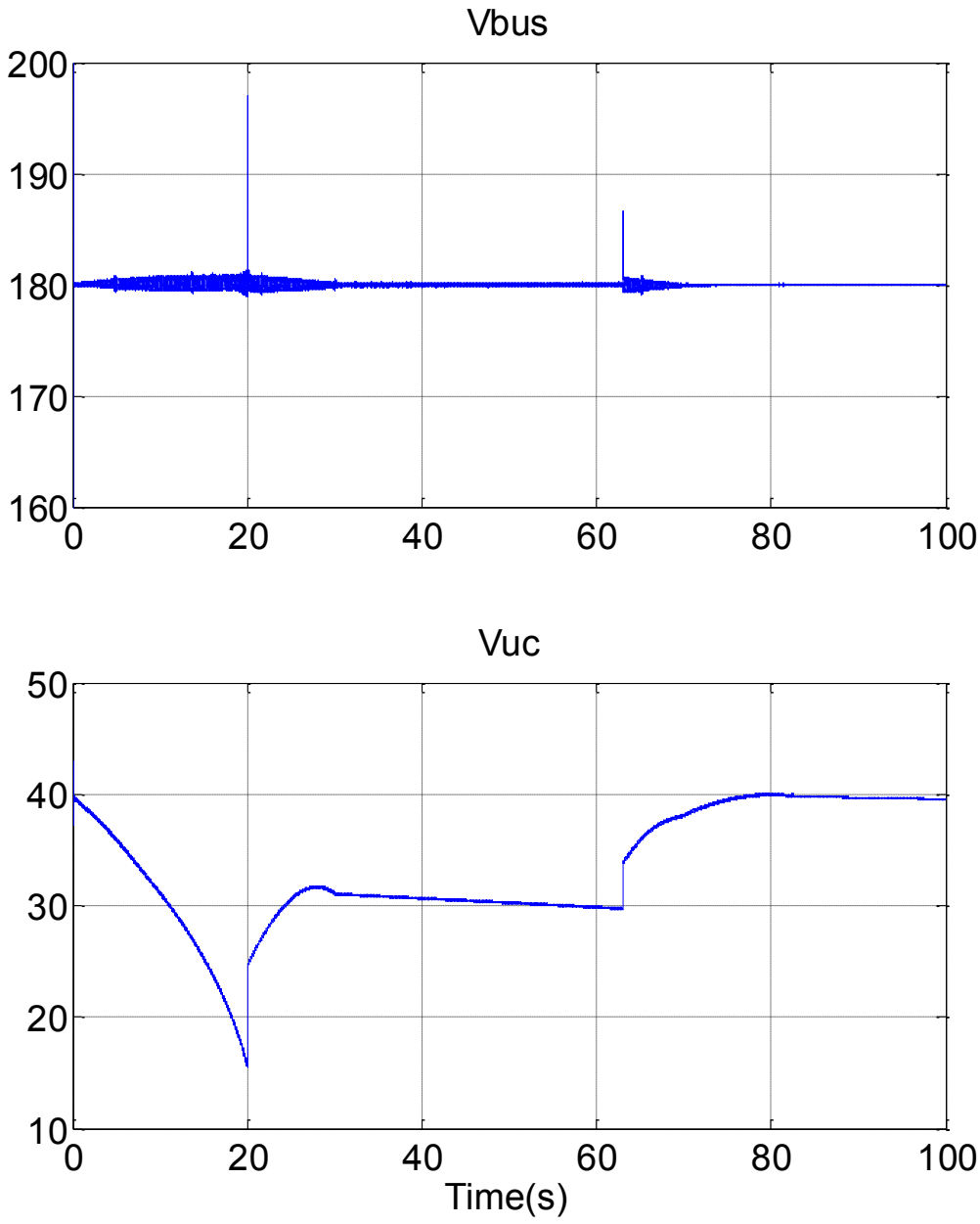

Figure 6-14: DC bus voltage and Ultra-capacitor bank voltage/20 % more than Rated Load/Strategy2

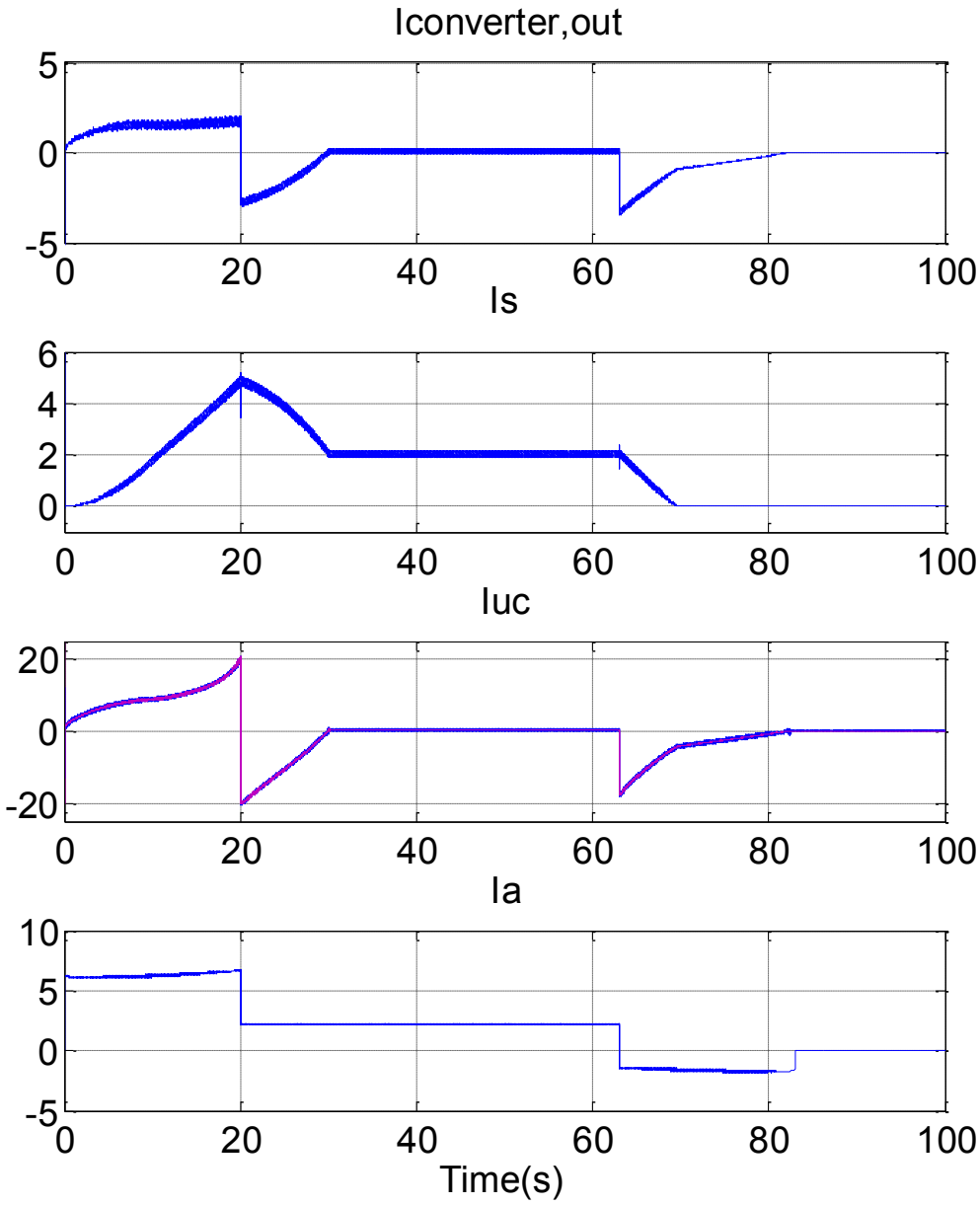

Figure 6-15: Averaged ultra-capacitor converter output current, Averaged DC rail boost converter output current, ultra-capacitor current, and motor drive current/20 % more than Rated Load/Strategy2

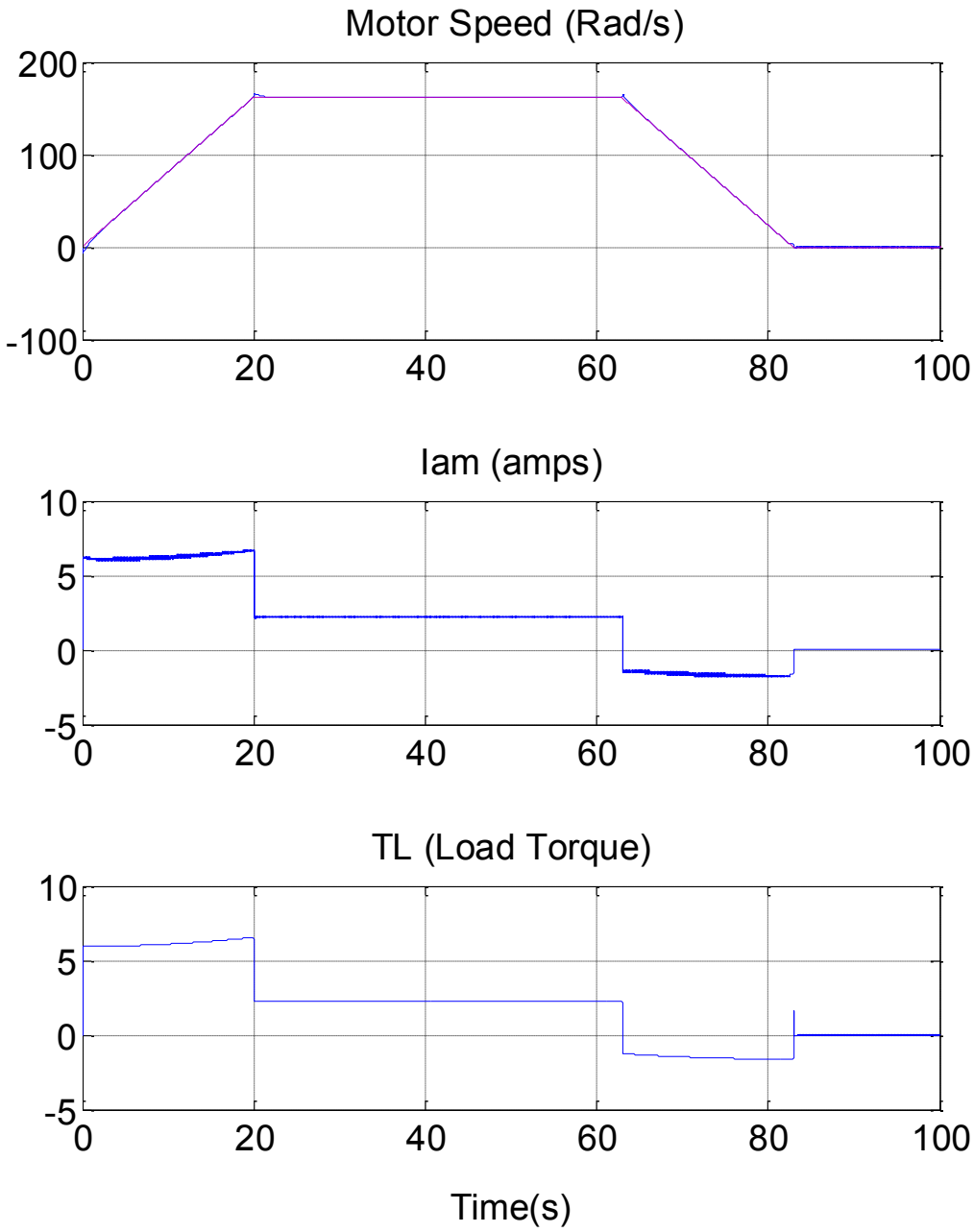

Figure 6-16: Motor speed, Armature current, and Load torque/20 % more than Rated Load/Strategy2

6.5.3 Results of 20% less than rated load (80 kg)

In this section, the simulation results are also satisfying the requirements mentions in section 6.5.3. This ultra-capacitor bank full utilization is verified with the tuned average time window. The DC bus voltage is also regulated around 180 Volts.

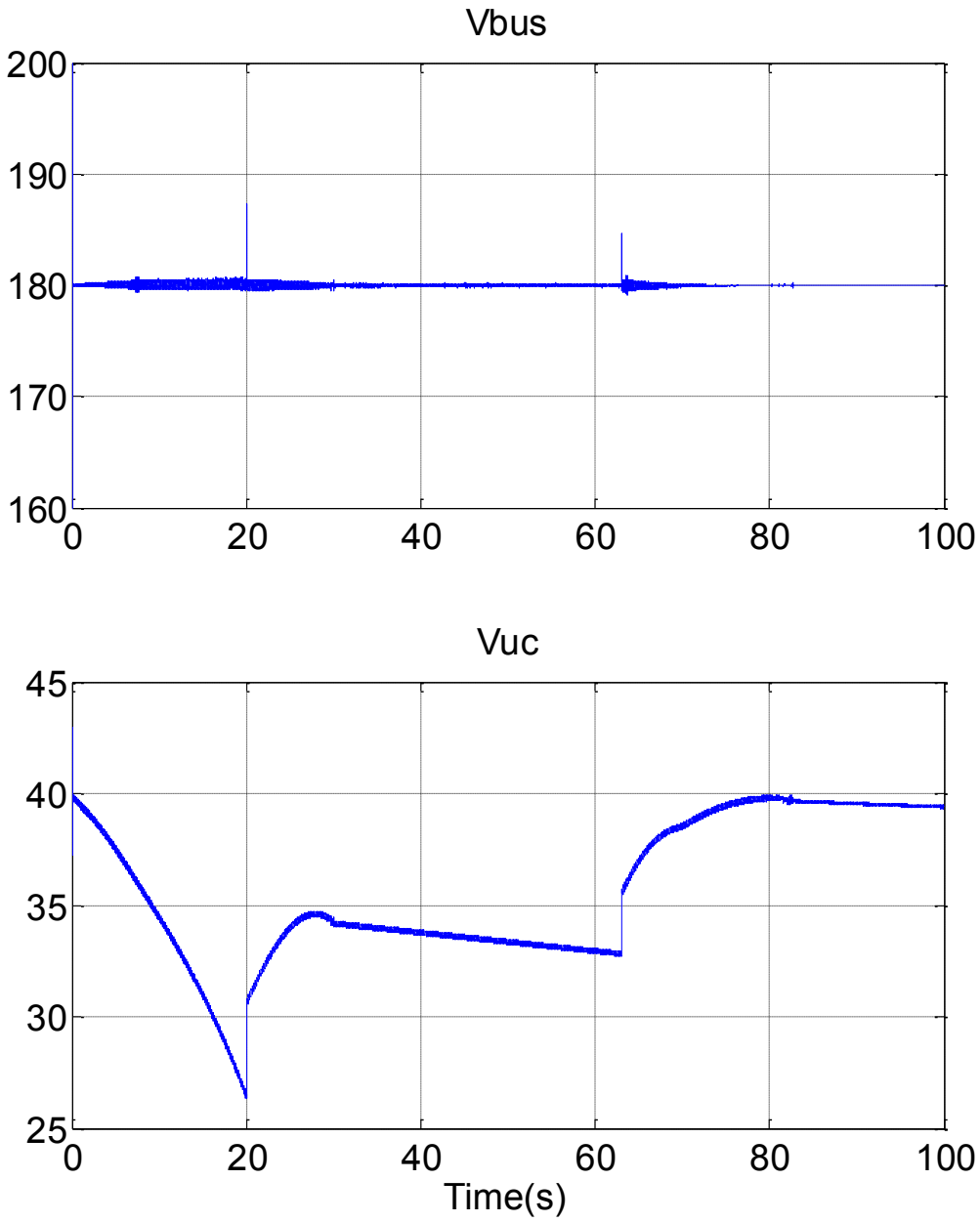

Figure 6-17: DC bus voltage and Ultra-capacitor bank voltage/20 % less than Rated Load/Strategy2

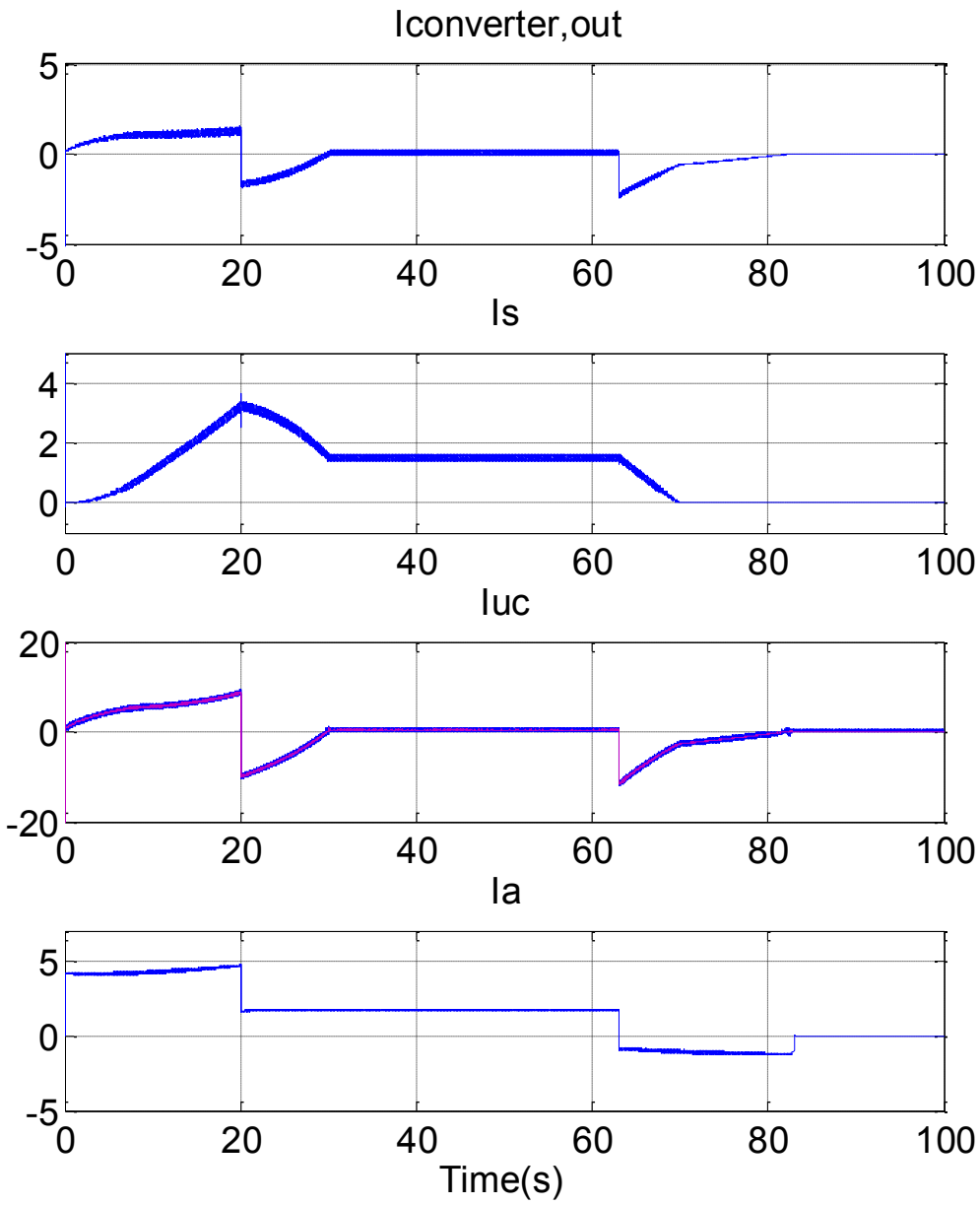

Figure 6-18: Averaged ultra-capacitor converter output current, Averaged DC rail boost converter output current, ultra-capacitor current, and motor drive current/20 % less than Rated Load/Strategy2

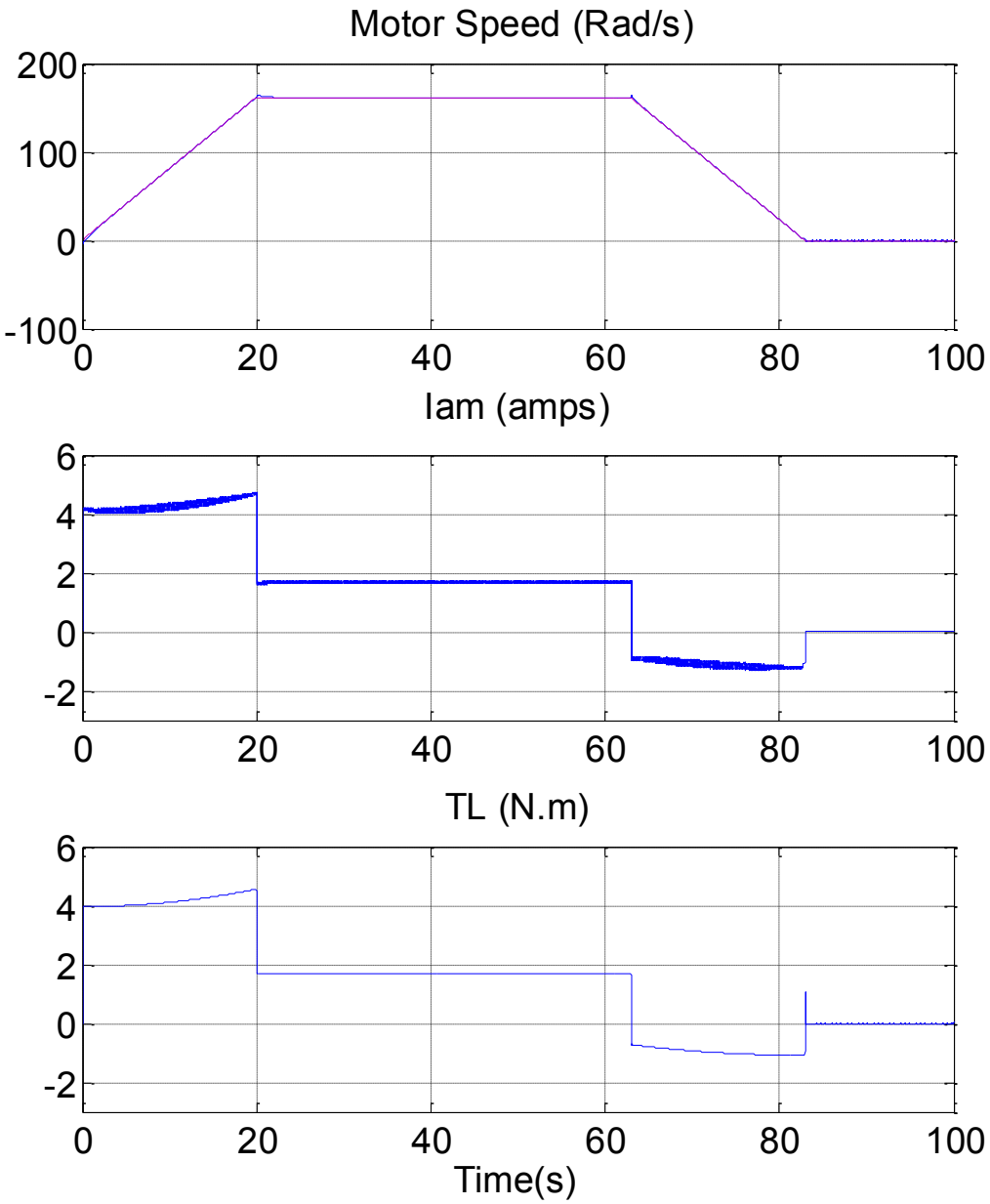

Figure 6-19: Motor speed, Armature current, and Load torque/20 % less than Rated Load/Strategy2

6.6 **Summary**

The developed control strategy for the scaled down Montreal metro system was presented followed by its working principal in chapter 6. To protect the ultra-

capacitor bank, an over-voltage and under-voltage protection system was developed in Matlab/Simulink.

Two control strategies were developed; one for the ultra-capacitor bank sized to provide the acceleration energy and the second one for the ultra-capacitor bank sized to provide the peak acceleration energy.

The first supervisory control strategy was tuned for the system with the first ultra-capacitor bank size. The maximum ultra-capacitor utilization point was found. From discussions about the simulation results, it was concluded that the algorithm could not work for the second designed ultra-capacitor bank size. Thus, a second control strategy was developed and validated through simulations.

Chapter 7: Conclusions and Future Work

7.1 Conclusions

In this thesis a supervisory control unit was developed to perform peak power smoothing via ultra-capacitor for electrified metro transit application. The system operation was regulated by the supervisory control unit in which a well-defined control strategy is implemented.

In chapter 2, the Montreal metro train-set model MR73 was introduced. The power and torque calculation was done for a nine car composition with this train-set model. The results were used to analyse the hybridization of the MES via ultra-capacitors in chapter 4.

The ultra-capacitor was introduced in chapter 3 and an appropriate ultra-capacitor model was selected for metro transit application. A sizing method was developed then applied for the Montreal metro system. Since the results of the sizing to supply the whole acceleration energy were not financially and technically reasonable, a second sizing method was developed. The second sizing method sizes the AES to provide only the peak acceleration energy. The results of the second sizing method were satisfactory.

For the purpose of simulation, the initial full scale metro model was scaled down. The scaling down procedure was explained then ultra-capacitor bank sizing was done for the scaled model. The two previously developed sizing methods were applied to the scaled down model. The results were used in the simulations in chapter 6.

In chapter 4, the ultra-capacitor interfaced bidirectional DC/DC converter was designed and the control requirements for metro transit application were defined based on a 2 Hp machine's controlled drive load. This machine represented the metro traction motor. PI controllers based on the control requirements were designed to perfume current and voltage control. In designing the controllers, the issue of the converter inherited nonlinearities was reflected and effective solutions were proposed. Then, the same steps were taken for the DC rail Boost converter and controller design. The PI controllers designed for both buck-boost and boost converters were used in simulation in chapter 6.

In chapter 5, the basics of the permanent magnet DC machine were explained. Parameters of the 2 Hp Baldor CDPW3585 PMDC machine were experimentally determined then used to model the machine and achieve speed regulation in Matlab/Simulink. PI controllers were designed to satisfy the time domain requirements of the machine's controlled drive.

The developed control strategy for the scaled down Montreal metro system was presented followed by its working principal in chapter 6. To protect the ultra-capacitor bank, an over-voltage and under-voltage protection system was developed in Matlab/Simulink.

Two control strategies were developed; one for the ultra-capacitor bank sized to provide the acceleration energy and the second one for the ultra-capacitor bank sized to provide the peak acceleration energy. Both sizes of the ultra-capacitor bank can be used in the metro system, however they do not work with the same control strategy.

The first supervisory control strategy was tuned for the system with the first ultra-capacitor bank size. The maximum ultra-capacitor utilization point was found. In discussions about the simulation results of the first control strategy, it was clarified that why the algorithm could not work for the second designed ultra-capacitor bank size. Then, a second control strategy was developed and validated through simulations for the ultra-capacitor bank sized to provide the peak acceleration energy.

7.2 **Future Work**

In this work, for simplicity some assumptions were made. The converters were

assumed to be ideal, i.e., all the switches and filter capacitors were considered ideal with no losses and zero turn-on or turn-off time. The parasitic elements such as resistors, inductors, capacitors and ESR were not considered in converter and ultra-capacitor modeling. Considering these elements may increase the order of the system and will change the system model and finally will make deriving system transfer functions sophisticated. Taking these factors into account can be considered as future work.

Switching losses in the IGBT switches and diodes are not studied in this thesis. Calculating and analyzing these losses can give valuable information for experimental implementation.

Experimental setup construction of this work and comparison with simulation results is also valuable.

Another potential work can be considered as analyzing other supervisory control schemes. Modern control optimization techniques such as feedback control can be employed for the system. Comparing the results of applying modern control techniques to this system with the results of classic control theory applied in this thesis is valuable.

Bibliography

[1] P. Grbović, P. Delarue, P. Le Moigne and P. Bartholomeus, "The Ultracapacitor-Based Regenerative Controlled Electric Drives With Power-Smoothing Capability," *IEEE Transactions on Industrial Electronics,* vol. 59, no. 12, pp. 4511-4522, 2012.

[2] M. Ortuzar, *Design, Implementation and Evaluation of an Auxillary Energy System for Electric Vehicles, Based on Ultracapacitors and Buck-Boost Converter,* Santiago de Chile: Pontificia Universidad Catolica de Chile, 2005.

[3] L. H. Seim, *Modeling, Control and Experimental Testing of a Supercapacitor/Battery Hybrid System Passive and Semi-Active Topologies,* Kjeller: Norwegian University of Life Sciences, 2011.

[4] W. Lhomme, P. Delarue, P. Barrade, A. Bouscayrol and A. Rufer, "Design and Control of a supercapacitor storage system for traction applications," in *Industry Applications Conference*, Villeneuve d'Ascq, 2005.

[5] P. J. Grbović, P. Delarue, P. L. Moigne and P. Bartholomeus, "A Bidirectional Three-Level DC–DC Converter for the Ultracapacitor Applications," *IEEE Transactions on Industrial Electronics,* vol. 57, no. 10, pp. 3415-3430, 2010.

[6] M. Camara, H. Gualous, B. Dakyo and P. M. C.Nichita, "Buck-Boost

converters design for Ultracapacitors and lithium Battery mixing in Hybrid Vehicle Applications," in *Vehicle Power and Propulsion Conference (VPPC)*, Lille, 2010.

[7] M. Camara, H. Gualous, F. Gustin and A. Berthon, "Control strategy of Hybrid sources for Transport applications using supercapacitors and batteries," in *CES/IEEE 5th International Power Electronics and Motion Control Conference*, Shanghai, 2006.

[8] M. Camara, H. Gualous, F. Gustin and A. Berthon, "Design and New Control of DC/DC Converters to Share Energy Between Supercapacitors and Batteries in Hybrid Vehicles," *IEEE Transactions on Vehicular Technology,* vol. 57, no. 5, pp. 2721-2735, 2008.

[9] M. Ortuzar, J. Moreno and J. Dixon, "Ultracapacitor-Based Auxiliary Energy System for an Electric Vehicle: Implementation and Evaluation," *IEEE Transactions on Industrial Electronics,* vol. 54, no. 4, pp. 2147-2156, 2007.

[10] M. Camara, F. Gustin, H. Gualous and A. Berthon, "Supercapacitors and battery power management for hybrid vehicle applications using multi boost and full bridge converters," in *European Conference on Power Electronics and Applications*, Aalborg, 2007.

[11] M. B. Camara, H. Gualous, F. Gustin and A. Berthon, "DC/DC Converter Design for Supercapacitor and Battery Power Management in Hybrid Vehicle Applications—Polynomial Control Strategy," *IEEE Transactions on Industrial Electronics,* vol. 57, no. 2, pp. 587-597, 2010.

[12] P. Grbović, P. Delarue and P. Le Moigne, "Selection and Design of Ultra-Capacitor Modules for Power Conversion Applications: From Theory to Practice," in *7th International Power Electronics and Motion Control Conference (IPEMC)*, Harbin, 2012.

[13] B. Bouquain David, D. Romain and C. Daniela, "Etude de l'hybridation du métro de Montréal type MR-73," Institut Supérieur d'Automobile et Transport (ISAT), University of Burgundy, France, 2013.

[14] S. S. Williamson, *Lecture Notes in Electric and Hybrid Electric Vehicles,* Montreal: Concordia University, 2011.

[15] H. Zha and Z. Zong, "Emulating Electric Vehicle's Mechanical Inertia Using an Electric Dynamometer," in *International Conference on Measuring Technology and Mechatronics Automation (ICMTMA)*, Changsha City, 2010.

[16] I. Husain, Electric and Hybrid Vehicles Design Fundamentals, Akron: CRC PRESS, 2005.

[17] J. Lee and D. Nelson, "Rotating inertia impact on propulsion and regenerative braking for electric motor driven vehicles," in *IEEE Conference on Vehicle Power and Propulsion*, Blacksburg, 2005.

[18] S. Mason, *The Effects of Rotational Inertia on Automotive Acceleration.*

[19] H. J. Zhang, "Application Note 140: Basic Concepts of Linear Regulator and Switching Mode Power Supplies," Linear Technology, 2013.

[20] P. Johansson and B. Andersson, *Comparison of Simulation Programs for*

Supercapacitor Modelling; Model Creation and Verification, Gothenburg: Chalmers University of Technology, 2008.

[21] C. Tammineedi, *Modeling Battery-Ultracapacitor Hybrid Systems For Solar and Wind Applications,* State College: The Pennsylvania State University, 2011.

[22] R. Faranda, M. Gallina and D. Son, *A new simplified model of Double-Layer Capacitors,* Milan: Politecnico di Milano, 2013.

[23] R. Barrero, J. V. Mierlo and a. X. Tackoen, *Enhanced Energy Storage Systems for Improved On-Board Light Rail Vehicle Efficiency,* 2008.

[24] *Datasheet 125V Heavy Transportation Modules,* Maxwell Technologies.

[25] *Maxwell Datasheet of Medieum Cells from 310 Farad to 350 Farad,* Maxwell Technology.

[26] L. A. Lopes, *Lecture Notes in Power Electronics I,* Montreal: Concordia University, 2011.

[27] N. Mohanl, T. Undeland and W. Robbins, Power Electronics: Converters, Applications and Design, 3rd ed., John Wiley & Sons, Inc, 2003.

[28] M. Ortuzar, J. Dixon and J. Moreno, "Design, construction and performance of a buck-boost converter for an ultracapacitor-based auxiliary energy system for electric vehicles," in *The 29th Annual Conference of the IEEE Industrial Electronics Society*, Roanoke, 2003.

[29] N. Mohan, Power Electronics and Drives, Minneapolis: MNPERE, 2003.

[30] L. A. Lopes, *Lecture Notes in Power Electronics II*, Montreal: Concordia University, 2012.

[31] K. Ogata, Modern Control Engineering, 5th ed., New Jersey: Prentice Hall, 2009.

[32] A. Shafiei, *Modeling, Analysis, and Design of a PV-Based Grid-Tied Plug-in Hybrid Electric Vehicle Battery Pack Charger*, Montreal: Concordia University, 2013.

[33] R. L. Barrett, "Switchmode Boost Power Converter Using Voltage-Mode Control," www.suncam.com, Fort Lauderdale.

[34] M. A. Johnson and M. H. Moradi, PID Control: New Identification and Design Methods, Springer Science & Business Media, 2005.

[35] A. Balestrino, A. Landi and L. Sani, "Closed loop tests for performance evaluations of controlled DC-DC switching converters," in *IEEE International Symposium on Industrial Electronics*, Ajaccio, 2004.

[36] D. Meeks, "Application Report: Loop Stability Analysis of Voltage Mode Buck Regulator With Different Output Capacitor Types – Continuous and Discontinuous Modes," Texas Instruments, 2008.

[37] B. Singh, R. P. Payasi, K. S. Verma, V. Kumar and S. Gangwar, "Design of controllers PD, PI, and PID for speed control of dc motor using IGBT based Chopper," *Electronic Journal: German Journal of Renewable and*

Sustainable Energy Research (GJRSER), vol. 1, no. 1, pp. 29-49, 2013.

[38] S. Williamson and J. Woods, *ELEC 440 Controlled Electric Drives Laboratory Manual,* Montreal: Concordia University, 2013.

[39] F. Andersson and L. Karlsson, *High efficiency actuators,* Göteborg: Chalmers University of Technology, 2007.

[40] R. Krishnan, Electric Motor Drives, Modeling, Analysis, and Control, Preintice Hall Inc., 2001.

[41] S. Williamson, *Letcure Notes in Controlled Electric Drives,* Montreal: Concordia University, 2012.

Appendices

Appendix 1: Matlab Codes of the Metro Train Model Block

```
function y = Trainmodel(u1,   u2, u3)
V = 0.125*0.48*u1;
%der_V = u2
%u3 load percentage
A=9.15;
g=9.8;
Co=0.01;
C1=6e-6;
GR=8;
r=0.48;
p=1.204;
Cd=0.4;
M=1.1*u3;% to consider the rotational acceleration force
Fg=u3*g*0.01047;
etaM=0.882;
etaG=0.686;
FAD=2.2*(V^2);
Froll=u3*g*(Co+C1*(V^2));
Fa=M*u2;
Ft=Fg+FAD+Froll+Fa;
Ttr=Ft*r;
if  u2<0 ;
    Ttm=(Ttr/GR)*etaG;
```

```
else
     Ttm=(Ttr/GR)/etaM;
end
y = Ttm;
```

Appendix 2: Detailed Power and Torque calculations for MR73 Train-set

- Acceleration Mode (0-40 sec)

Calculations in this section are done based on the predefined conditions in Table 2-2, Table 2-3, Table 2-4, Table 2-5, and Table 2-6.

Tire inertia from Table 2-4 is:

$$J_t = 3.1675\,(\mathrm{kg}/\mathrm{m}^2)$$

The total inertia is calculated from equations (2-5), (2-6), and (2-7).

$$J_1 = 2N_x J_t = 72 \times 3.1675 = 228\,(\mathrm{kg}/\mathrm{m}^2)$$

$$J_2 = 12288\,(\mathrm{kg}/\mathrm{m}^2)$$

$$J = 12516\,(\mathrm{kg}/\mathrm{m}^2)$$

The results of calculations for the acceleration mode is presented in Figure 2-10. Checking the rule of thumb, the calculated $F_{a2} = 12516$ N is about eight percent

of $F_{a1} = 156283$ N. The two percent discrepancy might be caused by the approximate tire inertia calculation.

The total averaged traction force is:

$$F_{TR} = 244.5\,(\text{kN})$$

The force per tire from equation (2-34) is:

$$F_t = \frac{F_{TR}}{48} = 5.0875\,(\text{kN.m})$$

Torque per tire from equation (2-35) is:

$$T_t = F_t r = 5.0875 \times 0.48 = 2.445\,(\text{kN.m})$$

Each motor is connected to two tires. Transmission efficiency, $\eta = \eta_{motor}\eta_{transmission}$, is 88 percent. Total torque referred to the motor shaft from equation (2-36) is:

$$T_m = \frac{2\ T_t}{\eta\ GR} = 695\,(\text{N.m})$$

Total torque on the tires side from equation (2-23) is:

$$T_{TR} = F_{TR} r = 244.5 \times 0.48 = 117.2\,(\text{KN.m})$$

Total torque referred to the motor side from equation (2-24) is:

$$T_{TM} = \frac{T_{TR}}{\eta\ GR} = 16.65\,(\text{KN.m})$$

Energy output at driving axle to accelerate the vehicle from equation (2-27) is:

$$E_{acc} = F_a D_1$$

D_1 is the distance travelled during acceleration.

$$D_1 = 0.5at_{acc}^{\ 2} = 0.5 \times 0.48 \times 40^2 = 384\,(\mathrm{m})$$

Therefore, the acceleration energy is 18 kWh.

Some energy is consumed to overcome the aerodynamic drag, rolling resistance, and grade forces. From equation (2-28), equation (2-29), and equation (2-30):

$$E_g = F_{gxT} D_1 = 3.6\,(\mathrm{kWh})$$
$$E_{Roll} + E_{AD} = (F_{Roll} + F_{AD}) D_1 = 4.83\,(\mathrm{kWh})$$

Total energy output required at the axle from equation (2-31) is:

$$E_T = E_{acc} + E_g + E_{Roll} + E_{AD} = 26.43\,(\mathrm{kWh})$$

The averaged tractive power from equation (2-32) is:

$$\mathrm{P}_{\mathrm{TR,average}} = \frac{\Delta E}{\Delta t} = 2.378\,(\mathrm{MW})$$

Required power from the motors is:

$$\mathrm{P}_{\mathrm{TM,average}} = \frac{\mathrm{P}_{\mathrm{TR,average}}}{\eta} = 2.7\,(\mathrm{MW})$$

There are 24 motors in the 'MRMMRMMRM' configuration. Dividing the mean tractive power on 24 gives 111.25 kW. The rated power of the motor is 125 kW. Therefore, the calculation results matches with the metro ratings.

- **Constant Speed Mode (40-103 sec)**

At constant speed linear acceleration, a, and rotational acceleration, $\propto$, are equal to zero. There the total tractive force from equation (2-1) will become:

$$F_{TR} = F_{AD} + F_{Roll} + F_{gxT}$$

The distance travelled during constant speed mode is calculated below from the Table 2-10 data.

$$D_2 = 19.44 \times 63 = 1222 \text{ (m)}$$

The results of the calculations for this mode are shown in Table 2-9. The same procedure is followed as the acceleration mode calculations.

- **Regenerative Braking Mode (103-143 sec)**

During deceleration the motors work as generators which are being fed by the metro braking power. A portion of the kinetic energy from the metro is needed to overcome of rolling resistance, aerodynamic drag, and gravitational force. It means that the recoverable energy is lower than the kinetic energy of the train-set.

In regeneration mode, to calculate the motor torque, the train tires torque is multiplied to the transmission and generator efficiency.

$$T_{TG} = \frac{T_{TR}\eta}{GR}$$

$$\eta = \eta_{generator}\eta_{trnasmisson} = 0.69$$

The calculation results are presented in Table 2-11.

Appendix 3: Detailed System Schematic

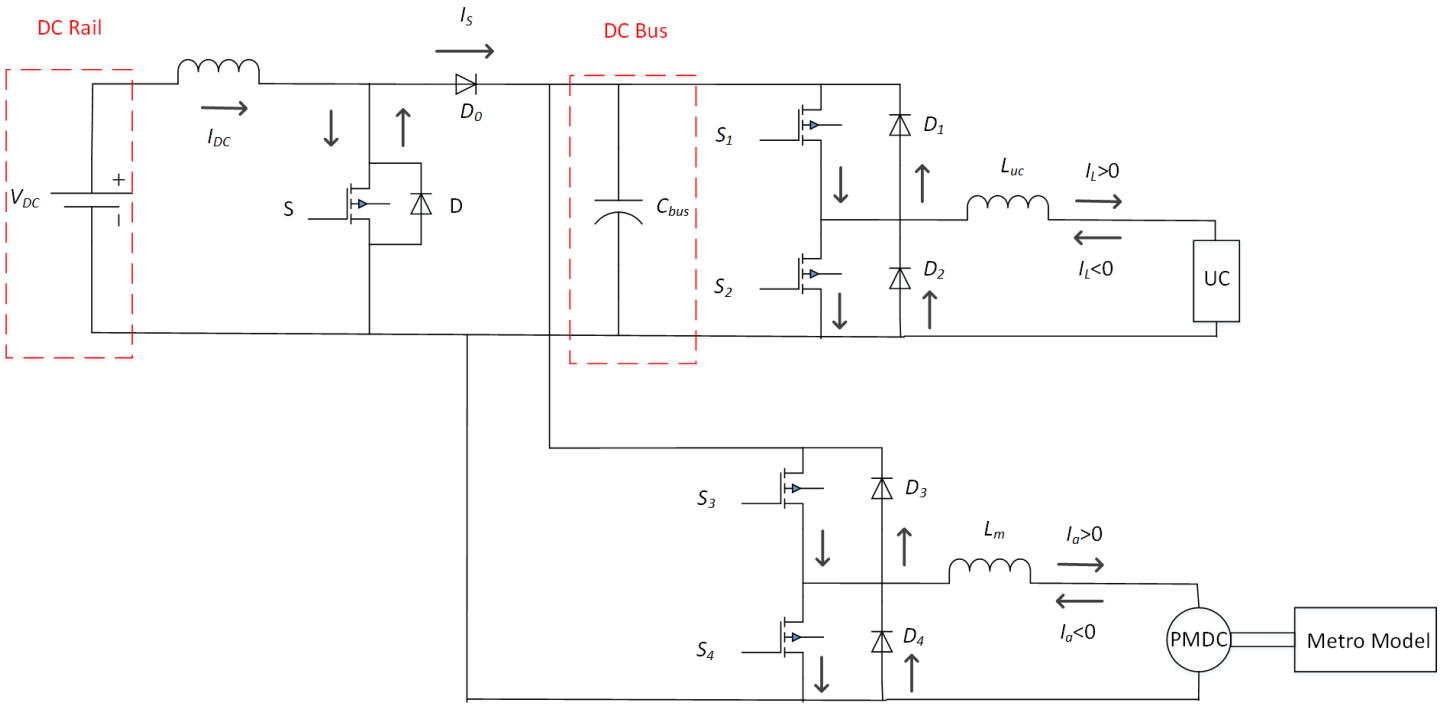
DC Rail
DC Bus
I_S
I_{DC}
D_0
V_{DC}
+
-
S
D
C_{bus}
S_1
D_1
L_{uc}
I_L>0
I_L<0
S_2
D_2
UC
S_3
D_3
L_m
I_a>0
I_a<0
S_4
D_4
PMDC
Metro Model